TECHNISCHE UNIVERSITÄT WIEN

DISSERTATION

Periodic quantum chemical methods for molecule–surface interactions

zur Erlangung des akademischen Grades

Doktor der technischen Wissenschaften

eingereicht von

Theodoros Tsatsoulis

Matrikelnummer 11729280

ausgeführt am Institut für Theoretische Physik
der Fakultät für Physik der Technischen Universität Wien

Betreuer: Univ.-Prof. Dr. Andreas Grüneis

Wien, 18.06.2020

(Unterschrift Verfasser/in) (Unterschrift Betreuer/in)

Declaration of Authorship

Hiermit erkläre ich, dass ich diese Arbeit selbständig verfasst habe, dass ich die verwendeten Quellen und Hilfsmittel vollständig angegeben habe und dass ich die Stellen der Arbeit - einschließlich Tabellen, Karten und Abbildungen -, die anderen Werken oder dem Internet im Wortlaut oder dem Sinn nach entnommen sind, auf jeden Fall unter Angabe der Quelle als Entlehnung kenntlich gemacht habe.

Unterschrift: _____

Datum: _____

Abstract

Interactions of gas-phase molecules with surfaces are at the heart of many fascinating phenomena and commercial applications. First-principles computational models are crucial since they provide an insight into the physical and chemical mechanisms involved. The most popular computational method for such problems is density functional theory due to its good trade-off between accuracy and computational cost. However, fundamental limitations exist in the most widely-used approximate exchange-correlation functionals. Quantum chemical methods constitute a hierarchy that allows for a systematically improvable treatment of quantum many-body effects. However, the steep polynomial scaling of such methods with system size often prohibits their application to molecule–surface systems.

In this work, a periodic quantum chemical framework is presented, applicable to molecule–surface systems, using a canonical periodic coupled-cluster theory implementation and a plane-wave basis set. A compact representation of the two-electron integrals within the projector augmented wave method is summarized. A separable tensor factorization of the integrals is introduced, reducing the computational cost of periodic coupled-cluster calculations. A procedure to use atom-centered Gaussian basis functions in a plane-wave representation is outlined. These functions are employed as virtual orbitals for correlated calculations. A key advantage is the need of much fewer orbitals than when using the full plane-wave basis to approach the complete basis set limit. The slow convergence of wave-function correlated methods with respect to the system size for periodic surfaces is addressed via an interpolation technique of the structure factor resulting in thermodynamic limit results with an exceptional efficiency.

Periodic coupled-cluster theory is applied to a number of prototypical molecule–surface systems. Water adsorption on lithium hydride is investigated with periodic quantum chemistry and results are compared to different electronic-structure methods, such as density functional theory and quantum Monte Carlo techniques, yielding an excellent agreement between higher levels of theory. Physisorption of water on two-dimensional materials, such as graphene and h-BN, is studied with coupled-cluster theory, addressing long-range dispersion interactions. The results of different wavefunction-based methods agree very well, making it possible to benchmark different electronic-structure methods. Finally, dissociative adsorption of molecular hydrogen on silicon surface is considered in two different reaction paths. Using the aforementioned methods it is found that the

adsorption barrier for the two reaction paths are very similar, in excellent agreement with experimental estimates and in contrast to previous density-functional and correlated calculations.

Zusammenfassung

Die Wechselwirkung zwischen Gasphasenmolekülen und Oberflächen spielt eine wichtige Rolle in vielen physikalischen Prozessen und kommerziellen Anwendungen. Ab-initio-Berechnungen sind von entscheidender Bedeutung, da sie einen Einblick in die beteiligten physikalischen und chemischen Mechanismen ermöglichen. Das am häufigsten verwendete Näherungsverfahren zur Lösung der Schrödinger-Gleichung für Mehr-Elektronensysteme basiert auf der Dichtefunktionaltheorie (DFT) und zeichnet sich durch einen guten Kompromiss zwischen Genauigkeit und Rechenaufwand aus. Grundlegende Einschränkungen ergeben sich jedoch durch die verwendeten Näherungen im Austauschkorrelationsfunktional. Im Gegensatz dazu bilden quantenchemische Methoden eine Hierarchie, welche eine systematische Beschreibung der Quanten-Vielteilchen-Effekte ermöglicht. Der vergleichsweise hohe Rechenaufwand dieser Methoden skaliert polynomiell mit der Systemgröße und erschwert ihre Anwendung auf Molekül-Oberflächensysteme.

Diese Dissertation befasst sich mit der Implementierung und Anwendung von quantenchemischen Vielteilchen-Methoden mit periodischen Randbedingungen und einer Ebenen-Wellen-Basis. Die kanonische Coupled-Cluster-Methode wird zur Berechnung von Molekülоberflächensystemen verwendet. Die Berechnung der Zwei-Elektronen-Integrale im Rahmen der Projektor-Augmented-Wave-Methode wird zusammengefasst. Zur Reduktion des Rechenaufwands wird eine Tensorfaktorisierung der Integrale vorgestellt. Ein Verfahren zur Projektion von atomzentrierten Gaußschen Basisfunktionen in eine Ebene-Wellen-Basis wird ebenfalls beschrieben. Es wird gezeigt, dass sich mit diesen Ein-Teilchen-Wellenfunktionen Reaktions- und Adsorptionsenergien besonders effizient berechnen lassen. Die langsame Konvergenz von Grundzustandsenergien in Bezug auf die Systemgröße für periodische Oberflächen wird mittels einer Interpolation des Strukturfaktors signifikant beschleunigt.

Im Rahmen dieser Dissertation werden Adsorptionsenergien von prototypischen Molekül-Oberflächensystemen mit Hilfe der Coupled-Cluster-Methode berechnet. Die Wasseradsorption an Lithiumhydrid wird untersucht und die Ergebnisse werden mit verschiedenen Näherungsverfahren verglichen. Die Übereinstimmung zwischen den hochgenauen wellenfunktionsbasierten Methoden ist ausgezeichnet. Die Physisorption von Wasser an

zweidimensionalen Materialien wie Graphen und h-BN wird ebenfalls mit der Coupled-Cluster-Methode untersucht, wobei langreichweitige Dispersionswechselwirkungen eingehend behandelt werden. Die berechneten Adsorptionsenergien unterschiedlicher wellenfunktionsbasierter Methoden stimmen sehr gut überein, wodurch sich ein zuverlässiger Benchmarkwert ergibt. Schließlich wird die dissoziative Adsorption von molekularem Wasserstoff an der Siliziumoberfläche auf zwei verschiedenen Reaktionswegen betrachtet. Unter Verwendung der oben genannten Verfahren wurde festgestellt, dass die Adsorptionsbarriere für die beiden Reaktionswege sehr ähnlich ist, was ausgezeichnet mit experimentellen Schätzungen übereinstimmt und früheren DFT Ergebnissen widerspricht.

Acknowledgements

Throughout the writing of this dissertation I have received a great deal of support and assistance. I would first like to thank my supervisor, Dr. A. Grüneis, whose expertise was invaluable in the formulating of the research topic and methodology in particular.

Next, I would like to thank all my research associates over the course of my PhD. My colleagues in Vienna: Felix for his irreplaceable help and advice, Alejandro for his vitally important help on computer code, Andreas for his careful evaluation of the dissertation, as well as the whole Grüneis group and the Institute for Theoretical Physics. Next, I would like to express my gratitude to the Max Planck Institute for solid State Research in Stuttgart for giving me the opportunity to work in an unparalleled scientific environment for the first half of my PhD and all my colleagues there.

In addition, I would like to thank my parents and my brother for their wise counsel and sympathetic ear. You are always there for me. Finally, there are my friends, who were of great support in deliberating over our problems and findings, as well as providing happy distraction to rest my mind outside of my research.

Contents

List of Figures

List of Tables

Abbreviations

DFT	**D**ensity **F**unctional **T**heory
XC	e**X**change-**C**orrelation
LDA	**L**ocal **D**ensity **A**pproximation
UEG	**U**niform **E**lectron **G**as
QMC	**Q**uantum **M**onte **C**arlo
GGA	**G**eneralized **G**radient **A**pproximation
RPA	**R**andom **P**hase **A**pproximation
vdW	**v**an **d**er **W**aals
HF	**H**artree **F**ock
RHF	**R**estricted **H**artree **F**ock
FCI	**F**ull **C**onfiguration **I**nteraction
CI	**C**onfiguration **I**nteraction
MP2	second-order **M**øller–**P**lesset perturbation theory
HOMO	**H**ighest **O**ccupied **M**olecular **O**rbital
LUMO	**L**owest **U**noccupied **M**olecular **O**rbital
CC	**C**oupled **C**luster
DIIS	**D**irect **I**nversion in the **I**terative **S**ubspace
BCH	**B**aker–**C**ampbell–**H**ausdorff
PAW	**P**rojector **A**ugmented **W**ave
USPP	**U**ltra**S**oft **P**seudo**P**otential
AE	**A**ll-**E**lectron
GTO	**G**aussian **T**ype **O**rbital
PGTO	**P**seudized **G**aussian **T**ype **O**rbital
SVD	**S**ingular **V**alue **D**ecomposition
OAF	**O**ptimized **A**uxiliary **F**ield

ALS	**A**lternating **L**east **S**quares
RALS	**R**egularized **A**lternating **L**east **S**quares
CPD	**C**anonical **P**olyadic **D**ecomposition
THC	**T**ensor **H**yper**C**ontraction
BSSE	**B**asis **S**et **S**uperposition **E**rror
CP	**C**ounterpoise **C**orrection
DCSD	**D**istinguishable **C**luster **S**ingles **D**oubles
TRD	**T**ensor **R**ank **D**ecomposition
CBS	**C**omplete **B**asis **S**et
NO	**N**atural **O**rbital
PBE	**P**erdew–**B**urke–**E**rnzerhof
SCF	**S**elf-**C**onsistent-**F**ield
MBD	**M**any **B**ody **D**ispersion
DLPNO	**D**omain **L**ocal **P**air **N**atural **O**rbital
NEB	**N**udged **E**lastic **B**and
SCAN	**S**trongly **C**onstrained and **A**ppropriately **N**ormed

Dedicated to my family...

Chapter 1

Introduction

A vast wealth of properties of atoms, molecules, and materials predominantly originate from the interacting electrons, moving in the electric field of the nuclei. This correlated motion of the electrons in molecules and solids leads to a variety of phenomena that are observed in nature and are of great importance in present-day technological advancements. Such phenomena include molecule–surface interactions and crystal phase transitions among others. Modern experimental techniques, such as ultra high-vacuum, diffraction techniques, electron and ion scattering spectroscopy, and scanning tunneling microscopy, allow the study of well-defined solids, surfaces and molecules in a controlled environment, often on an atomic level.

Quantum chemistry and electronic structure theory, on the other hand, has emerged as an indispensable tool for investigating such problems in chemistry and physics. With recent developments in the computational methods and recent advancements in supercomputers quantum chemistry is today routinely applied to compute and predict structures, spectroscopic parameters, as well as reaction barriers for moderate-sized molecular complexes. For extended systems, however, like solids and surfaces approximate methods, such as density functional theory in the framework of approximate functionals, have dominated the field due to a favourable balance of computational cost and accuracy. Although exact in theory, practical density functional theory calculations use approximations that are far away from being error-free. Validation of these approximations against more accurate methods is an ongoing research in the field of quantum chemistry.

In spite of this increasing importance of computational quantum chemistry in the field of chemistry and physics this work is devoted to the implementation of quantum chemical wavefunction-based methods for periodic systems. The aim of this thesis is to present a computationally affordable, yet accurate, framework for quantum chemical calculations in solids and surfaces, thus extending the predictive power of electronic structure theory.

Chapter 2

Interacting electrons in Molecules and Solids

An important goal of modern electronic structure theory is the *ab-initio* description of a molecule or solid and the accurate prediction of its properties. *Ab-initio* quantum chemical methods aim at obtaining accurate solutions of the Schrödinger equation in order to yield useful information such as electron densities, energies and other properties of the system. In this chapter the electronic Hamiltonian within the Born–Oppenheimer approximation will be introduced, whereby the many-electron Schrödinger equation is decoupled from the motion of the nuclei.

2.1 The Hamiltonian

A molecule or a solid is a system of interacting nuclei and electrons and is described by the following Hamiltonian

$$\hat{\mathcal{H}} = \hat{T}_{\text{el}} + \hat{T}_{\text{nuc}} + V_{\text{el–nuc}} + V_{\text{el–el}} + V_{\text{nuc–nuc}} \ , \tag{2.1}$$

where $\hat{T}_{\text{el}}$ and $\hat{T}_{\text{nuc}}$ is the kinetic energy operator of the electrons and the nuclei, respectively. $V_{\text{el–el}}$, $V_{\text{nuc–nuc}}$, and $V_{\text{el–nuc}}$ describes the electrostatic interaction potential of the electrons, the nuclei, and between them, respectively. In principle the only remaining task is to solve the corresponding time-independent Schrödinger equation

$$\hat{\mathcal{H}}\Psi_n(\mathbf{r}, \mathbf{R}) = \mathcal{E}_n\Psi_n(\mathbf{r}, \mathbf{R}) \ , \tag{2.2}$$

with the appropriate symmetry for the wavefunction.

2.1.1 Born–Oppenheimer approximation

The electron–nuclear Schrödinger equation for a molecule or solid is highly dimensional and thus practically impossible to be solved analytically. Thus, approximations that significantly simplify the theory have to be employed, without seriously affecting the accuracy or the qualitative description of the system. The most fundamental one is the Born–Oppenheimer approximation [1], which allows the decoupling of the electronic and nuclear motion. Because the mass of the nuclei is $10^4 - 10^5$ times larger than the mass of an electron one may assume that electrons adapt to the motion of the nuclei instantaneously. It is therefore convenient to recast the Hamiltonian into the form

$$\hat{\mathcal{H}} = \hat{\mathcal{H}}^{(\mathrm{el})} + \hat{T}_{\mathrm{nuc}} \ , \tag{2.3}$$

where $\hat{T}_{\mathrm{nuc}}$ is the nuclear kinetic energy and the electronic part is defined as

$$\hat{\mathcal{H}}^{(\mathrm{el})} = \hat{T}_{\mathrm{el}} + V_{\mathrm{el\text{–}nuc}} + V_{\mathrm{el\text{–}el}} + E_{\mathrm{nuc\text{–}nuc}} \ , \tag{2.4}$$

where the nuclear–nuclear repulsion energy $E_{\mathrm{nuc\text{–}nuc}}$ is included into the electronic Hamiltonian. Consequently the total wavefunction may be decomposed into its electronic and nuclear components

$$\Psi_n(\mathbf{r}, \mathbf{R}) = \Psi_n^{(\mathrm{el})}(\mathbf{r}|\mathbf{R})\Phi_n(\mathbf{R}) \ . \tag{2.5}$$

For a set of fixed nuclear coordinates $\{\mathbf{R}\}$ we are therefore interested into solving the electronic Schrödinger equation

$$\hat{\mathcal{H}}^{(\mathrm{el})}\Psi_n^{(\mathrm{el})}(\mathbf{r}|\mathbf{R}) = \mathcal{E}_n^{(\mathrm{el})}\Psi_n^{(\mathrm{el})}(\mathbf{r}|\mathbf{R}) \ . \tag{2.6}$$

2.2 The many-electron Schrödinger equation

Although the Born–Oppenheimer approximation simplifies the problem, obtaining approximate, yet accurate, solutions for the many electron Schrödinger equation is still a formidable task. In what follows the electronic Hamiltonian will be denoted by $\hat{\mathcal{H}}$, and $\Psi(\mathbf{r})$ refers to the many-electron wavefunction. The non-relativistic electronic Hamiltonian, within the Born–Oppenheimer approximation and using Hartree atomic units (*a.u.*) has the form

$$\hat{\mathcal{H}} = -\frac{1}{2}\sum_i \nabla_i^2 - \sum_i V_{\mathrm{N}}(\mathbf{r}_i) + \frac{1}{2}\sum_{i \neq j} \frac{1}{r_{ij}} \ , \tag{2.7}$$

where i and j are indices that run over all N electrons. The corresponding time-independent Schrödinger equation reads

$$\hat{\mathcal{H}}\Psi_n(\mathbf{r}) = \mathcal{E}_n\Psi_n(\mathbf{r}) \ , \tag{2.8}$$

where the index n refers to the n-th solution with $\Psi_n(\mathbf{r})$ and $\mathcal{E}_n$ being the many-electron eigenstates and eigenenergies respectively. The first term of the electronic Hamiltonian $\hat{\mathcal{H}}$ is the kinetic energy of the electrons, the second is the electron–nuclear electrostatic attraction via the Coulomb potential, and the last term represents the electron–electron Coulombic repulsion. The electron–nuclear attraction has the form

$$V_{\mathrm{N}}(\mathbf{r}) = \sum_{\alpha} \frac{Z_\alpha}{|\mathbf{R}_\alpha - \mathbf{r}|} \ , \tag{2.9}$$

where $\mathbf{R}_\alpha$ are the nuclear positions and Z_α the nuclear charge of the α-th nuclei. The last term in Eq. (2.7) is a two-electron operator that prohibits the reduction of the many-electron problem to a set of independent particle problems.

Chapter 3

Electronic structure theory of many-body systems

Since the solution of the many electron Schrödinger equation is a formidable task for any but the systems with very few electrons, approximate methods are needed. In this Chapter important approximate methods to deal with an *ab-initio* molecular or solid electronic Hamiltonian are discussed.

3.1 Density Functional Theory

Among the many methods to solve the many-electron Schrödinger equation, density functional theory (DFT) [2] is nowadays the most popular approach for electronic structure calculations of solids and large molecular complexes due to its good trade off between accuracy and computational cost. The basic variable in DFT is the electronic density rather than the many-electron wavefunction. DFT is based on two theorems by Hohenberg and Kohn [3]. The first states that the electronic ground state density $n(\mathbf{r})$ of a many-electron system in an external potential $V_{\mathrm{N}}(\mathbf{r})$ determines this potential uniquely. The second theorem of Hohenberg and Kohn [3] states that the ground-state energy can be obtained by the minimization of a functional $E[n(\mathbf{r})]$ with respect to the electron density $n(\mathbf{r})$.

$$E[n(\mathbf{r})] = \int V_{\mathrm{N}}(\mathbf{r}) n(\mathbf{r}) \mathrm{d}\mathbf{r} + F[n(\mathbf{r})] \ , \tag{3.1}$$

where $V_{\mathrm{N}}(\mathbf{r})$ is the external potential of the nuclei and $F[n(\mathbf{r})]$ a universal functional, in the sense that is system independent, that includes the kinetic energy of the electrons as well as their Coulombic repulsion. Kohn and Sham [4] proposed the idea of replacing

the interacting electronic system with a non-interacting one with the same electronic density $n(\mathbf{r})$. The electron density can then be written in terms of one-electron orbitals of the fictitious non-interacting system

$$n(\mathbf{r}) = \sum_i \psi_i^*(\mathbf{r})\psi_i(\mathbf{r}) \ , \tag{3.2}$$

where i runs over all occupied one-electron orbitals $\psi_i(\mathbf{r})$. This enabled them to write the Hohenberg–Kohn energy functional in the following form [4]

$$E[n(\mathbf{r})] = -\frac{1}{2}\sum_i \int \psi_i^*(\mathbf{r})\nabla^2\psi_i(\mathbf{r})\mathrm{d}\mathbf{r} + \int V_\mathrm{N}(\mathbf{r})n(\mathbf{r})\mathrm{d}\mathbf{r} + \frac{1}{2}\int\int \frac{n(\mathbf{r})n(\mathbf{r}')}{|\mathbf{r}-\mathbf{r}'|}\mathrm{d}\mathbf{r}\mathrm{d}\mathbf{r}' + E_\mathrm{xc}[n(\mathbf{r})] \ , \tag{3.3}$$

where the first term represents the kinetic energy $T\big[\{\psi_i|n(\mathbf{r})\}\big]$ of the non-interacting system with electron density $n(\mathbf{r})$, the second term the interaction with the electrostatic potential of the nuclei, the third term the Hartree energy $E_\mathrm{H}[n(\mathbf{r})]$, representing the classical electrostatic repulsion of two charge densities, and the last term is the so-called exchange and correlation (XC) energy, which represents the remaining error to the energy functional and is defined as

$$E_\mathrm{xc}[n(\mathbf{r})] = F[n(\mathbf{r})] - T\big[\{\psi_i|n(\mathbf{r})\}\big] - E_\mathrm{H}[n(\mathbf{r})] \ . \tag{3.4}$$

Kohn and Sham showed that the minimization of the energy functional of Eq. (3.3) leads to a set of self-consistent equations [4] that lead to the ground state density and energy

$$\left(-\frac{1}{2}\nabla_i^2 + V_\mathrm{N}(\mathbf{r}) + V_\mathrm{H}(\mathbf{r}) + V_\mathrm{xc}(\mathbf{r})\right)\psi_i(\mathbf{r}) = \varepsilon_i\psi_i(\mathbf{r}) \ , \tag{3.5}$$

where V_N is the nuclear electrostatic potential

$$V_\mathrm{N}(\mathbf{r}) = \sum_\alpha \frac{Z_\alpha}{|\mathbf{R}_\alpha - \mathbf{r}|} \ , \tag{3.6}$$

V_H is the Hartree potential

$$V_\mathrm{H}(\mathbf{r}) = \int \frac{n(\mathbf{r}')}{|\mathbf{r}-\mathbf{r}'|}\mathrm{d}\mathbf{r}' \ , \tag{3.7}$$

and $V_\mathrm{xc}(\mathbf{r})$ the so-called XC potential

$$V_\mathrm{xc}(\mathbf{r}) = \frac{\delta E_\mathrm{xc}[n(\mathbf{r})]}{\delta n(\mathbf{r})} \ . \tag{3.8}$$

Thus far Kohn–Sham DFT represents an exact mathematical framework for solving the many-electron Schrödinger equation from an electronic density viewpoint. Although

formally exact, the XC energy functional is an unknown quantity that has to be approximated. The simplest approximation is to assume a local form for the XC functional

$$E_{\mathrm{xc}}[n(\mathbf{r})] = \int \varepsilon_{\mathrm{xc}}(\mathbf{r}, [n(\mathbf{r})]) n(\mathbf{r}) \mathrm{d}\mathbf{r} \ , \tag{3.9}$$

i.e., the functional depends locally on the density $n(\mathbf{r})$. One of the first and best-known approximations is the local density approximation (LDA). $\varepsilon_{\mathrm{xc}}(\mathbf{r}, [n(\mathbf{r})])$ is the XC energy per particle of the uniform electron gas (UEG) with density n. The exchange part is well known, whereas the first accurate approximation for the correlation part of the functional was given by Ceperley and Alder [5, 6], obtained by accurate quantum Monte Carlo (QMC) techniques. It is apparent that the LDA is reasonably accurate when the electronic density is close to a uniform one. Nevertheless it produces surprisingly adequate results for inhomogeneous densities as well. LDA predicts geometries of molecules and solids, as well as bond lengths with an impressive accuracy. Binding and dissociation energies, on the other hand are often less satisfactory. A better approximation to the XC functional is obtained when the gradient of the density is included. The XC energy has then the form

$$E_{\mathrm{xc}}[n(\mathbf{r})] = \int \varepsilon_{\mathrm{xc}}(\mathbf{r}, [n(\mathbf{r})], [\nabla n(\mathbf{r})]) n(\mathbf{r}) \mathrm{d}\mathbf{r} \ , \tag{3.10}$$

where $\varepsilon_{\mathrm{xc}}(\mathbf{r}, [n(\mathbf{r})], [\nabla n(\mathbf{r})])$ is expanded in a set of parameterized non-linear functions. Such an approximation is termed generalized gradient approximation (GGA) since it includes the gradient as well as the local density. One of the most widely-used GGA functionals in solid state calculations is PBE [7].

A hierarchy of XC functional approximations was introduced by Perdew [8], termed the Jacob's ladder of DFT, where each rung includes additional ingredients to the approximation of the XC functional. This is schematically depicted in Fig. 3.1. In the lowest rung lies the LDA that depends locally on the electron density $n(\mathbf{r})$. In the second rung we find GGA where additionally the gradient of the density $\nabla n(\mathbf{r})$ is used. In the third rung meta-GGA utilizes the kinetic energy density $\tau(\mathbf{r})$ in the XC functional [9]. The meta-GGA rung is the highest rung in the Jacob's ladder of DFT that is not fully non-local. The exact exchange energy, as we will see later, is a fully non-local functional of the one-electron orbitals. Becke observed the importance of exact-exchange information to local or semi-local density-functional approximations. This has led to the so-called hybrid functionals, that lie on the fourth rung of the ladder, of the form [10]

$$E_{\mathrm{XC}}^{\mathrm{Hybrid}} = E_{\mathrm{XC}}^{\mathrm{GGA}} + \alpha (E_{\mathrm{X}}^{\mathrm{exact}} - E_{\mathrm{X}}^{\mathrm{GGA}}) \ , \tag{3.11}$$

where E_{XC} and E_{X} denote the XC and exchange energy respectively, thus mixing exact

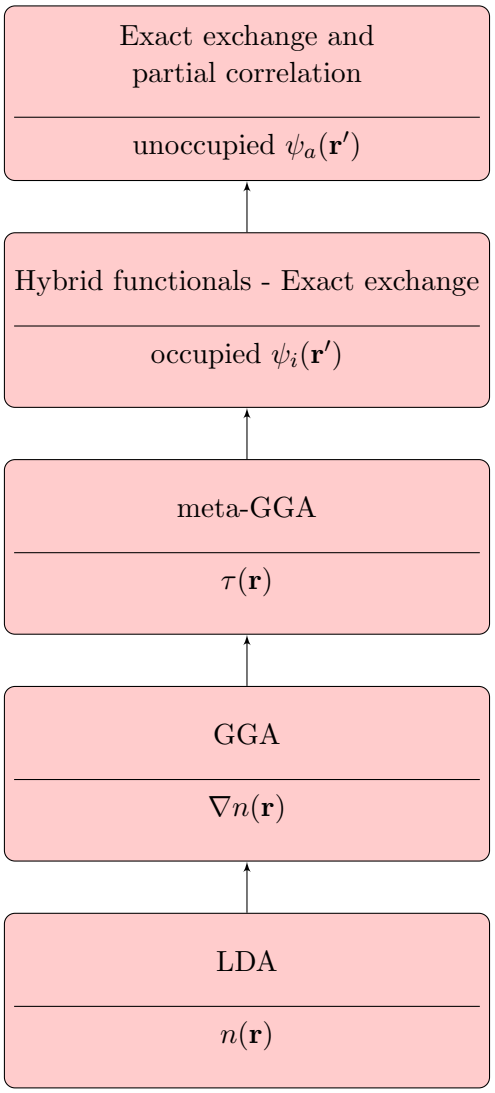

FIGURE 3.1: Schematic illustration of Jacob's ladder of approximations to the XC functional [8].

with local exchange energy, with a scaling factor α. On the fifth rung lie methods that include exact exchange and exact correlation to a certain order, like the Random Phase Approximation (RPA) [11, 12]. We shall mention that RPA is the only method of the DFT rungs that seamlessly includes long-range non-local van der Waals (vdW) interactions [13].

3.2 Hartree–Fock Theory

The Hartree–Fock (HF) approximation [14–16] is based on the assumption that the motion of every electron can be expressed by a single-particle orbital that does not depend explicitly on the coordinates of the other electrons. Due to the fermionic nature

of the electrons the many-particle wavefunction must be antisymmetric with respect to the exchange of two particles, i.e.,

$$\Psi(\dots,\mathbf{x}_i,\dots,\mathbf{x}_j,\dots) = -\Psi(\dots,\mathbf{x}_j,\dots,\mathbf{x}_i,\dots) \;, \tag{3.12}$$

where $\mathbf{x}$ is a shorthand notation for the spatial ($\mathbf{r}$) and spin (σ) coordinate of an electron. In HF theory the one-particle states are orbitals that can be expanded in any basis. For the sake of simplicity we will assume that the one electron orbitals are real.

The HF wavefunction can be expressed as an antisymmetrized product of one-particle states, via a Slater determinant

$$\Psi(\mathbf{x}_1,\mathbf{x}_2,\dots,\mathbf{x}_N) = \frac{1}{\sqrt{N!}} \begin{vmatrix} \psi_1(\mathbf{x}_1) & \psi_1(\mathbf{x}_2) & \dots & \psi_1(\mathbf{x}_N) \\ \psi_2(\mathbf{x}_1) & \psi_2(\mathbf{x}_2) & \dots & \psi_2(\mathbf{x}_N) \\ \vdots & \vdots & \vdots & \vdots \\ \psi_N(\mathbf{x}_1) & \psi_N(\mathbf{x}_2) & \dots & \psi_N(\mathbf{x}_N) \end{vmatrix} \;. \tag{3.13}$$

The orbitals in the HF determinant are optimized by minimizing the expectation value of the Hamiltonian $\hat{\mathcal{H}}_{\text{el}}$ with the constraint that the one-particle orbitals $\psi_i(\mathbf{x})$ are orthonormal. Using the Slater–Condon rules (see Appendix A), the variational energy expression of the electronic Hamiltonian using the HF wavefunction ansatz (3.13) takes the form

$$E_{\text{HF}} = \langle\Psi|\hat{\mathcal{H}}|\Psi\rangle = \sum_i^{\text{occ.}} \langle\psi_i|\hat{h}|\psi_i\rangle + \frac{1}{2}\sum_{i,j}^{\text{occ.}} \left(\langle\psi_i\psi_j|\frac{1}{r_{12}}|\psi_i\psi_j\rangle - \langle\psi_i\psi_j|\frac{1}{r_{12}}|\psi_j\psi_i\rangle \right) \;, \tag{3.14}$$

where the one-electron integral $\langle\psi_i|\hat{h}|\psi_i\rangle$ is defined as

$$\langle\psi_i|\hat{h}|\psi_i\rangle = -\frac{1}{2}\langle\psi_i|\nabla^2|\psi_i\rangle + \langle\psi_i|V_{\text{N}}(\mathbf{r})|\psi_i\rangle \;, \tag{3.15}$$

with the nuclear potential $V_{\text{N}}(\mathbf{r})$ defined in Eq. (2.9). The two-electron integrals are defined as

$$\langle\psi_i\psi_j|\frac{1}{r_{12}}|\psi_i\psi_j\rangle = \int\int \psi_i(\mathbf{x})\psi_j(\mathbf{x}')\frac{1}{|\mathbf{r}-\mathbf{r}'|}\psi_i(\mathbf{x})\psi_j(\mathbf{x}')\mathrm{d}\mathbf{x}\mathrm{d}\mathbf{x}' \;, \tag{3.16}$$

$$\langle\psi_i\psi_j|\frac{1}{r_{12}}|\psi_j\psi_i\rangle = \int\int \psi_i(\mathbf{x})\psi_j(\mathbf{x}')\frac{1}{|\mathbf{r}-\mathbf{r}'|}\psi_i(\mathbf{x}')\psi_j(\mathbf{x})\mathrm{d}\mathbf{x}\mathrm{d}\mathbf{x}' \;. \tag{3.17}$$

The first two-electron integral describes the classical electrostatic Coulomb interaction between two charge densities $\rho_i(\mathbf{x}) = |\psi_i(\mathbf{x})|^2$ and $\rho_j(\mathbf{x}') = |\psi_i(\mathbf{x}')|^2$, i.e.,

$$\langle\psi_i\psi_j|\frac{1}{r_{12}}|\psi_i\psi_j\rangle = \int\int \rho_i(\mathbf{x})\frac{1}{|\mathbf{r}-\mathbf{r}'|}\rho_j(\mathbf{x}')\mathrm{d}\mathbf{x}\mathrm{d}\mathbf{x}' \;. \tag{3.18}$$

The second two-electron integral has no classical counterpart. It stems solely from the antisymmetry of the many-electron wavefunction and is denoted as the exchange integral. The Hartree–Fock energy expression E_{HF}, defined in Eq.(3.14), needs to be minimized with respect to the one-particle orbitals subjected to the orthonormality constraint $\langle\psi_i|\psi_j\rangle = \delta_{ij}$. Using the method of Lagrange multipliers, we arrive at the self-consistent HF equations for the one-particle orbitals ψ_i [17, 18]

$$\begin{aligned}\hat{h}(\mathbf{r})\psi_i(\mathbf{x}) + \sum_j \left(\int \psi_j(\mathbf{x}') \frac{1}{|\mathbf{r}-\mathbf{r}'|} \psi_j(\mathbf{x}') \mathrm{d}\mathbf{x}' \right) \psi_i(\mathbf{x}) \\ - \sum_j \left(\int \psi_j(\mathbf{x}') \frac{1}{|\mathbf{r}-\mathbf{r}'|} \psi_i(\mathbf{x}') \mathrm{d}\mathbf{x}' \right) \psi_j(\mathbf{x}) = \varepsilon_i \psi_i(\mathbf{x}) \ , \end{aligned} \tag{3.19}$$

where ε_i are eigenenergies corresponding to the orbitals ψ_i. Eq. (3.19) can be rewritten as

$$\left(\hat{h}(\mathbf{r}) + \sum_j \left[\hat{J}_j - \hat{K}_j \right] \right) \psi_i(\mathbf{x}) = \varepsilon_i \psi_i(\mathbf{x}) \ , \tag{3.20}$$

where $\hat{J}_j$ is the Coulomb operator and $\hat{K}_j$ the exchange operator. The latter one represents a non-local potential that is a consequence of the antisymmetry of the wavefunction and cures the self-interaction of an electron, i.e. the fact that an electron interacts with itself via the Coulomb potential. We can define the Fock operator as

$$\hat{f} = \hat{h}(\mathbf{r}) + \sum_j \left[\hat{J}_j - \hat{K}_j \right] \ , \tag{3.21}$$

and using this definition the HF equations have the following form

$$\hat{f}\psi_i = \varepsilon_i \psi_i \ . \tag{3.22}$$

Thus far spin-orbitals have been assumed without imposing any restriction on the spin and spatial part of the one-particle states. When each spatial orbital ϕ_i is occupied by one spin-up and one spin-down electron this constitutes the closed-shell or restricted HF (RHF) approximation. Carrying out the spin integration the expression for the HF energy takes the following form,

$$E_{\mathrm{HF}} = \sum_i^{\mathrm{occ.}} 2\langle\phi_i|\hat{h}|\phi_i\rangle + \sum_{i,j}^{\mathrm{occ.}} \left(2\langle\phi_i\phi_j|\frac{1}{r_{12}}|\phi_i\phi_j\rangle - \langle\phi_i\phi_j|\frac{1}{r_{12}}|\phi_j\phi_i\rangle \right) \ . \tag{3.23}$$

Introducing the "Muliken" or "chemical" notation for the two electron integrals

$$(\phi_i\phi_k|\phi_j\phi_l) = \langle\phi_i\phi_j|\phi_k\phi_l\rangle = \int\int \phi_i(\mathbf{r}_1)\phi_j(\mathbf{r}_2)\frac{1}{r_{12}}\phi_k(\mathbf{r}_1)\phi_l(\mathbf{r}_2)\mathrm{d}\mathbf{r}_1\mathrm{d}\mathbf{r}_2 \ , \tag{3.24}$$

the RHF energy can be rewritten as

$$E_{\mathrm{HF}} = \sum_{i}^{\mathrm{occ.}} 2\langle\phi_i|\hat{h}|\phi_i\rangle + \sum_{i,j}^{\mathrm{occ.}} \Big[2\left(\phi_i\phi_i|\phi_j\phi_j\right) - \left(\phi_i\phi_j|\phi_j\phi_i\right)\Big] \ . \tag{3.25}$$

In any computer implementation the one-electron orbitals ϕ_i are expanded in a linear combination of basis functions χ_μ

$$\phi_i(\mathbf{r}) = \sum_{\mu=1}^{N_\mathrm{b}} \chi_\mu(\mathbf{r}) C_{\mu i} \ , \tag{3.26}$$

where the sum runs over all N_b basis functions. In molecular quantum chemistry the most widely-used basis set is an atomic orbital basis. Later we will see that for periodic systems plane-waves represent a very convenient basis set and we will discuss the implementation of HF equations within this basis. Using a complete orthonormal basis the orbitals can be represented exactly, however, one needs an infinite amount of functions to do that. Thus, a truncated basis set is used in practice. Inserting Eq. (3.29) into the HF Eq. (3.22) leads to the Roothaan equations

$$\hat{f}\sum_{\mu=1}^{N_\mathrm{b}} \chi_\mu(\mathbf{r}) C_{\mu i} = \varepsilon_i \sum_{\mu=1}^{N_\mathrm{b}} \chi_\mu(\mathbf{r}) C_{\mu i} \ . \tag{3.27}$$

Left multiplying and integrating with $\chi^*_\nu(\mathbf{r})$, and assuming orhtonormality of the basis (which is true in the case of plane-waves) the Roothaan equations can be written in the following compact form

$$\sum_{\nu} F_{\mu\nu} C_{\nu i} = \varepsilon_i C_{\mu i} \ , \tag{3.28}$$

where $F_{\mu\nu}$ is the Fock matrix in an orthonormal basis set

$$F_{\mu\nu} = \left\langle \chi_\mu(\mathbf{r}) \middle| \hat{f} \middle| \chi_\nu(\mathbf{r}) \right\rangle \ . \tag{3.29}$$

The RHF method approximates the many-electron wavefunction by a single Slater determinant and according to the variational principle the HF energy constitutes an upper bound for the exact energy. The correlation energy is the energy missing from the RHF approximation to reach the exact value and is defined as

$$E_{\mathrm{corr}} = E_{\mathrm{exact}} - E_{\mathrm{HF}} \ . \tag{3.30}$$

Although the correlation energy is often a small part of the exact energy, it usually contributes significantly to energy differences that determine chemical bonding and interaction energies. Furthermore along a reaction pathway the correlation energy may

vary significantly as a result of the rearranged chemical bonds. Hence more sophisticated methods, such as perturbation theory, are needed to compute the correlation energy in order to estimate a reaction scheme accurately.

3.3 Post Hartree–Fock Methods

The HF method is a mean-field (or independent electron) approximation where each electron moves independently in an average field produced by the other electrons. The HF wavefunction includes exchange effects arising only from the anti symmetry of the many-electron wavefunction. Electronic correlation effects due to the electron–electron Coulomb interaction are not captured by HF.

HF theory approximates the many-electron wavefunction by a single Slater determinant $\Psi(\mathbf{x}_1, \mathbf{x}_2, \ldots, \mathbf{x}_N)$, as shown in Eq. (3.13), where the one-electron orbitals are minimized variationally and are expanded in a truncated basis. A many-electron wavefunction can in turn be expanded as a linear combination of Slater determinants $\Psi_I(\mathbf{x}_1, \mathbf{x}_2, \ldots, \mathbf{x}_N)$ using the HF one-particle orbitals. For a complete one-electron basis, one can approximate the many-electron wavefunction exactly within this basis, however, in practice the many-electron wavefunction can only be approximated using a truncated basis set. The exact form of the wavefunction dictates a slow convergence with respect to the number of basis set functions. The many-electron wavefunction exhibits a characteristic cusp at the coalescence points of two electrons [19–21]. The Coulomb potential $\frac{1}{r_{12}}$ in the electronic Hamiltonian of Eq. (2.7) is singular for zero interelectronic distance ($r_{12} = 0$). In order for the energy to remain finite the singularity must be canceled by an opposite singularity in the kinetic energy which is manifested via a discontinuity in the first derivative of the wavefunction. In the center-of-mass of two electrons with opposite spin, close to zero interelectronic distance, the wavefunction is linear with respect to the interelectronic distance r_{12}

$$\Psi(\mathbf{r}_1, \mathbf{r}_2) \sim \Psi(r_{12} = 0)\left(1 + \frac{1}{2} r_{12} + \ldots\right) . \tag{3.31}$$

This cusp results in a discontinuity in the first derivative of the wavefunction at $r_{12} = 0$

$$\left(\frac{\partial \Psi}{\partial r_{12}}\right)_{r_{12}=0} \sim \frac{1}{2}\Psi(r_{12} = 0) , \tag{3.32}$$

which in turn results in a singularity of the second derivative at $r_{12} = 0$. Such a wavefunction cusp can be approximated using a finite basis set, however, the many-electron wavefunction will never exhibit a discontinuity. This is illustrated in Fig. 3.2 where the singlet two-electron wavefunction for the helium atom is plotted against the

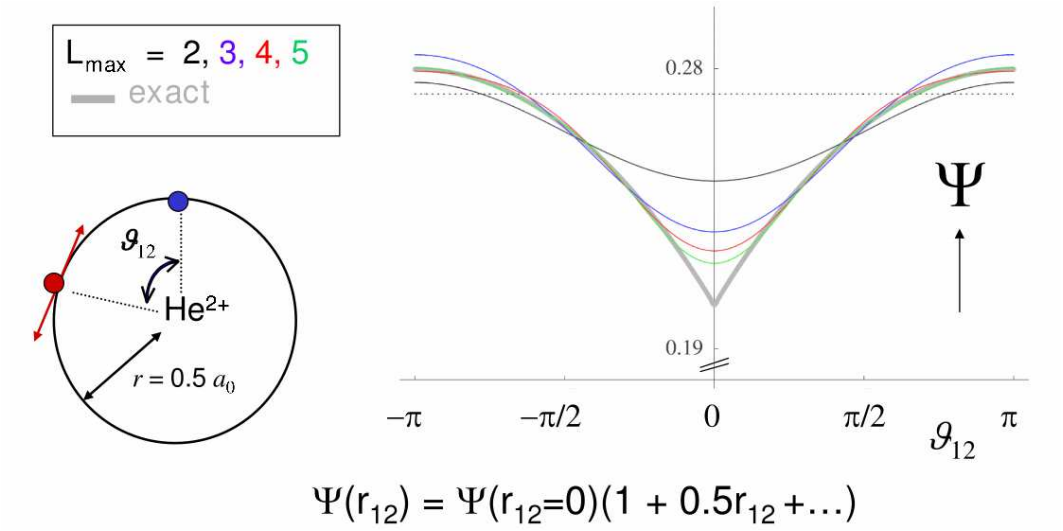

FIGURE 3.2: Two-electron wavefunction of the He atom as a function of the angle θ_{12} for a fixed radial distance. The exact wavefunction exhibits a characteristic cusp at θ_{12}, where the two electrons coalesce. Slater determinant expansions of the many-electron wavefunction do not have a cusp and converge very slowly towards the exact solution. Figure taken from Ref. [20]

angular interelectronic distance for a fixed radial distance. The HF Slater determinant does not depend on the interelectronic distance, whereas, a linear combination of Slater determinants approximates the cusp. It can be clearly seen that a large number of atomic basis functions is needed in order to get an accurate description of the wavefunction cusp. When all possible Slater determinants are used to linearly expand the many-electron wavefunction we have the full configuration interaction (FCI) expansion. However, the number of Slater determinants N_{det} increases dramatically with respect to the total number of spin-up and -down electrons $N = N_\alpha + N_\beta$ and the number of basis set functions N_b

$$N_{\text{det}} = \frac{N_\text{b}!}{N_\alpha!(N_\text{b} - N_\alpha)!} \cdot \frac{N_\text{b}!}{N_\beta!(N_\text{b} - N_\beta)!} \tag{3.33}$$

prohibiting the FCI expansion for anything but the smallest systems.

3.3.1 Configuration Interaction

Like in HF theory, where the expectation value of the Hamiltonian is minimized using a single Slater determinant as the trial wavefunction, in configuration interaction (CI) the expectation value of the Hamiltonian is variationally minimized using an expansion of Slater determinants as a trial wavefunction. The many-electron wavefunction is

expanded in the basis of Slater determinants as

$$\Psi_{\mathrm{CI}} = \sum_I c_I \Phi_I \ . \tag{3.34}$$

Assuming the one-particle orbitals to be orthonormal ($\langle\phi_i|\phi_j\rangle = \delta_{ij}$) all possible Slater determinants are also orthonormal ($\langle\Phi_I|\Phi_J\rangle = \delta_{IJ}$). The expansion coefficients c_I can be obtained by variationally minimizing the energy expectation value

$$E_{\mathrm{CI}} = \frac{\langle\Psi_{\mathrm{CI}}|\hat{\mathcal{H}}|\Psi_{\mathrm{CI}}\rangle}{\langle\Psi_{\mathrm{CI}}|\Psi_{\mathrm{CI}}\rangle} \ . \tag{3.35}$$

which leads to the following eigenvalue equation [18]

$$\langle\Phi_I|\hat{\mathcal{H}} - E_{\mathrm{CI}}|\Psi_{\mathrm{CI}}\rangle = \sum_J \Big[\langle\Phi_I|\hat{\mathcal{H}}|\Phi_J\rangle - \lambda c_J \delta_{IJ}\Big] = 0 \ , \tag{3.36}$$

or in compact matrix form

$$\mathbf{Hc} = \mathbf{Ec}, \tag{3.37}$$

where $\mathbf{H}$ is the Hamiltonian matrix in the Slater determinant basis, $\mathbf{c}$ is the coefficient vector, and $\mathbf{E}$ is a diagonal matrix with the energy expectation value. It is noted that when all possible excitations are included in the CI expansion, we have the full CI (FCI) expansion. The latter is often termed as exact diagonalization, as it represents the exact solution within the employed basis set.

One can define a hierarchy of CI wavefunctions, depending on the excitation levels that are included. This gives rise to CISD, CISDT, and so forth, up to the FCI method. A major drawback of the truncated CI methods, is that they are not size consistent. For a method to be size consistent, the sum of the energies of independently computed fragments should be identical to the energy of the total system, when the two fragments are separated by a large distance. Let us consider for example the CID method. The product wavefunction of the individual fragments contains quadrupole excitations, since each individual fragment is truncated up to double excitations. However, the combined system includes only up to double excitations as a result of the truncation of the CI wavefunction. These missing quadrupole excitations are products of double excitations. Later it will be shown how the exponential ansatz of the coupled cluster method overcomes this problem.

3.3.2 Møller–Plesset Perturbation Theory

Rayleigh–Schrödinger perturbation theory [22] in quantum mechanics refers to the mathematical method of obtaining the solution of a complex Hamiltonian, by approximating

it with a simpler one. The idea is that the solution of the simpler system is known and an approximate solution of the perturbed Hamiltonian can be added as a correction, often in the form of an asymptotic expansion. In the context of electronic structure theory perturbation theory is applied to approximate the electronic correlation energy E_c. When the unperturbed Hamiltonian is the sum of all Fock operators, defined in Eq. (3.21), one then speaks of Møller–Plesset perturbation theory [23, 24].

The zeroth order Hamiltonian is defined as

$$\hat{\mathcal{H}}^{(0)} = \sum_{i}^{\text{occ.}} \hat{f}(i) \ , \tag{3.38}$$

and the perturbation as

$$\hat{\mathcal{V}} = \hat{\mathcal{H}} - \hat{\mathcal{H}}^{(0)} \ . \tag{3.39}$$

The canonical HF orbitals ψ_i are eigenfunctions of the Fock operator and thus the HF Slater determinant Φ is an eigenstate $\Psi^{(0)}$ of the zeroth order Hamiltonian $\hat{\mathcal{H}}^{(0)}$

$$\hat{\mathcal{H}}^{(0)}\Psi^{(0)} = E^{(0)}\Psi^{(0)} \ . \tag{3.40}$$

$E^{(0)}$ is the zeroth order energy and is the sum of the one-particle orbital eigenenergies

$$E^{(0)} = \sum_{i}^{\text{occ.}} \varepsilon_i \ . \tag{3.41}$$

The first order correction to the zeroth Hamiltonian yields the HF energy (see Appendix B)

$$\langle\Psi^{(0)}|\hat{\mathcal{H}}^{(0)}|\Psi^{(0)}\rangle + \langle\Psi^{(0)}|\hat{\mathcal{V}}|\Psi^{(0)}\rangle = E^{(0)} + E^{(1)} = E_{\text{HF}} \ . \tag{3.42}$$

In order to obtain the leading order correction to the HF energy the second order energy $E^{(2)}$ is needed. The expression for the second order energy reads (Appendix B)

$$\begin{aligned} E^{(2)} &= \langle\Psi^{(1)}|\hat{\mathcal{V}}|\Psi^{(0)}\rangle \\ &= \langle\Psi^{(1)}|\hat{\mathcal{H}} - \hat{\mathcal{H}}^{(0)}|\Psi^{(0)}\rangle \ . \end{aligned} \tag{3.43}$$

The above equations depend on the first order wavefunction, which can be expanded in the basis of excited Slater determinants

$$\Psi^{(1)} = \sum_{i}^{\text{occ.}}\sum_{a}^{\text{vir.}} t_i^a \Phi_i^a + \sum_{i<j}^{\text{occ.}}\sum_{a<b}^{\text{vir.}} t_{ij}^{ab}\Phi_{ij}^{ab} + \dots \ , \tag{3.44}$$

where $i, j, \dots$ and $a, b \dots$ refer to occupied and virtual one-electron states respectively. The excited Slater determinants are obtained by replacing occupied states ψ_i with virtual

(unoccupied) states ψ_a in the HF determinant. This is depicted schematically in Fig. 3.3. Inserting the ansatz of Eq. (3.44) in Eq. (B.8) and multiplying on the left with all excited Slater determinants $\langle\Phi_i^a|, \langle\Phi_{ij}^{ab}|, \dots$, the following equations for the first order wavefunction are obtained

$$\begin{aligned}
&\sum_{k}^{\text{occ.}}\sum_{c}^{\text{vir.}}\langle\Phi_i^a|\hat{\mathcal{H}}^{(0)} - E^{(0)}|\Phi_k^c\rangle t_k^c + \langle\Phi_i^a|\hat{\mathcal{H}}|\Phi\rangle = 0 \\
&\sum_{k>l}^{\text{occ.}}\sum_{c>d}^{\text{vir.}}\langle\Phi_{ij}^{ab}|\hat{\mathcal{H}}^{(0)} - E^{(0)}|\Phi_{kl}^{cd}\rangle t_{kl}^{cd} + \langle\Phi_{ij}^{ab}|\hat{\mathcal{H}}|\Phi\rangle = 0 \\
&\vdots
\end{aligned} \tag{3.45}$$

Slater determinants that are built from canonical HF orbitals are eigenstates of $\hat{\mathcal{H}}^{(0)}$, so that the first term on the left hand side of Eq. (3.45) yields

$$\begin{aligned}
&\sum_{k}^{\text{occ.}}\sum_{c}^{\text{vir.}}\langle\Phi_i^a|\hat{\mathcal{H}}^{(0)} - E^{(0)}|\Phi_k^c\rangle t_k^c = (\varepsilon_a - \varepsilon_i) t_i^a \\
&\sum_{k>l}^{\text{occ.}}\sum_{c>d}^{\text{vir.}}\langle\Phi_{ij}^{ab}|\hat{\mathcal{H}}^{(0)} - E^{(0)}|\Phi_{kl}^{cd}\rangle t_{kl}^{cd} = (\varepsilon_a + \varepsilon_b - \varepsilon_i - \varepsilon_j) t_{ij}^{ab} \ .
\end{aligned} \tag{3.46}$$

We thus arrive at the following result for the amplitudes

$$\begin{aligned}
t_i^a &= -\frac{\langle\Phi_i^a|\hat{\mathcal{H}}|\Phi\rangle}{(\varepsilon_a - \varepsilon_i)} \\
t_{ij}^{ab} &= -\frac{\langle\Phi_{ij}^{ab}|\hat{\mathcal{H}}|\Phi\rangle}{(\varepsilon_a + \varepsilon_b - \varepsilon_i - \varepsilon_j)} \ .
\end{aligned} \tag{3.47}$$

It should be noted that Slater determinants with more than double excitations yield zero amplitudes since the matrix element of the Hamiltonian with the HF reference determinant vanishes due to the Slater–Condon rules. Furthermore, for canonical HF orbitals singly excited amplitudes also vanish due to the Brillouin condition, i.e., $\langle\Phi_i^a|\hat{\mathcal{H}}|\Phi\rangle = \hat{f}_i^a = 0$. Consequently, we have arrived at the key result that only double excitations contribute to the first order wavefunction and the second order energy. The first order wavefunction is therefore given by

$$\Psi^{(1)} = \sum_{i<j}^{\text{occ.}}\sum_{a<b}^{\text{vir.}} t_{ij}^{ab}\Phi_{ij}^{ab} \ , \tag{3.48}$$

where the amplitudes are given by

$$t_{ij}^{ab} = -\frac{(\psi_i\psi_a|\psi_j\psi_b) - (\psi_j\psi_a|\psi_i\psi_b)}{\varepsilon_a + \varepsilon_b - \varepsilon_i - \varepsilon_j} \ . \tag{3.49}$$

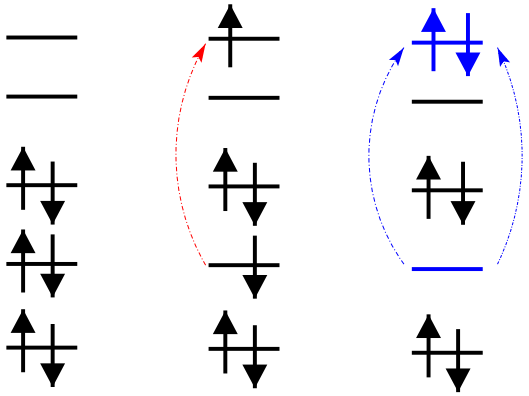

FIGURE 3.3: Schematic representation of different configurations. From left to right: The HF determinant ($|0\rangle$), singly, and doubly excited configurations.

The second order energy is thus

$$E^{(2)} = \langle \Psi^{(1)} | \hat{\mathcal{H}} | \Psi^{(0)} \rangle = \sum_{i<j}^{\text{occ.}} \sum_{a<b}^{\text{vir.}} t_{ij}^{ab} \langle \Phi_{ij}^{ab} | \hat{\mathcal{H}} | \Phi \rangle$$
$$= -\sum_{i<j}^{\text{occ.}} \sum_{a<b}^{\text{vir.}} \frac{\Big[(\psi_i \psi_a | \psi_j \psi_b) - (\psi_j \psi_a | \psi_i \psi_b) \Big]^2}{\varepsilon_a + \varepsilon_b - \varepsilon_i - \varepsilon_j} \,. \tag{3.50}$$

A closed shell expression can be formulated in terms of spatial orbitals. The second-order Møller–Plesset perturbation theory (MP2) correlation energy in Eq. (3.50) can be rewritten as

$$E^{(2)} = -\frac{1}{4} \sum_{i,j}^{\text{occ.}} \sum_{a,b}^{\text{vir.}} \frac{\Big[(\psi_i \psi_a | \psi_j \psi_b) - (\psi_j \psi_a | \psi_i \psi_b) \Big]^2}{\varepsilon_a + \varepsilon_b - \varepsilon_i - \varepsilon_j} \tag{3.51}$$
$$= -\frac{1}{2} \sum_{i,j}^{\text{occ.}} \sum_{a,b}^{\text{vir.}} \frac{(\psi_i \psi_a | \psi_j \psi_b) \Big[(\psi_i \psi_a | \psi_j \psi_b) - (\psi_j \psi_a | \psi_i \psi_b) \Big]}{\varepsilon_a + \varepsilon_b - \varepsilon_i - \varepsilon_j} \,, \tag{3.52}$$

where the sum runs over all occupied and virtual spin orbitals. Spin integration for a closed shell system yields

$$E^{(2)} = -\sum_{i,j}^{\text{occ.}} \sum_{a,b}^{\text{vir.}} \frac{(\phi_i \phi_a | \phi_j \phi_b) \Big[2\,(\phi_i \phi_a | \phi_j \phi_b) - (\phi_j \phi_a | \phi_i \phi_b) \Big]}{\varepsilon_a + \varepsilon_b - \varepsilon_i - \varepsilon_j} \,, \tag{3.53}$$

where the indices i, j, a, and b, run over the spatial orbitals ϕ. The total MP2 energy takes the form

$$E_{\text{MP2}} = E^{(0)} + E^{(1)} + E^{(2)} = E_{\text{HF}} + E^{(2)} \,. \tag{3.54}$$

MP2 theory forms the simplest perturbation expansion that captures correlation effects. In the lowest order only doubly excited determinants contribute, signifying that the most important correlation effects stem from independent electron pair excitations. MP2 theory provides a fair compromise between efficiency and accuracy, capturing non local vdW interactions. However, if the energy difference between the Highest Occupied Molecular Orbital (HOMO) and the Lowest Unoccupied Molecular Orbital (LUMO) (or the band gap in periodic systems) is small, MP2 theory is unsuccessful. Higher order perturbation expansions are also possible, however, they are computationally demanding. Coupled-cluster methods provide a more robust and accurate framework for treating electronic correlation, as will be seen in the next section.

3.3.3 Coupled cluster theory

While many-body perturbation theory offers a finite-order approximation to the electronic correlation, coupled-cluster (CC) theory [25–27] provides a compelling framework of infinite-order approximations in the form of an exponential of cluster operators. In the CC method the wavefunction is approximated using the exponential ansatz

$$|\Psi_{\mathrm{CC}}\rangle = \exp(\hat{T})|0\rangle \ , \tag{3.55}$$

where the cluster operator $\hat{T}$ is defined as

$$\hat{T} = \hat{T}_1 + \hat{T}_2 + \hat{T}_3 + \dots \ . \tag{3.56}$$

The contracted excitation operators create excited Slater determinants with coefficients $t_i^a, t_{ij}^{ab}, t_{ijk}^{abc}, \dots$.

$$\begin{aligned}
\hat{T}_1|\Psi^{\mathrm{HF}}\rangle &= \sum_i \sum_a t_i^a |\Psi_i^a\rangle \\
\hat{T}_2|\Psi^{\mathrm{HF}}\rangle &= \sum_{ij} \sum_{ab} t_{ij}^{ab} |\Psi_{ij}^{ab}\rangle \\
\hat{T}_3|\Psi^{\mathrm{HF}}\rangle &= \sum_{ijk} \sum_{abc} t_{ijk}^{abc} |\Psi_{ijk}^{abc}\rangle \\
&\vdots
\end{aligned} \tag{3.57}$$

The exponential of the cluster operator is given by the expansion

$$\exp(\hat{T}) = 1 + \hat{T} + \frac{1}{2!}\hat{T}\hat{T} + \frac{1}{3!}\hat{T}\hat{T}\hat{T} + \cdots \equiv \sum_0^\infty \frac{1}{n!}\hat{T}^n \ . \tag{3.58}$$

In principle the cluster operator $\hat{T}$ in Eq. (3.56) contains up to N-fold excitations for an N-electron system. Truncating the operator $\hat{T}$ at a certain number of excitations, i.e., singles, doubles, triples, etc., yields a hierarchy of CC methods, termed as CCSD, CCSDT, CCSDTQ etc.

3.3.3.1 Closed shell CCSD theory

Let us first take a look in the case of CCSD that includes single and double excitations. The CC ansatz for the wavefunction reads

$$|\Psi_{\mathrm{CCSD}}\rangle = \exp\left(\hat{T}_1 + \hat{T}_2\right)|0\rangle = \left(1 + \hat{T}_1 + \hat{T}_2 + \frac{1}{2!}\hat{T}_1^2 + \hat{T}_1\hat{T}_2 + \frac{1}{3!}\hat{T}_1^3 + \frac{1}{4!}\hat{T}_1^4 + \frac{1}{2!}\hat{T}_2^2 + \dots\right)|0\rangle \,. \tag{3.59}$$

The CCSD wavefunction contains up to N-fold excitations (for N electrons) as a result of the exponential ansatz, in the form of products of single and double excitations. Thus, CC energies of any order are size consistent. In order to determine the CC energy and the $\hat{T}_1$ and $\hat{T}_2$ amplitudes we insert the CC ansatz in the Schrödinger equation and project on the HF and singly and doubly excited determinants.

$$\begin{aligned}
\langle 0|\left(\hat{\mathcal{H}} - E_{\mathrm{CCSD}}\right)|\Psi_{\mathrm{CCSD}}\rangle &= 0 \\
\langle \Phi_i^a|\left(\hat{\mathcal{H}} - E_{\mathrm{CCSD}}\right)|\Psi_{\mathrm{CCSD}}\rangle &= 0 \\
\langle \Phi_{ij}^{ab}|\left(\hat{\mathcal{H}} - E_{\mathrm{CCSD}}\right)|\Psi_{\mathrm{CCSD}}\rangle &= 0 \,.
\end{aligned} \tag{3.60}$$

The first row of Eq. (3.60) yields the correlation energy

$$\begin{aligned}
E_{\mathrm{corr}} = E_{\mathrm{CCSD}} - E_{\mathrm{HF}} &= \langle 0|\left(\hat{\mathcal{H}} - E_{\mathrm{CCSD}}\right)|\Psi_{\mathrm{CCSD}}\rangle = \langle 0|\hat{\mathcal{H}}\left(\frac{1}{2}\hat{T}_1^2 + \hat{T}_2\right)|0\rangle \\
&= \sum_{i,j}^{\mathrm{occ.}}\sum_{a,b}^{\mathrm{vir.}}\left(\frac{1}{2}t_i^a t_j^b + t_{ij}^{ab}\right)\Big[2\left(\phi_i\phi_a|\phi_j\phi_b\right) - \left(\phi_j\phi_a|\phi_i\phi_b\right)\Big] \,.
\end{aligned} \tag{3.61}$$

This energy formula is valid for any CC ansatz, since according to the Slater-Condon rules higher that double excitations have vanishing matrix elements. The expression is very similar to the MP2 one in Eq. (3.50), albeit the doubles amplitudes are computed differently.

In CCSD the amplitudes are computed from Eq. (3.60). These equations lead to a set of non linear equations that can be solved iteratively. One can reformulate these equations by multiplying the Schrödinger equation from the left with $e^{-\hat{T}}$. Employing the identity

$e^{-\hat{T}}e^{\hat{T}} = 1$, the equations are transformed to

$$\begin{aligned}\langle 0|e^{-\hat{T}}\hat{\mathcal{H}}e^{\hat{T}}|0\rangle &= E_{\mathrm{CCSD}} \\ \langle \Phi_i^a|e^{-\hat{T}}\hat{\mathcal{H}}e^{\hat{T}}|0\rangle &= 0 \\ \langle \Phi_{ij}^{ab}|e^{-\hat{T}}\hat{\mathcal{H}}e^{\hat{T}}|0\rangle &= 0\ .\end{aligned} \tag{3.62}$$

Here, $e^{-\hat{T}}\hat{\mathcal{H}}e^{\hat{T}}$ is a similarity transformed Hamiltonian. The energy expression stays intact. The singles and doubles amplitude equations can be solved iteratively by optimizing the amplitudes. For this to happen the residuals, defined below, have to vanish

$$\begin{aligned}r_i^a &= \langle \Phi_i^a|e^{-\hat{T}}\hat{\mathcal{H}}e^{\hat{T}}|0\rangle \\ r_{ij}^{ab} &= \langle \Phi_{ij}^{ab}|e^{-\hat{T}}\hat{\mathcal{H}}e^{\hat{T}}|0\rangle\ .\end{aligned} \tag{3.63}$$

The residuals are computed in every iteration and the CCSD amplitudes are updated as following

$$\begin{aligned}r_i^a &= t_i^a - \underbrace{\frac{R_i^a(t_i^a)}{\varepsilon_a - \varepsilon_i}}_{\text{New amplitudes } t_i^a} \\ r_{ij}^{ab} &= t_{ij}^{ab} - \underbrace{\frac{R_{ij}^{ab}(t_{ij}^{ab})}{\varepsilon_a + \varepsilon_b - \varepsilon_i - \varepsilon_j}}_{\text{New amplitudes } t_{ij}^{ab}}\ ,\end{aligned} \tag{3.64}$$

where R_i^a and R_{ij}^{ab} are computed using the amplitudes t_i^a and t_{ij}^{ab}. The equations for R_i^a and R_{ij}^{ab} are given below. After the first iteration, R_{ij}^{ab} are just the two electron integrals $(\phi_i\phi_a|\phi_j\phi_b)$ and the amplitudes the MP2 ones. This procedure works well when the MP2 amplitudes are a reasonably good starting point. This is often the case for systems with a large HOMO-LUMO gap (or band gap in periodic systems). The iterative procedure can either be accelerated using the direct inversion in the iterative subspace (DIIS) method [28], or even converge in cases that the normal one can diverge.

The doubles amplitudes in Eq. (3.62) involve up to quadruple excitations since Hamiltonian matrix elements vanish if the Slater determinants differ by more than two orbitals. Similarly singles amplitudes involve up to triple excitations. The Baker–Campbell–Hausdorff (BCH) expansion reads

$$e^{-\hat{T}}\hat{\mathcal{H}}e^{\hat{T}} = \hat{\mathcal{H}} + \big[\hat{T},\hat{\mathcal{H}}\big] + \frac{1}{2!}\Big[\big[\hat{\mathcal{H}},\hat{T}\big],\hat{T}\Big] + \frac{1}{3!}\Big[\Big[\big[\hat{\mathcal{H}},\hat{T}\big],\hat{T}\Big],\hat{T}\Big] + \frac{1}{4!}\Big[\Big[\Big[\big[\hat{\mathcal{H}},\hat{T}\big],\hat{T}\Big],\hat{T}\Big],\hat{T}\Big]\ . \tag{3.65}$$

It is noted that this expansion truncates after fourth order. The reason is that the Hamiltonian $\hat{\mathcal{H}}$ includes a two-body operator. Using the BCH formula one can derive the amplitudes equations. However, that is a tedious task, owing to a large number of

terms involved. Unlike MP2 theory where the amplitudes depend only on the $(\phi_i\phi_a|\phi_j\phi_b)$ integrals, the CCSD residuals demand all possible two electron integrals, ranging from zero to four virtual orbitals. It is possible to derive a closed shell expression for the singles and doubles amplitudes in Eq. (3.62). Here the equations from the work of Hirata *et. al.* [29] are employed.

$$\begin{aligned} R_i^a =& \sum_c \kappa_c^a t_i^c - \sum_k \kappa_i^k t_k^a + \sum_{kc} \kappa_c^k \left(2t_{ki}^{ca} - t_{ik}^{ca}\right) + \sum_{kc} \kappa_c^k t_i^c t_k^a + \sum_{kc} w_{ic}^{ak} t_k^c + \\ & \sum_{kcd} w_{cd}^{ak} t_{ik}^{cd} + \sum_{kcd} w_{cd}^{ak} t_i^c t_k^d - \sum_{klc} w_{ic}^{kl} t_{kl}^{ac} - \sum_{klc} w_{ic}^{kl} t_k^a t_l^c \end{aligned} \tag{3.66}$$

$$\begin{aligned} R_{ij}^{ab} =& v_{ij}^{ab} + \sum_{kl} \chi_{ij}^{kl} t_{kl}^{ab} + \sum_{kl} \chi_{ij}^{kl} t_k^a t_l^b + \sum_{cd} \chi_{cd}^{ab} t_{ij}^{cd} + \sum_{cd} \chi_{cd}^{ab} t_i^c t_j^d + P \sum_c \lambda_c^a t_{ij}^{cb} - \\ & P \sum_k \lambda_i^k t_{kj}^{ab} + P \sum_c \left(v_{ic}^{ab} - \sum_k v_{ic}^{kb} t_k^a\right) t_j^c - P \sum_k \left(v_{ij}^{ak} + \sum_c v_{ij}^{ak} t_j^c\right) t_k^b + \\ & P \sum_{kc} \left(2\chi_{ic}^{ak} - \chi_{ci}^{ak}\right) t_{kj}^{cb} - P \sum_{kc} \chi_{ic}^{ak} t_{kj}^{bc} - P \sum_{kc} \chi_{ci}^{bk} t_{kj}^{ac} \end{aligned} \tag{3.67}$$

$$\begin{aligned} \kappa_i^k &= \sum_{lcd} w_{cd}^{kl} t_{il}^{cd} + \sum_{lcd} w_{cd}^{kl} t_i^c t_l^d \\ \kappa_c^a &= \sum_{kld} w_{cd}^{kl} t_{kl}^{ad} + \sum_{kld} w_{cd}^{kl} t_k^a t_l^d \\ \kappa_c^k &= \sum_{ld} w_{cd}^{kl} t_l^d \\ \lambda_i^k &= \kappa_i^k + \sum_{lc} w_{ic}^{kl} t_l^c \\ \lambda_c^a &= \kappa_c^a + \sum_{kd} w_{cd}^{ak} t_k^d \\ \chi_{ij}^{kl} &= v_{ij}^{kl} + \sum_c v_{ic}^{kl} t_j^c + \sum_c v_{cj}^{kl} t_i^c + \sum_{cd} v_{cd}^{kl} t_{ij}^{cd} + \sum_{cd} v_{cd}^{kl} t_i^c t_j^d \\ \chi_{cd}^{ab} &= v_{cd}^{ab} - \sum_k v_{cd}^{ak} t_k^b - \sum_k v_{cd}^{kb} t_k^a \\ \chi_{ic}^{ak} &= v_{ic}^{ak} - \sum_l v_{ic}^{lk} t_l^a + \sum_d v_{dc}^{ak} t_i^d - \frac{1}{2} \sum_{ld} v_{dc}^{lk} t_{il}^{da} - \sum_{ld} v_{dc}^{lk} t_i^d t_l^a + \frac{1}{2} \sum_{ld} w_{dc}^{lk} t_{il}^{ad} \\ \chi_{ci}^{ak} &= v_{ci}^{ak} - \sum_l v_{ci}^{lk} t_l^a + \sum_d v_{cd}^{ak} t_i^d - \frac{1}{2} \sum_{ld} v_{cd}^{lk} t_{il}^{da} - \frac{1}{2} \sum_{ld} w_{dc}^{lk} t_i^d t_l^a \ , \end{aligned} \tag{3.68}$$

where v_{sr}^{pq} are the two electron integrals defined by

$$v_{sr}^{pq} = (\phi_p\phi_s|\phi_q\phi_r)\,, \tag{3.69}$$

and w_{sr}^{pq} the antisymmetrized two electron integrals given by

$$w_{sr}^{pq} = 2\,(\phi_p\phi_s|\phi_q\phi_r) - (\phi_p\phi_r|\phi_q\phi_s) \ . \tag{3.70}$$

P is the permutation operator

$$P\left\{\dots\right\}_{ij}^{ab} = \left\{\dots\right\}_{ij}^{ab} + \left\{\dots\right\}_{ji}^{ba} \ . \tag{3.71}$$

The most expensive term is $v_{cd}^{ab}t_{ij}^{cd}$ (a contraction over repeated indices is assumed) that requires $N_{\mathrm{v}}^4 N_{\mathrm{o}}^2$ operations, since usually the number of virtual one electron states is much larger than the occupied ones. Then come terms that require $N_{\mathrm{v}}^3 N_{\mathrm{o}}^3$, such as $v_{cd}^{ak}t_k^b t_{ij}^{cd}$. Since N_{v} and N_{o} scale linearly with the system size, the computational complexity of the CCSD method is $\mathcal{O}(N^6)$, where N is a measure of the system. One can include higher excitations in the CC method, however, the scaling increases by two for each additional excitation. Thus, CCSDT scales as $\mathcal{O}(N^8)$, CCSDTQ as $\mathcal{O}(N^{10})$, etc.

3.3.3.2 Closed shell CCSD(T) theory

Another popular scheme to go beyond double exciations in CCSD theory is to evaluate the highest excitation level in a non iterative perturbative way. In Møller–Plesset perturbation theory up to third order, electronic correlation arises from single and double excitations only. The CCSD method includes all these contributions, hence it is exact up to third order perturbation theory. Fourth and fifth order contributions arise from single, double, triple, and quadrupole exciations. Raghavachari *et. al.* [30] have proposed a technique using triple excitations correction on top of the CCSD wavefunction. This gives rise to the CCSD(T) scheme. The CCSD(T) energy reads

$$E^{\mathrm{CCSD(T)}} = E^{\mathrm{CCSD}} + \Delta E^{\mathrm{CCSD(T)}} \ , \tag{3.72}$$

where $\Delta E^{\mathrm{CCSD(T)}}$ denotes the perturbative correction. We follow the equations from Piecuch *et. al.* [31]

$$\Delta E^{\mathrm{CCDS(T)}} = \bar{t}_{abc}^{ijk} t_{ijk}^{abc} D_{ijk}^{abc} + \bar{z}_{abc}^{ijk} t_{ijk}^{abc} D_{ijk}^{abc} \ , \tag{3.73}$$

where t_{ijk}^{abc} are the spin-free amplitudes, given by

$$D_{ijk}^{abc} t_{ijk}^{abc} = P(ia/jb/kc)\left[t_{ij}^{ae} v_{ek}^{bc} - t_{im}^{ab} v_{jk}^{mc}\right] \ , \tag{3.74}$$

with $P(ia/jb/kc)$ being the permutation operator

$$P(ia/jb/kc) = 1 + (ij)(ab) + (ik)(ac) + (jk)(bc) + (ijk)(abc) + (ikj)(acb) \ . \tag{3.75}$$

For any six-index tensor χ_{ijk}^{abc} we have defined

$$\bar{\chi}_{abc}^{ijk} = \frac{4}{3}\chi_{abc}^{ijk} - 2\chi_{acb}^{ijk} + \frac{2}{3}\chi_{bca}^{ijk} \ . \tag{3.76}$$

The CCSD(T) method scales as $\mathcal{O}(N^7)$, whereas the CCSDT(Q) method as $\mathcal{O}(N^9)$. The CCSD(T) method achieves chemical accuracy in the description of many molecular properties and is often referred to as the gold standard method. It is the scope of this thesis to implement and apply a periodic CCSD(T) method using a plane-wave basis.

Chapter 4

The PAW Method

An implementation of correlated methods, such the CC method, in a plane-wave basis within the projector augmented wave (PAW) framework in the VASP code is discussed in this Chapter. In any computer implementation the one-particle orbitals are expanded in a basis. In solids the one-particle orbitals are Bloch orbitals, i.e., they obey the Bloch theorem

$$\langle \mathbf{r} + \mathbf{R} | \psi_\alpha \rangle = \langle \mathbf{r} | \psi_\alpha \rangle e^{i \mathbf{k}_\alpha \mathbf{R}} \ , \tag{4.1}$$

where α stands for a shorthand notation of the band index n_α and the wave vector $\mathbf{k}_\alpha$. Although the wave vector is usually chosen to lie in the first Brillouin zone, one can instead increase the unit cell size in order to approximate the infinite system. In this work we will be concerned with quantum chemical methods within the Γ-point approximation, i.e,

$$\langle \mathbf{r} + \mathbf{R} | \psi_\alpha \rangle = \langle \mathbf{r} | \psi_\alpha \rangle \ , \tag{4.2}$$

where α stands for the band index. A very convenient basis for expanding one-electron orbitals for periodic systems is plane-waves. They are eigenfunctions of the kinetic energy operator, and naturally fulfil the periodicity of the computational cell, as required by Bloch theorem. Furthermore, plane-waves are independent of the atomic composition of the computational cell, depending only on its geometry. The Bloch orbitals can be expanded using the plane-wave basis as

$$\langle \mathbf{r} | \psi_\alpha \rangle = \frac{1}{\sqrt{\Omega}} \sum_{\mathbf{G}} C_\alpha^{\mathbf{G}} e^{i \mathbf{G} \mathbf{r}} \ . \tag{4.3}$$

A major disadvantage of using plane-waves is that the description of the full Coulomb electron–ion interaction is computationally demanding. Expanding the Bloch orbitals in terms of plane-waves, would require a large number of Fourier components because the potential becomes very strong inside the core-ion region, resulting in short wavelength

oscillations of the corresponding orbitals in that region. Instead, pseudopotentials are used to describe the interaction between valence electrons and ionic cores. This reduces the number of Fourier components needed to describe the valence one-electron states close to the ionic core region [32, 33].

4.1 The PAW Method

The full potential PAW formalism was first proposed by Blöchl [34], while its close correspondence to Vanderbilt's usltrasoft pseudopotential (USPP) method [35] was formally shown by Kresse and Joubert [36].

In the PAW method the space is divided into two regions. The augmentation (PAW) spheres and the interstitial regions. The one-electron orbitals $|\psi_\alpha\rangle$ are derived from the pseudo-orbitals $|\tilde{\psi}_\alpha\rangle$ by means of a linear transformation [34, 36]

$$|\psi_\alpha\rangle = |\tilde{\psi}_\alpha\rangle + \sum_i \big(|\phi_i\rangle - |\tilde{\phi}_i\rangle\big)\langle \tilde{p}_i|\tilde{\psi}_\alpha\rangle \ , \tag{4.4}$$

where i is a shorthand notation for the atomic site $\mathbf{R}_i$, the angular momentum quantum numbers l_i and m_i, and the reference energy ε_i. The pseudo-orbitals $|\tilde{\psi}_\alpha\rangle$ are the variational quantities and are expanded using plane-waves

$$\langle \mathbf{r}|\tilde{\psi}_\alpha\rangle = \frac{1}{\sqrt{\Omega}} \sum_{\mathbf{G}} C_\alpha^{\mathbf{G}} e^{i\mathbf{G}\mathbf{r}} \ . \tag{4.5}$$

In the interstitial region the pseudo-orbitals are identical to the exact full potential orbitals ψ_α, while in the PAW spheres they are mapped onto the corresponding exact full potential orbitals via Eq. (4.4). The all-electron (AE) partial-waves ϕ_i are solutions of the radial Schrödinger equation for a reference atom at a reference energy ε_i and an angular momentum l_i

$$\langle \mathbf{r}|\phi\rangle = \frac{1}{|\mathbf{r}-\mathbf{R}_i|} u_{l_i \varepsilon i}\big(|\mathbf{r}-\mathbf{R}_i|\big) Y_{l_i m_i}\big(\widehat{\mathbf{r}-\mathbf{R}_i}\big) \ . \tag{4.6}$$

The notation $\widehat{\mathbf{r}-\mathbf{R}_i}$ indicates that the spherical harmonics $Y_{l_i m_i}$ depend only on the orientation and not on the length of the vector $\mathbf{r}-\mathbf{R}_i$. The pseudo-partial-waves $\tilde{\phi}_i$ are equivalent to ϕ_i outside the core radius r_c, that defines the PAW spheres

$$\langle \mathbf{r}|\tilde{\phi}\rangle = \frac{1}{|\mathbf{r}-\mathbf{R}_i|} \tilde{u}_{l_i \varepsilon i}\big(|\mathbf{r}-\mathbf{R}_i|\big) Y_{l_i m_i}\big(\widehat{\mathbf{r}-\mathbf{R}_i}\big) \ . \tag{4.7}$$

The projector functions $\tilde{p}_i$ in Eq.(4.4) are constructed in such a way that they are dual to the pseudo-partial-waves

$$\langle \tilde{p}_i | \tilde{\phi}_j \rangle = \delta_{ij} \ . \tag{4.8}$$

The electron overlap density related to two orbitals a and b,

$$n_{ab}(\mathbf{r}) = \langle \psi_a | \mathbf{r} \rangle \langle \mathbf{r} | \psi_b \rangle \ , \tag{4.9}$$

can be written as (for details the reader is referred to Ref [36])

$$n_{ab}(\mathbf{r}) = \tilde{n}_{ab}(\mathbf{r}) - n^1_{ab}(\mathbf{r}) + \tilde{n}^1_{ab}(\mathbf{r}) \ , \tag{4.10}$$

where

$$\begin{aligned} \tilde{n}_{ab}(\mathbf{r}) =& \langle \tilde{\psi}_a | \mathbf{r} \rangle \langle \mathbf{r} | \tilde{\psi}_b \rangle \\ \tilde{n}^1_{ab}(\mathbf{r}) =& \sum_{ij} \langle \tilde{\phi}_i | \mathbf{r} \rangle \langle \mathbf{r} | \tilde{\phi}_j \rangle \langle \tilde{\psi}_a | \tilde{p}_i \rangle \langle \tilde{p}_j | \tilde{\psi}_b \rangle \\ n^1_{ab}(\mathbf{r}) =& \sum_{ij} \langle \phi_i | \mathbf{r} \rangle \langle \mathbf{r} | \phi_j \rangle \langle \tilde{\psi}_a | \tilde{p}_i \rangle \langle \tilde{p}_j | \tilde{\psi}_b \rangle \ . \end{aligned} \tag{4.11}$$

Densities with a superscript 1 are quantities that are evaluated on a radial grid inside the PAW spheres. The summation over i and j is restricted to pairs that belong to the same site ($\mathbf{R}_i = \mathbf{R}_j$). For a correct treatment of the long range electrostatics, a compensation density $\hat{n}$ is introduced in such a way, so that $\tilde{n}_{ab} + \hat{n}_{ab}$ has the same multiple moments as n^1_{ab} in the PAW spheres. Details of the construction of the compensation density in the VASP code are given in Ref. [36]. For a more efficient implementation it is important to compute separately the energy in the PAW spheres and the plane-wave grid. It is thus required to add and subtract the compensation charge in Eq. (4.12) leading to the following formula for the density

$$n_{ab}(\mathbf{r}) = \left[\tilde{n}_{ab}(\mathbf{r}) + \hat{n}_{ab}(\mathbf{r})\right] + n^1_{ab}(\mathbf{r}) - \left[\tilde{n}^1_{ab}(\mathbf{r}) + \hat{n}^1_{ab}(\mathbf{r})\right] \ . \tag{4.12}$$

4.2 The PAW DFT energy

The final expression for the total energy in Kohn–Sham DFT can thus be split into three terms using the electronic density from Eq. (4.12)

$$E = \widetilde{E} + E^1 - \widetilde{E}^1 \ . \tag{4.13}$$

The first term is evaluated on a regular plane-wave grid, whereas the last two terms are computed on atom centered radial logarithmic grids inside the PAW spheres. The three

parts of the energy functional of Eq. (3.3) take the following form

$$\tilde{E} = -\frac{1}{2}\sum_n \langle\tilde{\psi}_n|\nabla^2|\tilde{\psi}_n\rangle + E_{\rm xc}\big[\tilde{n}+\hat{n}+\tilde{n}_{\rm c}\big] + E_{\rm H}\big[\tilde{n}+\hat{n}\big] + \int v_{\rm H}[\tilde{n}_{Zc}]\big[\tilde{n}(\mathbf{r})+\hat{n}(\mathbf{r})\big]{\rm d}\mathbf{r} + U\big(\mathbf{R}, Z_{\rm ion}\big) \ , \tag{4.14}$$

$$\tilde{E}^1 = -\frac{1}{2}\sum_{(i,j)} \rho_{ij}\langle\tilde{\phi}_i|\nabla^2|\tilde{\phi}_j\rangle + \overline{E_{\rm xc}\big[\tilde{n}^1+\hat{n}+\tilde{n}_{\rm c}\big]} + \overline{E_{\rm H}\big[\tilde{n}^1+\hat{n}\big]} + \int v_{\rm H}[\tilde{n}_{Zc}]\big[\tilde{n}^1(\mathbf{r})+\hat{n}(\mathbf{r})\big]{\rm d}\mathbf{r} \ , \tag{4.15}$$

$$E^1 = -\frac{1}{2}\sum_{(i,j)} \rho_{ij}\langle\phi_i|\nabla^2|\phi_j\rangle + \overline{E_{\rm xc}\big[n^1+n_{\rm c}\big]} + \overline{E_{\rm H}\big[n^1\big]} + \int v_{\rm H}[n_{Zc}]n^1(\mathbf{r}){\rm d}\mathbf{r} \ , \tag{4.16}$$

where ρ_{ij} can be thought as the one-electron reduced density matrix at each atomic site, and is given by

$$\rho_{ij} = \sum_n f_n\langle\tilde{\psi}_n|\tilde{p}_i\rangle\langle\tilde{p}_j|\tilde{\psi}_n\rangle \ , \tag{4.17}$$

with f_n being the occupancies of the pseudo-orbitals $\tilde{\psi}_n$, with band index n. $n_{\rm c}$ is the charge density of the frozen core AE wavefuctions of the reference atom, while $\tilde{n}_{\rm c}$ is the partial charge density of the core electrons. n_{Zc} is the point charge density of the nucleus n_Z plus the frozen core AE charge density $n_{\rm c}$ and $\tilde{n}_{Zc}$ is the pseudized core density. Overlined terms are evaluated on a radial grid. The Hartree potential and the Hartree energy of a density n are defined as

$$\begin{aligned} v_{\rm H}[n](\mathbf{r}) &= \int \frac{n(\mathbf{r}')}{|\mathbf{r}-\mathbf{r}'|}{\rm d}r' \ , \\ E_{\rm H}[n](\mathbf{r}) &= \frac{1}{2}\int\int \frac{n(\mathbf{r})n(\mathbf{r}')}{|\mathbf{r}-\mathbf{r}'|}{\rm d}r{\rm d}r' \ . \end{aligned} \tag{4.18}$$

The above expression for the energy holds for LDA- and GGA-DFT methods. For the HF method, as well as for the wavefunction correlated techniques, the two-electron integrals are also needed.

4.3 Two-electron integrals in PAW

In order to obtain the HF energy within the PAW method the E_{xc} energy expression in the Kohn Sham DFT has to be replaced by the exact exchange energy expression, given in Eq. (3.14). Furthermore, for correlated methods, such as the CC method, the evaluation of all possible two-electron integrals is needed.

The two-electron integrals for a periodic system, within the Γ-point approximation are defined as

$$V_{rs}^{pq} = \int\int \psi_p(\mathbf{r})\psi_q(\mathbf{r}')\frac{1}{|\mathbf{r}-\mathbf{r}'|}\psi_r(\mathbf{r}')\psi_s(\mathbf{r})\mathrm{d}\mathbf{r}\mathrm{d}\mathbf{r}' \ , \tag{4.19}$$

where p, q, r, s refer to the band index.

Within the PAW method, the overlap density $n_{pr}(\mathbf{r}) = \psi_p(\mathbf{r})\psi_r(\mathbf{r})$ can be written as (see Eq. (4.12))

$$n_{pr}(\mathbf{r}) = \left[\tilde{n}_{pr}(\mathbf{r}) + \hat{n}_{pr}(\mathbf{r})\right] + n^1_{pr}(\mathbf{r}) - \left[\tilde{n}^1_{pr}(\mathbf{r}) + \hat{n}_{pr}(\mathbf{r})\right] \ . \tag{4.20}$$

Introducing the following notation for the two-electron integrals in terms of overlapping densities

$$\{n_{pr}\}\{n_{qs}\} = \int\int \frac{n_{pr}(\mathbf{r})n_{qs}(\mathbf{r}')}{|\mathbf{r}-\mathbf{r}'|}\mathrm{d}\mathbf{r}\mathrm{d}\mathbf{r}' \ , \tag{4.21}$$

the integrals V_{rs}^{pq} in the PAW method can be expressed as

$$\begin{aligned}\{n_{pr}\}\{n_{qs}\} =& \{\tilde{n}_{pr} + \hat{n}_{pr}\}\{\tilde{n}_{qs} + \hat{n}_{qs}\} - \{\tilde{n}^1_{pr} + \hat{n}^1_{pr}\}\{\tilde{n}^1_{qs} + \hat{n}^1_{qs}\} \\ &+ \{n^1_{pr}\}\{n^1_{qs}\} \ .\end{aligned} \tag{4.22}$$

It is stressed that the integrals are composed from three contributions that are either calculated on a plane-wave basis (first term) or on a partial-wave basis in the PAW spheres (second and third terms). The integrals can thus be decomposed into three terms

$$V_{rs}^{pq} = \widetilde{V}_{rs}^{pq} - {}^1\widetilde{V}_{rs}^{pq} + {}^1V_{rs}^{pq} \ , \tag{4.23}$$

where

$$\begin{aligned}\widetilde{V}_{rs}^{pq} =& \{\tilde{n}_{pr} + \hat{n}_{pr}\}\{\tilde{n}_{qs} + \hat{n}_{qs}\} \\ {}^1\widetilde{V}_{rs}^{pq} =& \{\tilde{n}^1_{pr} + \hat{n}^1_{pr}\}\{\tilde{n}^1_{qs} + \hat{n}^1_{qs}\} \\ {}^1V_{rs}^{pq} =& \{n^1_{pr}\}\{n^1_{qs}\} \ .\end{aligned} \tag{4.24}$$

For a detailed derivation of the above integrals the reader is referred to Refs. [37, 38].

Harl derived an expression, whereby all three contributions can be approximated on a plane-wave grid [39]. In a plane-wave basis these integrals can be expressed as

$$V_{rs}^{pq} = \frac{1}{\Omega} \sum_{\mathbf{G}} C_{pr}(\mathbf{G}) v(\mathbf{G}) C_{qs}(-\mathbf{G}) \ , \tag{4.25}$$

where $v(\mathbf{G}) = \frac{4\pi}{\mathbf{G}^2}$ is the Coulomb kernel in reciprocal space and $C_{pr}(\mathbf{G})$ is the Fourier transform of the overlap density $n_{pr}(\mathbf{r}) = \psi_p(\mathbf{r})\psi_r(\mathbf{r})$

$$C_{pr}(\mathbf{G}) = \int_{\Omega} e^{-i\mathbf{G}\mathbf{r}} \psi_p(\mathbf{r})\psi_r(\mathbf{r}) \mathrm{d}\mathbf{r} \ . \tag{4.26}$$

Defining the Coulomb vertex as

$$\Gamma_{pr}(\mathbf{G}) = \sqrt{\frac{1}{\Omega}}\sqrt{\frac{4\pi}{\mathbf{G}^2}} C_{pr}(\mathbf{G}) = \sqrt{\frac{1}{\Omega}}\sqrt{\frac{4\pi}{\mathbf{G}^2}} \int_{\Omega} e^{-i\mathbf{G}\mathbf{r}} \psi_p(\mathbf{r})\psi_r(\mathbf{r}) \mathrm{d}\mathbf{r} \ , \tag{4.27}$$

the Coulomb integrals can be separated as

$$V_{rs}^{pq} = \sum_{\mathbf{G}} \Gamma_{ps}(\mathbf{G}) \Gamma_{qr}(-\mathbf{G}) \ , \tag{4.28}$$

or in the Einstein notation as

$$V_{rs}^{pq} = \Gamma^{*pG}_{\ r} \Gamma^{q}_{\ sG} \ , \tag{4.29}$$

where a sum over repeated indices is assumed, and G denotes the reciprocal lattice vectors $\mathbf{G}$. Thus, the integrals V_{rs}^{pq} can be expressed via Eq.(4.29), where the Fourier transformed overlap densities $C_{pr}(\mathbf{G})$ contain all three contributions of the PAW method. The plane-wave expansion of the overlap densities $C_{pr}(\mathbf{G})$ is done on a discrete grid and is truncated by a kinetic energy cutoff E_χ, such that $\frac{1}{\mathbf{G}^2} \leq E_\chi$. It is noted that the above approximation is of the same algebraic form as obtained by Cholesky decomposition [40–42] or density fitting [43–45] methods for the calculation of the Coulomb integrals employing atom centered basis sets. However, in the case of plane-wave basis sets, Eq. (4.29) can be derived directly from Eq. (4.19) via a series of Fourier transforms.

The exchange energy E_x per unit cell for a periodic system, within the Γ-point approximation is defined as

$$E_\mathrm{x} = -\sum_{ij}^{\mathrm{occ.}} \int\int \psi_i(\mathbf{r})\psi_j(\mathbf{r}') \frac{1}{|\mathbf{r}-\mathbf{r}'|} \psi_i(\mathbf{r}')\psi_j(\mathbf{r}) \mathrm{d}\mathbf{r}\mathrm{d}\mathbf{r}' \ . \tag{4.30}$$

where i, j refer to the band index of all occupied states. Within the PAW formalism and using the Γ-point approximation the integral takes the form

$$V_{ii}^{jj} = \frac{4\pi}{\Omega} \sum_{\mathbf{G}} \frac{C_{ij}(\mathbf{G})\ C_{ij}(-\mathbf{G})}{\mathbf{G}^2} = \sum_{G} \Gamma^{*jG}_{\ i} \Gamma^{j}_{\ iG} \ , \tag{4.31}$$

where

$$C_{ij}(\mathbf{G}) = \int_{\Omega} e^{-i\mathbf{G}\mathbf{r}} \psi_i(\mathbf{r}) \psi_j(\mathbf{r}) \mathrm{d}\mathbf{r} \ . \tag{4.32}$$

The potential is singular for $\mathbf{G} = 0$, when $i = j$. In the limit of an infinitely fine $\mathbf{G}$-mesh, these singularities are integrable and the exact exchange energy is well defined. In order to speed up the convergence of the exchange energy, a singularity correction computing using the probe-charge Ewald-sum method is employed [37, 46] (the reader is referred to Ref. [46] for a comparison of this and related methods). Throughout the thesis this scheme is used to estimate the $\mathbf{G} = 0$ component. Finally, it is stressed that apart from the exchange energy, the coupled cluster equations involve integrals of the form V_{cd}^{ab} and V_{ij}^{kl}, where all four indices may coincide leading to the same divergence. The probe-charge Ewald-sum method is used in that case as well.

Chapter 5

Periodic coupled-cluster implementation for extended systems

In the previous Chapters, we have seen methods to solve the electronic Schrödinger equation of a molecular or periodic quantum system, within the Born–Oppenheimer approximation. HF theory approximates the many-electron wavefunction by a single Slater determinant, whereas wavefunction-based correlated methods, such as the CC method, approximate the exact configuration interaction wavefunction coefficients in the Slater determinant basis, via the exponential ansatz. We have seen that for a periodic system a very convenient basis to expand one-particle orbitals are plane-waves. The two-electron integrals are approximated naturally within the PAW method in the form of $V_{rs}^{pq} = \sum_G \Gamma_r^{*pG} \Gamma_{sG}^q$, where p, q, r, s denote orbital indices, and the summation runs over reciprocal lattice vectors G.

In this Chapter an implementation of CCSD, whereby the Coulomb vertex is calculated within the PAW method, is presented. A procedure to reduce the number of momentum grid points G of the Coulomb vertex Γ_r^{pG} based on a singular value decomposition (SVD) is outlined. Afterwards a tensor rank decomposition of the Coulomb vertex into a product of three second-order tensors that allows partly a scaling reduction of the CCSD algorithm is introduced. In order to demonstrate the accuracy and efficiency of these approximations water adsorption on hexagonal Boron Nitride (h-BN) sheet, a typical example of weak molecular physisorption on an insulating two-dimensional surface, is studied.

5.1 Optimized Auxiliary Field Approximation

The expression of the Coulomb integrals using the Γ-point approximation within the PAW method is derived in Eq. (4.29). G denotes the momentum grid points $\mathbf{G}$ which are truncated according to a kinetic energy cutoff E_χ. Since the plane-wave expansion of the two-electron integrals carries no information about the atomic composition of the computational supercell, an approach for a more compact set of auxiliary field variables F is presented that can approximate the integrals with fewer relevant elements than the plane-wave expansion, without compromising accuracy. This is particularly true in studies of surfaces where a huge vacuum is required in order to avoid the interaction of the surface with its spurious periodic image, leading to a large number of plane-waves. We denote with $\tilde{\Gamma}_r^{pG}$ the unapproximated plane-wave expanded Coulomb vertex. Henceforth a sum over all free indices occurring at least twice within a product is implied, e.g.,

$$V_{sr}^{pq} = \tilde{\Gamma}^{*pG}_{\ s}\tilde{\Gamma}^{q}_{rG} =: \sum_G \tilde{\Gamma}^{*pG}_{\ s}\tilde{\Gamma}^{q}_{rG} \ . \tag{5.1}$$

Let

$$\tilde{\Gamma}^I_G = U^F_G \Sigma^J_F W^{*I}_{\ J} \ , \tag{5.2}$$

be a singular value decomposition of the Coulomb vertex $\tilde{\Gamma}^I_G$, written as a matrix with the compound index $I = (q, r)$, where the singular values in Σ are sorted in descending order. Taking only the largest $N_F < N_G$ singular values of the unapproximated Coulomb vertex $\tilde{\Gamma}$ into account we can define the *optimized auxiliary field (OAF) Coulomb vertex*

$$\Gamma^I_F := \Sigma^J_F W^{*I}_{\ J} = U^{*G}_{\ F}\tilde{\Gamma}^I_G \ . \tag{5.3}$$

Γ without a tilde denotes the approximated Coulomb vertex, in contrast to usual convention, simply because the unapproximated vertex will not be used in any subsequent step.

Only the left singular vectors U^F_G associated with the largest singular values will be considered so we contract Eq. (5.2) from the right with $\tilde{\Gamma}^{*G'}_I$

$$\tilde{\Gamma}^I_G\tilde{\Gamma}^{*G'}_I = U^F_G \Sigma^{2F}_{\ F} U^{*G'}_F =: E^{G'}_G \ , \tag{5.4}$$

transforming a singular value problem of a large $N_G \times N_p^2$ matrix into an eigenvalue problem of a comparatively small $N_G \times N_G$ hermitian matrix. The eigenvalues of E are the squares of the singular values of $\tilde{\Gamma}^I_G$, and the left eigenvectors of E associated with the largest eigenvalues are also the left singular vectors of $\tilde{\Gamma}$ we need in order to transform the Coulomb vertex $\tilde{\Gamma}^I_G$ into the optimized auxiliary field Coulomb vertex Γ^I_F

according to Eq. (5.3). Note that this approach becomes numerically problematic for very small singular values since one only has access to their squares. However, all N_F largest singular values needed for an accurate approximation of the Coulomb vertex are sufficiently large.

Inserting the singular value decomposition of the Coulomb vertex with sorted singular values from Eq. (5.2) into the discretized definition of the Coulomb integrals given in Eq. (5.1) yields a singular value decomposition of the Coulomb integrals, also with sorted singular values:

$$V_J^I = W_J^K \Sigma^2{}_K^K W^{*I}{}_K \,, \tag{5.5}$$

where the Coulomb integrals V_{sr}^{pq} are now written in matrix form V_J^I with $I = (q, r)$ and $J = (s, p)$. Thus, using the optimized auxiliary field Coulomb vertex Γ_F^I instead of the full Coulomb vertex $\tilde{\Gamma}_G^I$ best approximates the Coulomb integrals with respect to the Frobenius norm of the difference:

$$V_{sr}^{pq} \approx \Gamma^{*pF}{}_s \Gamma^q{}_{rF} \,. \tag{5.6}$$

It should be stressed that the method outlined above for obtaining the optimized auxiliary field is expected to be less accurate than the more widely used Cholesky decomposition method that employs an upper bound of error to any integral. However, the achieved level of accuracy is sufficient for the present purpose and the level of accuracy can be systematically improved by including a larger number of singular values.

5.2 Low-rank approximation of the Coulomb vertex

The form of the Coulomb vertex in real space on the right hand side in Eq. (4.27) suggests that the optimized Coulomb vertex Γ^q_{rF} can be decomposed in an analogous manner into a product of three tensors of second order, denoted as follows

$$\Gamma^q_{rF} \approx \Lambda^R_F \Pi^{*q}_R \Pi^R_r \,. \tag{5.7}$$

N_R denote the number of *vertex indices* R and will be refered to as the *rank* of the Coulomb vertex for a given quality of the approximation. The matrices Π^R_r and Λ^R_F are labeled *factor orbitals* and *Coulomb factors* of the Coulomb vertex, respectively.

The decomposition is invariant under scaling of the Coulomb factors Λ^R_F with any real scalar $a_R > 0$ while scaling the factor orbitals Π^R_r with a complex scalar c_R with $|c_R| = 1/\sqrt{a_R}$ for each value of R. One can also choose an alternative ansatz to Eq. (5.7) for approximating the Coulomb vertex Γ^q_{rF} which does not involve the conjugation of the

factor orbitals on the outgoing index q. This ansatz reads

$$\Gamma^q_{rF} \approx \Lambda^R_F \Pi^R_q \Pi^R_r \,. \tag{5.8}$$

The above decomposition is invariant under scaling of the Coulomb factors Λ^R_F with any complex scalar $c_R \neq 0$ while scaling the factor orbitals Π^R_r with $\pm 1/\sqrt{c_R}$ for each value of R. This is in contrast to the symmetries of the ansatz according to Eq. (5.7). In the Alternating Least Square (ALS) approximation scheme, which will be employed for fitting the factor orbitals Π and the Coulomb factors Λ, it is preferable to have the symmetries of Eq. (5.8) since fixing one of the two factors removes all continuous symmetries from the other. This accelerates convergence and allows a smaller rank N_R in practice. It should be stressed that the ansatz of Eq. (5.8) is used when real orbitals are employed (Γ-point approximation), however, for a shifted Γ-point calculation where complex orbitals are needed the more widely applicable ansatz of Eq. (5.7) is used.

5.2.1 Canonical polyadic decomposition algorithms

A factorization of a tensor according to the ansatz of Eq. (5.7) or (5.8) is referred to as canonical polyadic decomposition [47] (CPD). For a given rank N_R, the factor orbitals Π^R_r and the Coulomb factors Λ^R_F can be fit by minimizing the square of the Frobenius norm of the difference

$$(\Lambda, \Pi) = \underset{\Lambda,\,\Pi}{\operatorname{argmin}} \left\| \Lambda^R_F \Pi^{*q}_R \Pi^R_r - \Gamma^q_{rF} \right\|^2 . \tag{5.9}$$

The above optimization problem is high dimensional and nonquadratic. Conjugate gradient algorithms or other local algorithms may require thousands of steps until sufficiently converged. Global optimization algorithms try to tackle the problem by keeping a subset of the variables fixed and optimizing only the remaining variables. In the case of the alternating least squares [48] (ALS) algorithm the optimization is done in turn over each matrix, while in the case of the cyclic coordinate descent [49] algorithm the optimization is done in turn over each value of the index R. The performance of a regularized version of the ALS algorithm will be studied here.

5.2.2 Alternating least squares

In the case of three distinct factors $T_{ijk} \approx A_{iR} B_{jR} C_{kR}$ two of them can be regarded fixed leaving a least squares problem for finding the optimal third factor. Each matrix is

optimized in alternating order leading to the *alternating least squares* (ALS) algorithm

$$A^{(n+1)} := \underset{A}{\operatorname{argmin}} \left\| A_{iR} B^{(n)}_{jR} C^{(n)}_{kR} - T_{ijk} \right\|^2 , \tag{5.10}$$

$$B^{(n+1)} := \underset{B}{\operatorname{argmin}} \left\| A^{(n+1)}_{iR} B_{jR} C^{(n)}_{kR} - T_{ijk} \right\|^2 , \tag{5.11}$$

$$C^{(n+1)} := \underset{C}{\operatorname{argmin}} \left\| A^{(n+1)}_{iR} B^{(n+1)}_{jR} C_{kR} - T_{ijk} \right\|^2 , \tag{5.12}$$

which has to be solved iteratively until it is sufficiently converged, starting with random matrices $A^{(0)}, B^{(0)}$ and $C^{(0)}$.

Each least squares problem has a unique solution, which can be written explicitly. For Eq. (5.10) it is for instance given by

$$A^{(n+1)}_{iR} = T_{ijk} B^{*jS} C^{*kS} G^{+}_{SR} , \tag{5.13}$$

omitting the iteration specification on B and C for brevity. G^+ denotes the Moore–Penrose pseudoinverse [50, 51] of the Gramian matrix G. For Eq. (5.10) the Gramian matrix is given by

$$G_{RS} = B^{*jS} C^{*kS} B_{jR} C_{kR} . \tag{5.14}$$

The expressions for the other matrices can be written in an analogous manner. When applying the ALS algorithm to decompose the Coulomb vertex the computationally most demanding steps are the calculation of the pseudoinverse G^+ scaling as $\mathcal{O}(N_R^3)$, as well as the contraction of T_{ijk} with either factor B^{*jS} or C^{*kS} in Eq. (5.13), depending on which is larger, scaling as $\mathcal{O}(N_p^2 N_F N_R)$.

It is noted that the ALS algorithm and the employed CPD of the Coulomb integrals has already been studied in Ref. [52] under the guise of the tensor hypercontraction (THC) method. To overcome the slow convergence of the ALS algorithm, the authors of the THC method have switched in Refs. [53–55] to determining the factor orbitals Π using a real space quadrature grid, which was shown to have physical justification. Having fixed the factor orbitals the Coulomb factors Λ can then be efficiently calculated by a single least squares fit.

5.2.3 Regularized alternating least squares

A modification to the ALS algorithm that can substantially improve the convergence which does not require the choice of a real space quadrature grid is employed. Although the ALS algorithm guarantees an improvement of the fit quality in each iteration the convergence can be very slow, especially when there are multiple local minima for a factor

A in different regions having all similar minimal values. In that case the best choice for A may vary strongly from iteration to iteration since updating the other factors B and C can change the order of the minima. This behavior is referred to as swamping [56] and it takes many iterations before the ALS algorithm converges to one region for each factor that globally minimizes the fit quality. Introducing a penalty on the distance to the previous iteration limits swamping and leads to the regularized ALS [57] (RALS) algorithm:

$$A^{(n+1)} := \underset{A}{\operatorname{argmin}} \left(\left\| A_{iR} B^{(n)}_{jR} C^{(n)}_{kR} - T_{ijk} \right\|^2 + \lambda^{(n)}_A \left\| A_{iR} - A^{(n)}_{iR} \right\|^2 \right), \tag{5.15}$$

$$B^{(n+1)} := \underset{B}{\operatorname{argmin}} \left(\left\| A^{(n+1)}_{iR} B_{jR} C^{(n)}_{kR} - T_{ijk} \right\|^2 + \lambda^{(n)}_B \left\| B_{jR} - B^{(n)}_{jR} \right\|^2 \right), \tag{5.16}$$

$$C^{(n+1)} := \underset{C}{\operatorname{argmin}} \left(\left\| A^{(n+1)}_{iR} B^{(n+1)}_{jR} C_{kR} - T_{ijk} \right\|^2 + \lambda^{(n)}_C \left\| C_{kR} - C^{(n)}_{kR} \right\|^2 \right). \tag{5.17}$$

The solution of each regularized least squares problem can again be given explicitly, here for instance for Eq. (5.15), and again omitting the iteration specification on B and C

$$A^{(n+1)}_{iR} = \left(T_{ijk} B^{*jS} C^{*kS} + \lambda^{(n)}_A A^{(n)}_{iS} \right) G^{+}_{SR} \,. \tag{5.18}$$

In the regularized case the Gramian G depends on the regularization parameter $\lambda^{(n)}_A$

$$G_{RS} = B^{*jS} C^{*kS} B_{jR} C_{kR} + \lambda^{(n)}_A \delta_{RS} \,, \tag{5.19}$$

where δ_{RS} denotes the Kronecker delta.

The regularization parameter $\lambda^{(n)}_A$ for finding $A^{(n+1)}$ in the nth iteration still remains to be determined. Too low values allow swamping to occur while too large values unnecessarily slow down the convergence. For the estimation of an efficient regularization parameter it is assumed that the fit quality $\|AB^{(n)}C^{(n)} - T\|^2$ in the term to minimize in Eq. (5.15) varies little from one iteration to the next. This is also assumed for the

local change of the fit quality with respect to each value in A. This allows to relate the minimized term in the previous step $n-1$ to the minimized term in the step n where the regularization parameter is determined:

$$\lambda^{(n-1)}\|A^{(n)} - A^{(n-1)}\|^2 \approx \lambda^{(n)}\|A^{(n+1)} - A^{(n)}\|^2. \tag{5.20}$$

If $A^{(n)}$ and $A^{(n+1)}$ have similar norm one can also relate their relative step sizes $s_A^{(n)}$ and $s_A^{(n+1)}$, by $\lambda^{(n-1)}{s_A^2}^{(n)} \approx \lambda^{(n)}{s_A^2}^{(n+1)}$, where the relative step size in the nth iteration is given by

$$s_A^{(n)} := \|A^{(n)} - A^{(n-1)}\|/\|A^{(n)}\|. \tag{5.21}$$

The relative iteration step size $s_A^{(n+1)}$ of the next iteration should be approximately as large as a chosen maximum value s_0, which will be refered to as *swamping threshold*. From that the estimated regularization parameter for the nth iteration is defined

$$\hat{\lambda}_A^{(n)} := \lambda_A^{(n-1)}{s_A^2}^{(n)}/s_0^2. \tag{5.22}$$

Directly using the above estimate results in a regularization which we find alternately too strong and too weak. To ameliorate this we introduce a mixing of the estimated regularization parameter $\hat{\lambda}_A^{(n)}$ for the nth iteration, as above, with the regularization parameter $\lambda_A^{(n-1)}$ of the previous iteration to obtain the regularization parameter $\lambda_A^{(n)}$ employed for the nth iteration in the RALS:

$$\lambda_A^{(0)} := 1 \tag{5.23}$$

$$\lambda_A^{(n)} := \alpha\hat{\lambda}_A^{(n)} + (1-\alpha)\lambda_A^{(n-1)}. \tag{5.24}$$

Regarding the choice of the swamping threshold s_0 and the mixing factor α it is found that $s_0 = 1.0$ and $\alpha = 0.8$ offers a good compromise allowing quick convergence while still preventing swamping for the systems studied so far.

5.2.4 Quadratically occurring factors

In the case of the Coulomb vertex the factor orbitals Π_r^R occur quadratically. In order to find the next estimate $\Pi^{(n+1)}$ in the alternating least squares algorithm an iterative algorithm similar to the Babylonian square root algorithm is used. Each subiteration is

given by

$$\begin{aligned}\Pi^{(n+1,m+1)} := (1-\beta)\,\Pi^{(n+1,m)} \\ +\beta \operatorname*{argmin}_{\Pi}\Bigg(\left\| \Lambda_F^{R\,(n+1)} \Pi^{*q}_{R}{}^{(n+1,m)} \Pi_r^R - \Gamma^q_{rF} \right\|^2 \\ + \lambda_\Pi^{(n+1,m)} \left\| \Pi_r^R - \Pi_r^{R\,(n+1,m)} \right\|^2 \Bigg)\end{aligned} \tag{5.25}$$

with $\Pi^{(n+1,0)} := \Pi^{(n)}$ and the mixing factor $0 < \beta < 1$. Note that Π^* is a fixed parameter rather than a fitted one and that the regularization parameter $\lambda_\Pi^{(n+1,m)}$ needs to be determined for the mth subiteration similar to Eq. (5.24), however with $\lambda_\Pi^{(n+1,0)} = \lambda_\Pi^{(n)}$. The above iteration converges towards a solution of the quadratic problem. $\Pi^{(n+1,M)}$ and $\lambda_\Pi^{(n+1,M)}$ are used for the next estimate of $\Pi^{(n+1)}$ and $\lambda_\Pi^{(n+1)}$ in the RALS algorithm, respectively. The number of subiterations M needs to be sufficiently large, such that $\Pi^{(n+1)}$ is at least an improved solution of the entire fit problem compared to $\Pi^{(n)}$. A large number M of subiterations gives an estimate $\Pi^{(n+1)}$ that is close to the optimal choice of Π for a given $\Lambda^{(n+1)}$. However, the cost of each subiteration is similar to the cost of the fit of Λ in the RALS algorithm and a good choice for minimizing the overall computational cost is $\beta = 0.8$ and $M \geq 2$, but only as large such that the solution is an improvement. It should be pointed out that there are alternative methods for solving the quadratically occurring factors [58].

5.3 Implementation of coupled-cluster equations

The algorithms described so far yield an approximate factorization of the Coulomb integrals of the form

$$V^{pq}_{sr} \approx \Pi^{*p}_{R} \Pi^{*q}_{S} \Lambda^{*F}_{R} \Lambda^{S}_{F} \Pi^{S}_{r} \Pi^{R}_{s}, \tag{5.26}$$

where the factors Π and Λ are $N_p \times N_R$ and $N_F \times N_R$ matrices, respectively. It is found that the rank of the decomposition N_R is about an order of magnitude lower than the number of real space grid points of the original factors of the Coulomb integrals, being the orbitals $\psi_q(\mathbf{x})$.

5.3.1 Reduced scaling coupled cluster theory

This section outlines how the obtained factorization can be used to reduce the computational cost of coupled cluster theory. We closely follow the work of Parrish *et al.* in Ref. [59].

The most demanding step in the canonical CCD method using a plane-wave basis set is the calculation of the particle/particle ladder contribution $T_{ij}^{cd}V_{cd}^{ab}$ in the amplitude equation, scaling as $\mathcal{O}(N_\mathrm{o}^2N_\mathrm{v}^4)$ in time. Here, the factorized form of the Coulomb integrals V_{cd}^{ab} can be exploited to break down the simultaneous contraction over the indices c and d into a sequence of contractions involving only at most one index, as follows

$$T_{ij}^{cd}V_{cd}^{ab} \approx T_{ij}^{cd}\Pi_R^a\Pi^{*R}_{\ c}\Lambda^{*F}_{\ R}\Lambda_F^S\Pi^{*b}_{\ S}\Pi_d^S \tag{5.27}$$

The most expensive term in this sequence of contractions leads to a scaling of $\mathcal{O}(N_\mathrm{o}^2N_\mathrm{v}^2N_R)$ in time, without exceeding the memory complexity of the coupled cluster amplitudes. As will be demonstrated later, it is found that N_R is proportional to the system size N, resulting in an $\mathcal{O}(N^5)$ scaling behavior in time of the particle/particle ladder contribution. Likewise, the most expensive term in CCSD amplitude equations includes the singles contribution to the ladder diagram ($T_{ij}^{cd}T_k^aV_{cd}^{kb}$, $T_{ij}^{cd}T_l^bV_{cd}^{al}$, $T_{ij}^{cd}T_k^aT_l^bV_{cd}^{kl}$). Similarly, these terms can be evaluated via the factor orbitals and the Coulomb factors in an $\mathcal{O}(N^5)$ scaling in time

$$\begin{aligned}&(V_{cd}^{ab} - V_{cd}^{ak}T_k^b - V_{cd}^{kb}T_k^a + V_{cd}^{kl}T_k^aT_l^b)(T_{ij}^{cd} + T_i^cT_j^d) \approx \\ &(T_{ij}^{cd} + T_i^cT_j^d)(\Pi_R^a - \Pi_R^kT_k^a)\Pi^{*R}_{\ c}\Lambda^{*F}_{\ R}\Lambda_F^S(\Pi^{*b}_{\ S} - \Pi^{*k}_{\ S}T_k^b)\Pi_d^S\ .\end{aligned} \tag{5.28}$$

The closed CCSD amplitude equations, given in Eqs.(3.66) (3.67) (3.68) have been implemented, with the use of the Coulomb vertex Γ_{rF}^q, the Coulomb integrals $V_{rs}^{pq} = \Gamma^{*pF}_{\ \ r}\Gamma_{sF}^q$, as well as the factorization of the Coulomb vertex $\Gamma_{rF}^q \approx \Lambda_F^R\Pi^{*q}_{\ R}\Pi_r^R$. The workflow is schematically depicted in Fig. 5.1 The Coulomb vertex $\tilde{\Gamma}_{rG}^q$ is calculated using the VASP code within the PAW method, employing canonical HF orbitals, and afterwards is written on the disk. The memory requirement for the Coulomb vertex is $N_\mathrm{p}^2 \times N_G$, where $N_\mathrm{p} = N_\mathrm{v} + N_\mathrm{o}$ denotes the total number of orbitals and N_G the number of plane-wave vectors. Subsequently the Coulomb vertex is read using the CC4S code. The latter is written in C++ and utilizes the Cyclops Tensor Framework (CTF) [60]. CTF is a distributed-memory numerical library that automatically manages tensor blocking and redistribution to perform contractions via matrix multiplication on a properly ordered and structured tensor. CC4S implements a range of coupled-cluster and related methods such as CCSD, and CCSD(T) by writing the equations on top of a C++ templated domain-specific language. The closed shell CCSD equations are given in the Appendix C, and the (T) correction has been implemented in a similar manner.

Kats and Manby [61] proposed an approximation to CCSD theory that neglects exchange processes between different clusters which is formally still exact for two electron systems. The resultant theories have been called distinguishable cluster theories because

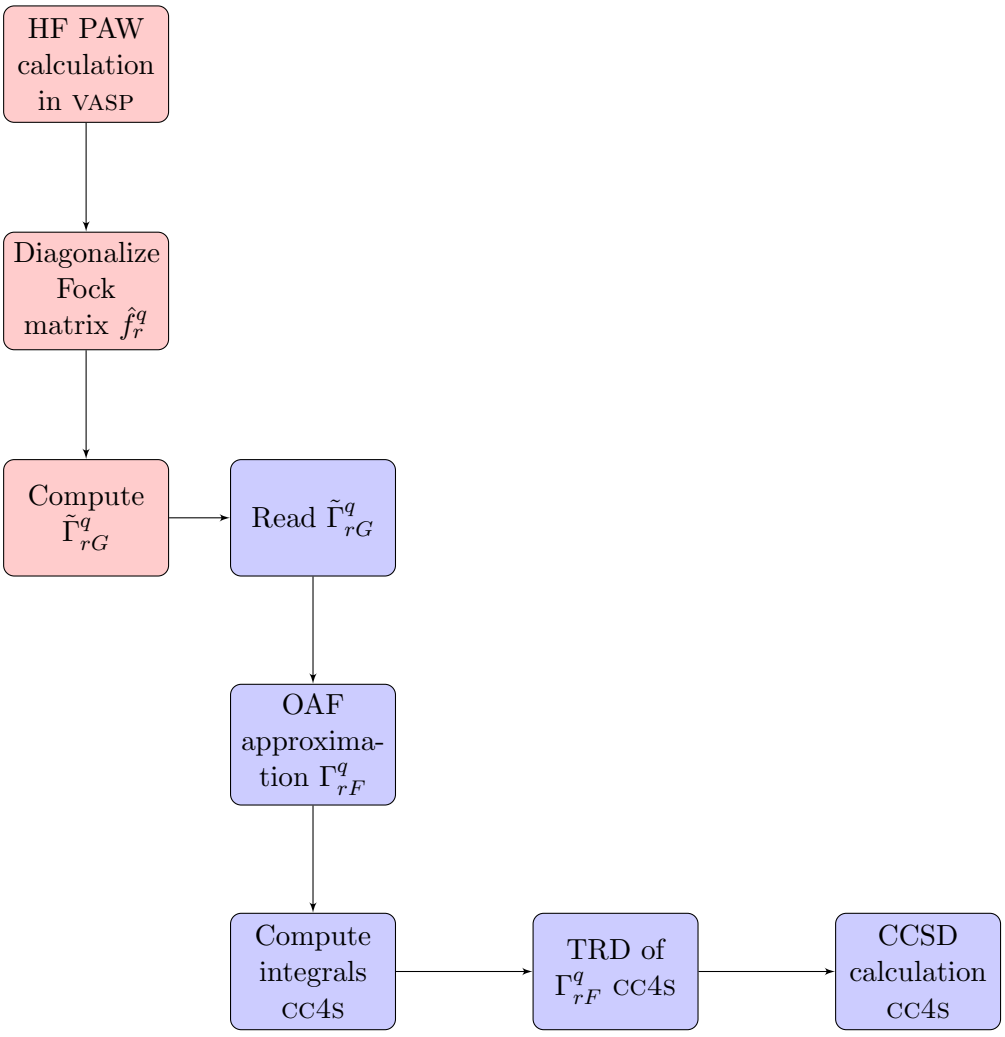

FIGURE 5.1: Schematic illustration of the workflow of a CCSD calculation using the VASP (red squares) and CC4S (blue squares) codes.

they violate the indistinguishability of electrons in a many-electron system. However, it has been shown that distinguishable cluster approximations such as distinguishable cluster singles and doubles (DCSD) correctly dissociate a number of diatomic molecules and yield very accurate equilibrium geometries and interaction energies for many molecular systems, outperforming the accuracy of CCSD theory at the same computational cost [62–64]. Motivated by these findings the distinguishable approximation to CCSD has also been implemented.

5.3.2 Molecular adsorption of water monomer on *h*-BN

In order to demonstrate the applicability of these newly developed methodologies the interaction energy between a water molecule and a 4×4 *h*-BN monolayer is calculated. Periodic CCD theory is employed to examine to what extent the TRD (Tensor Rank

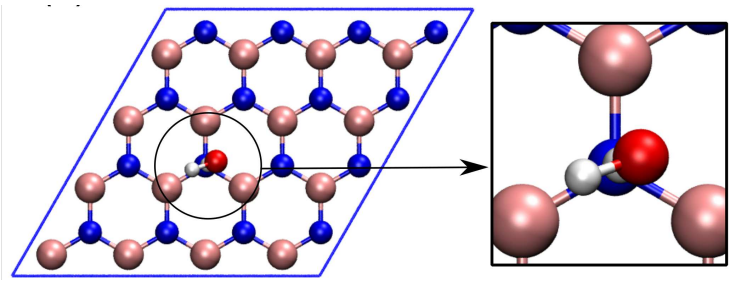

FIGURE 5.2: Computational cell for water adsorbed on a 4×4 h-BN sheet. White spheres are hydrogen, red spheres are oxygen, pink spheres are boron, and blue spheres are nitrogen. Picture is taken from Ref. [65]

Decomposition) and the optimized auxiliary field approximations are accurate and efficient. The structures for the adsorption have been obtained by Al-Hamdani *et al.* [65], whereby the molecule is oriented on top of an N site and the geometry has been optimized using the optB86b-vdW functional. The water–N distance was set to 3.2 Å. The h-BN monolayer is modeled by 32 atoms in the periodic cell and the distance between two BN sheets was set to 16 Å. The corresponding structure is shown in Fig. 5.2 After checking convergence, a 500 eV kinetic energy cutoff was employed for the one particle orbitals along with Γ-point sampling of the Brillouin zone. The B $2s^2 2p^1$, N $2s^2 2p^3$, O $2s^2 2p^4$, and H $1s^1$ states have been treated as valence states. Occupied HF states were converged within the full plane wave basis. The vast number of virtual orbitals in a plane wave basis is truncated by mapping a virtual orbital manifold, expanded in plane waves, onto atom centered basis functions. Dunning's contracted aug-cc-pVDZ (AVDZ) and aug-cc-pVTZ (AVTZ) [66, 67] pseudized Gaussians were chosen to represent the atom centered functions. By orthogonalizing these virtual states to the occupied space an AVDZ and AVTZ basis set is mimicked via orbitals that are expanded in plane waves. The underlying procedure is detailed in Ref. [68] and Section 6.1 later in the thesis. Counterpoise corrections to the basis set superposition error (BSSE) were included in all correlated calculations. Currently the accuracy of the OAF and the low-rank approximations of the Coulomb vertex $\tilde{\Gamma}^q_{rG}$ is examined. The quality of these atom-centered orbitals based on Gaussian basis functions will be discussed later in the thesis.

The adsorption energy is defined as the difference in energy between the non-interacting fragments and the interacting system

$$E_{\text{ads}} = E_{\text{H}_2\text{O}} + E_{\text{BN}} - E_{\text{H}_2\text{O+BN}}. \tag{5.29}$$

Initially, the convergence of the adsorption energy with respect to the number of momentum grid points N_G, employed to evaluate the Coulomb vertex $\tilde{\Gamma}^q_{rG}$ according to Eq. (4.29), is investigated. The selection of the plane waves vectors $\mathbf{G}$ is determined by

a kinetic energy cutoff E_χ such that

$$\frac{\hbar^2 \mathbf{G}^2}{2m_e} < E_\chi. \tag{5.30}$$

For this purpose a pseudized AVDZ basis set represents the virtual orbitals. The current system consists of $N_\mathrm{o} = 68$ and $N_\mathrm{v} = 780$ occupied and virtual orbitals respectively. Kinetic energy cutoff values from 100 to 300 eV were employed for the calculation of the adsorption energy. The results are shown in the inset of Fig. 5.3. The adsorption energy behaves as $CE_\chi^{-3/2}$ [38, 69] up to 200 eV, however, at higher cutoffs one observes a plateau in the curve as a result of the truncation of the virtual orbital space via the pseudized Gaussian basis functions. It can be concluded that a cutoff energy of 200 eV is sufficient to converge the adsorption energy to within 2–3 meV. The accuracy of the optimized auxiliary field technique to approximate the Coulomb vertex $\tilde{\Gamma}^q_{rG}$ for the current system is then investigated at the level of CCD theory. First the optimized Coulomb vertex $\Gamma^q_{rF} = U^{*G}_F \tilde{\Gamma}^q_{rG}$ is obtained, where U^F_G consists of the left singular values of $\tilde{\Gamma}^q_{rG}$ associated with the N_F largest singular values, according to Eq. (5.2). The optimized Coulomb vertex is expected to be efficient since most of the space in the simulation cell is vacant, and the plane-wave auxiliary basis contains redundant information. Different number of field variables N_F were employed to approximate the plane wave vectors N_G for the various cutoff energies. The behavior of the adsorption energy with respect to the number of field variables is shown in Fig. 5.3. The rapid convergence of the energy with increasing number of field variables owes to the locality of the molecular orbitals in the supercell. The adsorption energy obtained with a cutoff of 200 eV can be calculated within 0.5 meV accuracy using $N_F = 1450$ field variables to approximate $N_G = 4504$ plane wave vectors.

Since it is concluded that the adsorption energy can be computed within approximately 3 meV using a cutoff energy of 200 eV for the auxiliary plane-wave basis and $N_F = 1450$ field variables to construct the optimized Coulomb vertex, these settings are chosen to assess the accuracy of the low rank factorization of the Coulomb integrals. Different number of vertex indices R are used to compute the factor orbitals and Coulomb factors of the Coulomb vertex, following Eq. (5.8). The particle/particle ladder contribution $T^{cd}_{ij} V^{ab}_{cd}$ in the amplitude equation of CCD is approximated via the factor orbitals and the Coulomb factors as shown in Eq. (5.7). The adsorption energy versus the number of the vertex indices N_R is shown in Fig. 5.4. The energy does not converge monotonically as in the case of the optimized auxiliary field approximation. This is due to the nonlinear nature of the canonical polyadic decomposition of the Coulomb vertex and the random initial choice for its factors. Nevertheless a converged behavior with increasing N_R is observed. Furthermore, a value of $N_R = 4350 = 3N_F$ is sufficient

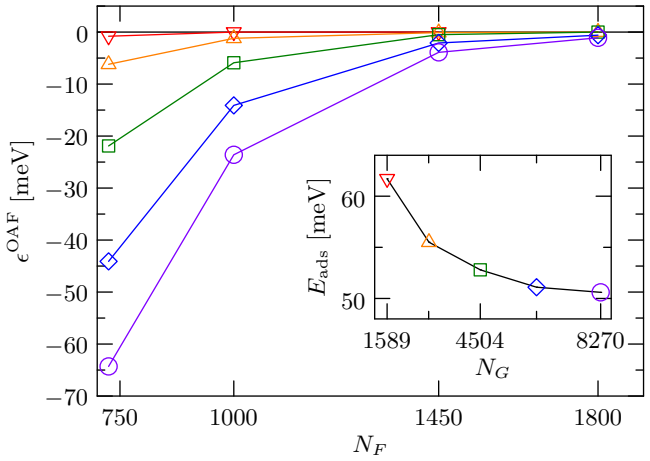

FIGURE 5.3: Optimized auxiliary field (OAF) approximation error $\epsilon^{\mathrm{OAF}}(N_F) = E_{\mathrm{ads}}(N_F) - E_{\mathrm{ads}}(N_G)$ of the CCD adsorption energy as a function of the number of field variables N_F used to approximate the Coulomb vertex. The number of G vectors N_G of the unapproximated Coulomb vertex $\tilde{\Gamma}^q_{rG}$ is indicated by the shape of the markers. The inset shows which marker corresponds to which N_G and plots the convergence of the adsorption energy with respect to N_G, corresponding to kinetic energy cutoff values of 100, 150, 200, 250, and 300 eV, respectively.

to yield an adsorption energy within 1 meV accuracy. This suggests that the TRD of the Coulomb vertex is a controllable approximation that can yield increasingly accurate results with increasing decomposition rank N_R. In order to further validate the accuracy of the TRD method the convergence of the absolute energy of the interacting system with respect to the decomposition rank N_R is shown in the inset of Fig. 5.4. An exponential convergence of the total energy is evident. An accuracy better than 0.1% is achieved already with $N_R = 2N_F$. Nevertheless, the corresponding accuracy in the adsorption energy is a result of an error cancellation of one to two orders of magnitude.

Having assessed the accuracy of the TRD the adsorption energy of the water molecule on h-BN is now calculated using the AVTZ pseudized Gaussian basis set. The evaluation involves the decomposition of a Coulomb vertex with $N_{\mathrm{o}} = 68$, $N_{\mathrm{v}} = 1564$, $N_F = 0.33N_G = 1450$, and $N_R = 3N_F = 4350$. The computational cost to obtain the decomposed matrices is roughly 3000 CPU hours with 256 iterations. The CPU hours required for the CCD calculations obtained with and without the TRD technique are summarized in Table 5.1. The time for the evaluation of the particle/particle ladder term per iteration is as much as 43 times faster using a decomposition with $N_R = 2N_F$ and 22 times faster with $N_R = 3N_F$. This constitutes a significant gain in the computational effort of coupled cluster methods with only slight compromise in accuracy.

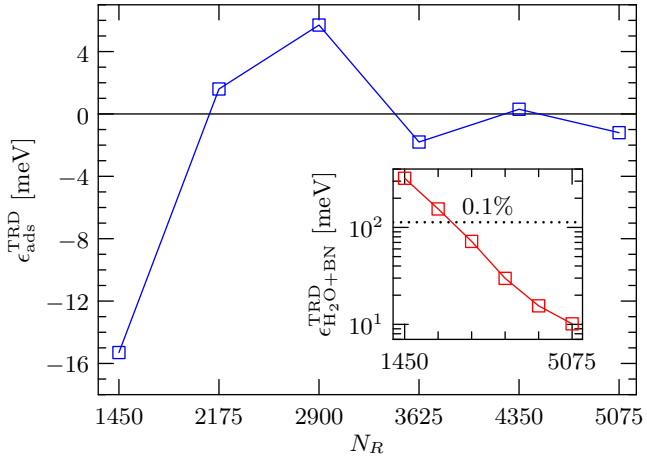

FIGURE 5.4: Low rank approximation error $\epsilon^{\mathrm{TRD}}_{\mathrm{ads}}(N_R) = E_{\mathrm{ads}}(N_F, N_R) - E_{\mathrm{ads}}(N_F)$ of the CCD adsorption energy as a function of the rank N_R using the OAF approximated Coulomb vertex with $N_F = 1450$ field variables. The inset shows the respective approximation error for surface+molecule fragment $\epsilon^{\mathrm{TRD}}_{\mathrm{H_2O+BN}} = E_{\mathrm{H_2O+BN}}(N_F, N_R) - E_{\mathrm{H_2O+BN}}(N_F)$ only, revealing an error cancellation of one to two orders of magnitude in the adsorption energy.

TABLE 5.1: CPU hours per iteration comparing CCD calculation with and without the factorized Coulomb integrals. In parenthesis we denote the part for evaluating the particle/particle ladder term.

Basis set	$N_R = 2N_F$		$N_R = 3N_F$		no TRD	
AVDZ	39	(13)	49	(24)	100	(75)
AVTZ	259	(28)	258	(55)	1443[a]	(1212)

[a] estimation based on the AVDZ basis set.

Chapter 6

Basis set and thermodynamic limit approximation

In this Chapter an efficient yet accurate truncation of the plane-wave virtual orbital manifold is discussed, based on either atom-centered Gaussian basis sets or MP2 natural orbitals. A tricubic interpolation of the correlation energy structure factor around the $\mathbf{G} \to 0$ limit is then investigated, to capture long-range correlation effects, together with an averaged shifted Γ-point technique that allows a smooth convergence of the correlation energy with respect to the band structure dispersion. The accuracy of these approximations is demonstrated by studying water adsorption on hexagonal Boron Nitride (h-BN) sheet, a typical example of weak molecular physisorption on an insulating two-dimensional surface.

6.1 Atom-centered Gaussians as plane-wave orbitals for correlated methods of periodic systems

All the hitherto correlated methods, such as MP2 and CC, have been discussed in the context of canonical plane-wave HF orbitals. The plane-wave basis is defined by an energy cutoff and the full set of canonical HF orbitals (occupied and virtual) is obtained by diagonalizing the Fock matrix within the given plane-wave basis. Plane-waves represent a convenient choice to expand one-electron orbitals in periodic systems since they are eigenstates of the kinetic energy operator and naturally fulfil the periodicity of the computational cell. However, there are some drawbacks to plane-wave expansions. Since they make no reference to the nature of the atomic environment, they have equal basis coverage throughout the cell. This can lead to a great deal of wasted computational effort when studying surfaces or low-dimensional systems. This is due to the necessity for

large amounts of vacuum in the cells to minimize the effect of spurious periodic images, which results in large, unwieldy plane-wave expansions to converge the total energy.

For correlated methods, the steeper scaling compared to mean-field methods means that the speed of convergence with respect to number of basis functions is even more critical. For instance, our implementation of MP2 scales as $\mathcal{O}(N_\mathrm{o}^2 N_\mathrm{v}^2 N_G)$, whereas CCSD as $\mathcal{O}(N_\mathrm{o}^2 N_\mathrm{v}^4)$, where N_o, N_v, and N_G is the number of occupied orbitals, virtual orbitals, and plane-wave vectors of the Coulomb vertex respectively. Rather than using plane waves directly for the virtual space, it is more common to truncate the prior mean-field virtual manifold on an energetic criteria to improve the convergence to the complete basis set. However, this virtual manifold is not inherently physical, and its somewhat arbitrary truncation therefore does not necessarily provide a good basis to expand the correlated wavefunction. Truncating based on an energetic criteria (now on the mean-field energy rather than kinetic energy as for plane waves) does not necessarily yield fast convergence. Furthermore, consistent truncations of the virtual bandstructure when comparing fundamentally different systems, such as an isolated molecule and a surface, are close to impossible to achieve, and therefore still generally rely on convergence to costly, near-complete basis sets for meaningful comparisons. Attempts to truncate virtual single-particle orbital expansions using other criteria, such as occupation numbers from other levels of theory, have had some success, but can often be expensive to carry out [70, 71]. The use of MP2 natural orbitals is examined in the next section.

An alternative representation to plane wave expansions is local atom-centered functions, such as Gaussian basis sets. While Gaussian basis sets can potentially take many different parameterizations, their widespread use within the field of quantum chemistry has meant that many tabulated basis sets of increasing size and flexibility are readily available [66, 67, 72]. The use of atom-centered Gaussian-type orbitals (GTOs) in periodic electronic structure is not new, with several other codes employing their use [73–81]. Furthermore, mixed plane-wave and Gaussian schemes have also been previously introduced as an attempt to combine their strengths in electronic structure calculations of periodic systems [82].

An implementation of a straightforward approach for the use of a periodic Gaussian basis (or indeed any numerical atom-centered functions) within the PAW framework in the VASP code is presented. An application of several correlated levels of theory to a number of systems, demonstrates that the consistent level of truncation as afforded by the Gaussian basis set expansions leads to a rapidly convergent and extrapolatable virtual space for the calculations. A comparison with all-electron molecular calculations, provides confidence in the applicability of the functions within the PAW framework.

An efficient hybrid approach is explored, whereby the occupied orbitals are first converged within a large primitive plane wave expansion, rendering the occupied space and hence the HF energy essentially complete. A virtual basis is then included for the correlation treatment comprised of the complementary set of orbitals constructed by projecting the occupied orbitals out of the Gaussian basis set. By rediagonalizing the Fock matrix in this newly constructed virtual space, a canonical formulation of correlated methods is possible. This dual approach removes basis set incompleteness of the occupied one-electron orbitals and thus substantially ameliorates the issue of basis-set superposition error, which now only manifests through the subsequent correlation treatment. Additionally, it retains the benefits of the compact, consistent virtual space afforded by the atom-centered Gaussians.

6.1.1 Construction of plane-wave Gaussians

A Gaussian basis set is composed of atom-centered functions that can be decomposed into radial and angular parts such that an angular momentum function (l, m) for a given atom positioned at $\mathbf{R}$ can be given by

$$G_{lm\mathbf{R}}(\mathbf{r}) = R_l\big(\big|\mathbf{r}-\mathbf{R}\big|\big)Y_{lm}(\theta,\phi) \ , \tag{6.1}$$

where $Y_{lm}(\theta,\phi)$ are spherical harmonic functions and $\mathbf{r},\theta,\phi$ represent spherical coordinates. The radial function $R_l\big(\big|\mathbf{r}-\mathbf{R}\big|\big)$ is expanded into Gaussian functions

$$R_l\big(\big|\mathbf{r}-\mathbf{R}\big|\big) = \big|\mathbf{r}-\mathbf{R}\big|^l \sum_p c_p A(l,\alpha_p) e^{-\alpha_p|\mathbf{r}-\mathbf{R}|^2} \ , \tag{6.2}$$

where $A(l,\alpha_p)$ is a normalization constant of the Gaussian primitives and c_p the contraction coefficients for the primitive Gaussian functions with exponent α_p. Such a Linear combination of primitive Gaussian functions is formed to approximate the radial part of the atomic orbitals.

Such a Gaussian basis set is sought to be expanded in plane-waves, seamlessly integrated within the PAW framework. The Fourier components of strongly localized real space orbitals decay very slowly, which results in a slow convergence of the orbitals with respect to the underlying plane-wave energy cutoff. This cutoff energy dictates the size of the plane-wave basis employed in Eq. (4.5). The slow convergence of the orbitals with respect to this cutoff is mainly due to sharp features of the Gaussian-type orbitals (GTOs) resulting from the fitting of the non-analytic cusp behavior at the nuclear coalescence point, which in non-relativistic quantum theory exhibits a derivative discontinuity in the wavefunction. However, the plane-wave basis is augmented within the PAW framework,

which includes a description of the atomic core region of each atom. This augmentation largely resolves these sharply varying parts of the wavefunction.

To this end the radial part of the Gaussian functions defined in Eq. (6.2) are pseudized, which smooths the core region of each function, defined up to a pseudization radius from the nucleus, r_c. This is done in a way consistent with the symmetry and norm of the orbitals, and results in a rapidly convergent set of Fourier components representing pseudized GTOs (PGTOs). The employed pseudization strategy mirrors the work of Kresse *et al.* in the construction of pseudized partial waves for pseudopotentials [83]. The core of the pseudized radial Gaussian basis functions is expanded in three spherical Bessel functions such that

$$\tilde{R}_l(r) = \sum_{i=1}^{3} \alpha_i r j_l(q_i r) \ , \tag{6.3}$$

where q_i is chosen such that the value of the function as well as logarithmic derivatives match at the cutoff radius,

$$\frac{\partial}{\partial r}\big[\log R_l(r)\big]\big|_{r=r_c} = \frac{\partial}{\partial r}\big[\log\big(r j_l(q_i r)\big)\big]\big|_{r=r_c} \ . \tag{6.4}$$

Moreover, norm conservation of the PGTO is required such that

$$\int_0^{r_c} \tilde{R}_l(r)^2 \mathrm{d}r = \int_0^{r_c} R_l(r)^2 \mathrm{d}r \ . \tag{6.5}$$

It is noted that for $r \geq r_c$ the following condition holds $R_l(r) = \tilde{R}_l(r)$. The pseudization radius can be chosen such that it is identical to the cutoff radius used by the projectors $\tilde{p}_i$ in the PAW method. In this manner the core region of the pseudized Gaussians is augmented with additional terms that capture the oscillatory and sharp features of the one-electron wavefunctions in this region. The procedure is schematically depicted in Fig. 6.1 Once the appropriate Fourier components are found, integrals between the orbitals can be obtained in the reciprocal basis using the procedure detailed in Chapter 4.

The one-particle orbitals are constructed pursuing a hybrid approach for the correlated calculations. The HF part of the calculation is performed with a plane-wave basis, where the convergence can be achieved using affordable energy cutoffs, yielding optimal occupied orbitals and eigenenergies. The large expansion of virtual orbitals as plane-waves or virtual canonical orbitals is then avoided by representing the virtual space as an expansion of pseudized Gaussian basis functions, after having projected out the

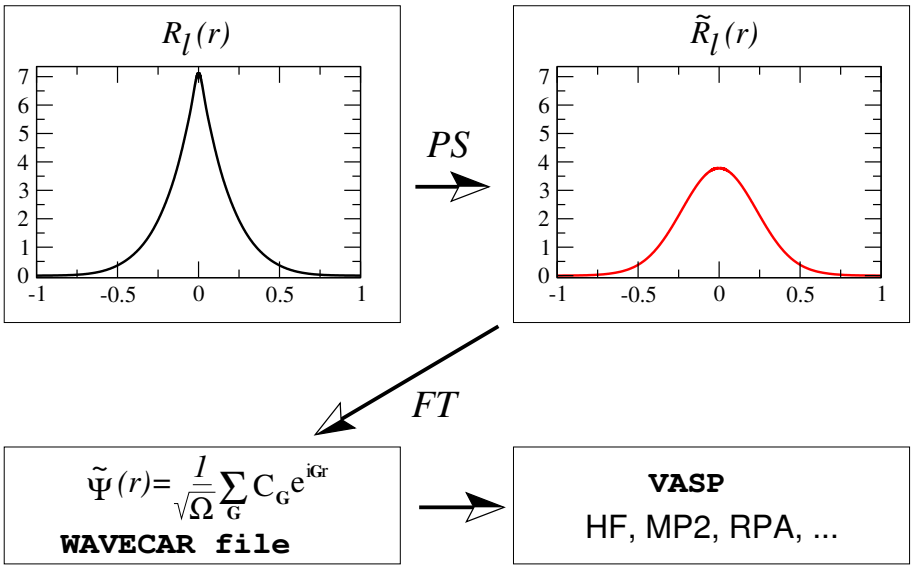

FIGURE 6.1: Schematic illustration of the workflow. A Gaussian basis set is represented on a radial grid (left upper panel). We employ a pseudization strategy (PS) to allow the core to be more efficiently represented by its Fourier coefficients by calculating the corresponding pseudized basis function (right upper panel). In the following step we Fourier transform (FT) the pseudized Gaussian-type orbital (PGTO) to the plane wave basis (left bottom panel). This is then used for the various electronic structure post-HF theories.

component of the (complete) occupied space from the Gaussian basis. This ensures that the full flexibility of the pseudized Gaussian basis is spanned, in addition to the complete occupied space. Since all orbitals are ultimately expressed by their Fourier components, this projection is trivially achieved, and the virtual orbital space $\{|\psi_\alpha\rangle\}$ can be constructed as

$$|\psi_\alpha\rangle = |G_\alpha\rangle - \sum_i |\psi_i\rangle\langle\psi_i|G_\alpha\rangle \ , \tag{6.6}$$

where $|G_\alpha\rangle$ is the Gaussian basis, and $|\psi_i\rangle$ represents the complete space of occupied orbitals expressed in the plane-wave basis (note that the $|\psi_i\rangle$ orbitals which are projected out refer to the AE orbitals rather than the pseudized orbitals to ensure true orthogonality). If the norm of any virtual orbital is below a threshold value after this projection, then it is removed from the calculation, while the rest are orthonormalized and constitute the virtual basis for the calculation. The virtual space is subsequently canonicalized before use in post-mean-field methods, with no further mixing between occupied and virtual states possible. The benefits of this basis construction are significant, with basis set incompleteness and superposition error only remaining in the correlated treatment of the wavefunction, which is readily extrapolatable within the employed correlation-consistent basis sets. A schematic illustration of the workflow employing the PGTOs as virtual orbitals is depicted in Fig. 6.2.

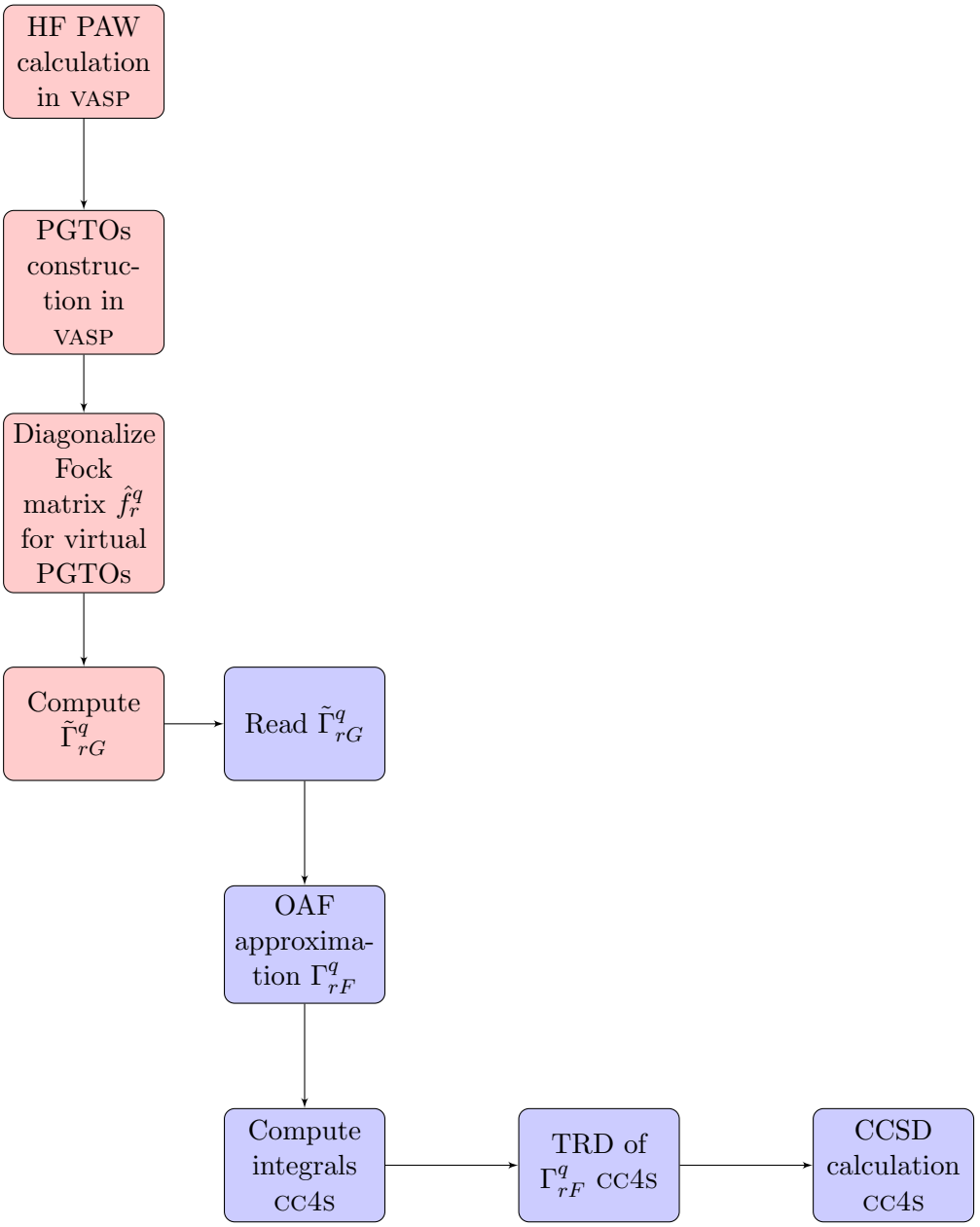

FIGURE 6.2: Schematic illustration of the workflow of a CCSD calculation with plane-wave expanded PGTOs representing the virtual one-electron states using the VASP (red squares) and CC4S (blue squares) codes.

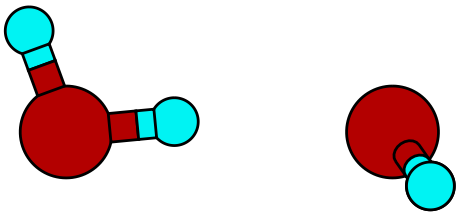

FIGURE 6.3: Water dimer geometry. The picture is taken form Ref. [68], whereas the atomic positions from http://cccbdb.nist.gov/

6.1.2 Water dimer

As an exemplary calculation the binding energy of water dimer is studied. This is an important example because plane-wave basis set calculations are computationally very expensive for atomic and molecular systems for they require a large simulation box with a lot of vacuum to minimize interactions between periodic images, similar to the case of surface studies. As a result of the large box size the number of plane-wave basis functions becomes very large regardless of the actual number of atoms and electrons in the unit cell. In this calculation a $10 \times 10 \times 10$ Å^3 cubic box is employed. The geometry of the water dimer is shown in Fig. 6.3. The cutoff energy was set to 600 eV resulting in a basis set size consisting of more than 30000 plane-waves, leading to a huge number of virtual orbitals. However, the number of Gaussian basis functions is smaller than 200 even for the largest used aug-cc-pVTZ basis set. The complete occupied space of states was first calculated and included within the basis to saturate the HF wavefunction. The PGTO basis was therefore only used to span the complementary virtual space.

Table 6.1 summarizes the obtained binding energies for the water dimer on the level of HF and MP2 theories calculated using the aug-cc-pVDZ (aVDZ) and aug-cc-pVTZ (aVTZ) contracted basis sets. Gas-phase calculation employ the PSI4 code [84], whereas periodic calculations the VASP code alongside the pseudized Gaussian basis to represent the virtual orbitals. The oxygen 1s orbitals of the GTO calculations were frozen to allow for fairer comparison to the valence-only PGTO calculations performed with the PAW method. Since the PGTOs are only used to span the virtual orbitals, the HF contribution to the binding energies is independent of the PGTO basis set size. This also renders the occupied space and HF contribution free of basis set superposition error, as shown by the lack of a counterpoise correction to the values. PGTOs and GTOs yield MP2 binding energies that deviate by more than 20 meV from each other when no allowance is made for basis set superposition error. However, the majority of this difference is due to the incompleteness in the HF contribution to the interaction in the GTO basis.

TABLE 6.1: Binding energy contributions for the water dimer using HF and MP2 theories, comparing results from gas-phase calculations in a contracted aug-cc-pVXZ basis with PSI4 with frozen oxygen 1s core, and results from a periodic system in a $10 \times 10 \times 10$ Å^3 cubic box, with a pseudized basis in VASP. The (CP) denotes that counterpoise corrections have been included for basis set superposition error in this basis. All units are in meV.

	PGTOs			GTOs		
Basis	HF	MP2 corr.	MP2	HF	MP2 corr.	MP2
aVDZ	142	56	197	155	62	217
aVTZ	142	66	208	145	69	215
aVDZ(CP)	142	41	183	151	42	194
aVTZ(CP)	142	53	195	144	53	197

The discrepancy in the MP2 correlation contribution to the interaction energy is only at most 6 meV, despite the contrasting occupied space. This difference decreases as the basis set is increased and the HF contribution of the GTO basis becomes increasingly complete to match the PGTO calculations. Basis set superposition errors are a well-known drawback of atom-centered basis sets and can typically lead to an overestimation of binding energies. This is because more basis coverage is available for each monomer at shorter bond lengths, as it can exploit the basis coverage supplied by the overlap of the functions from the other monomer.

To better understand the origin of the difference between PGTOs and GTOs calculations with counterpoise corrections (CP) for the basis set superposition error (BSSE) [85] are also included in Table 6.1. Both our PGTO and GTO calculations lower the predicted binding energies by about 15 meV and 20 meV in the case of PGTOs and GTOs, respectively, if BSSE is accounted for. This basis set superposition error in the case of the PGTO is purely contained in the correlation part of the MP2 since the occupied space is complete, while for the GTO basis it also includes basis set superposition in the HF contribution. Once the BSSE of purely the correlation part of the MP2 interaction energy is analyzed, results are in closer agreement, however, these will still be affected by the contrasting occupied space in each system. From this example one can conclude that our PGTO basis sets yield a comparably accurate description of electronic correlation effects as the GTO counterparts for molecular systems.

TABLE 6.2: Binding energy contributions for the water dimer using HF and MP2 theories, comparing results from gas-phase calculations in a contracted aug-cc-pVXZ basis with PSI4 with frozen oxygen 1s core, and results from a periodic system in a $10 \times 10 \times 10$ Å^3 cubic box, with a pseudized basis in VASP. The (CP) denotes that counterpoise corrections have been included for basis set superposition error in this basis. All units are in meV.

Basis	No. of virtual orbitals	HF	MP2 corr.	MP2
aVDZ(CP)	845	42	−141	−99
aVTZ(CP)	1632	42	−152	−110
PW (100eV)	22213	42	−176	−134
PW (150eV)	22213	42	−165	−123
PW (200eV)	22213	42	−162	−120
PW (extr.)	22213	42	−153	−111

6.1.3 Water adsorption on *h*-BN

The prototypical surface adsorption problem, water monomer on a 4×4 *h*-BN sheet, is then analyzed in order to demonstrate the accurate truncation of the virtual orbital space, using the PGTOs. Dunning's contracted aug-cc-pVDZ (AVDZ) and aug-cc-pVTZ (AVTZ) [66, 67] pseudized Gaussians were chosen to represent the atom centered functions. By orthogonalizing these virtual states to the occupied space we retain a canonical implementation of the correlated wavefunction-based methods as schematically depicted in Fig. 6.2. We compare this truncation to the full canonical HF plane-wave orbitals. We note that no OAF or TRD approximations are used in this study.

Table 6.2 summarizes MP2 adsorption energies using different virtual orbital schemes. It is evident that a truncation based on an AVTZ basis set yields an adsoprtion energy of −110 meV, very close to the complete basis set (CBS) limit result using the full plane-wave orbitals, that is −111 meV. It is noted that the AVTZ basis set consists of 1632 virtual orbitals compared to 22213 of the canonical HF orbitals using the full plane-wave basis, thus significantly reducing the computational cost.

6.2 MP2 natural orbitals

In the previous Section a truncation of the vast number of plane-wave virtual orbitals was introduced. A compact representation of the virtual orbital space is found by mapping a set of pseudized atom-centered Gaussian functions onto a plane-wave representation.

This virtual orbital manifold can produce accurate results with significantly fewer number of virtual states. In this Section a brief introduction of MP2 natural orbitals is given [70, 86, 87].

Natural orbitals (NOs) were introduced by Löwdin as eigenstates of a state-specific one-particle density matrix [86]. MP2 NOs are calculated by the diagonalization of the MP2 one-particle reduced density matrix [70, 88]

$$D_{ab} = \sum_{ijc} \frac{2\langle cb|ij\rangle\langle ij|ca\rangle - \langle cb|ij\rangle\langle ij|ca\rangle}{\Delta_{ij}^{cb}\Delta_{ij}^{ca}} \ , \tag{6.7}$$

where

$$\Delta_{ij}^{cb} = \varepsilon_i + \varepsilon_j - \varepsilon_c - \varepsilon_b \ . \tag{6.8}$$

The indices i and j refer to the band index of occupied spatial orbitals, whereas indices a, b, and c to the band index of virtual spatial orbitals. ε_n refers to the HF orbital eigenenergies. Eigenstates and eigenenergies of the one-particle density matrix are the MP2 NOs. Diagonalization of the density matrix D_{ab} mixes only the virtual orbitals. However, in contrast to canonical virtual HF orbitals, MP2 NOs do not diagonalize the Fock operator. A recanonicalization of the Fock operator in the basis of the virtual NOs allows for a canonical implementation of correlated methods. The diagonalization of the MP2 one-particle reduced density matrix requires the full plane-wave HF orbitals to be included. However, one can diagonalize the MP2 density matrix using the PGTOs as virtual states. This results in a reduction of the virtual states of about half. The procedure is depicted in Fig. 6.4.

6.3 Finite size corrections for periodic CC

Many-body methods such as coupled cluster theory can describe both long- and short-ranged electronic correlation effects with high accuracy. However, the scaling of the computational complexity of these theories with respect to system size is of a high-order polynomial form. Therefore, it is difficult to treat long-range correlation effects in a computationally efficient manner using these theories. In particular, the thermodynamic limit of an extended system is approached as $N \to \infty$, where N is the number of particles in the simulation cell. Finite-size errors are defined as the difference between the thermodynamic limit and the finite simulation cell results. For electronic correlation energies obtained using many-electron perturbation theories, these errors typically decay as $1/N$ for a 3–dimensional and $1/N^2$ for a 2–dimensional system as a consequence of long-range interatomic van der Waals forces.

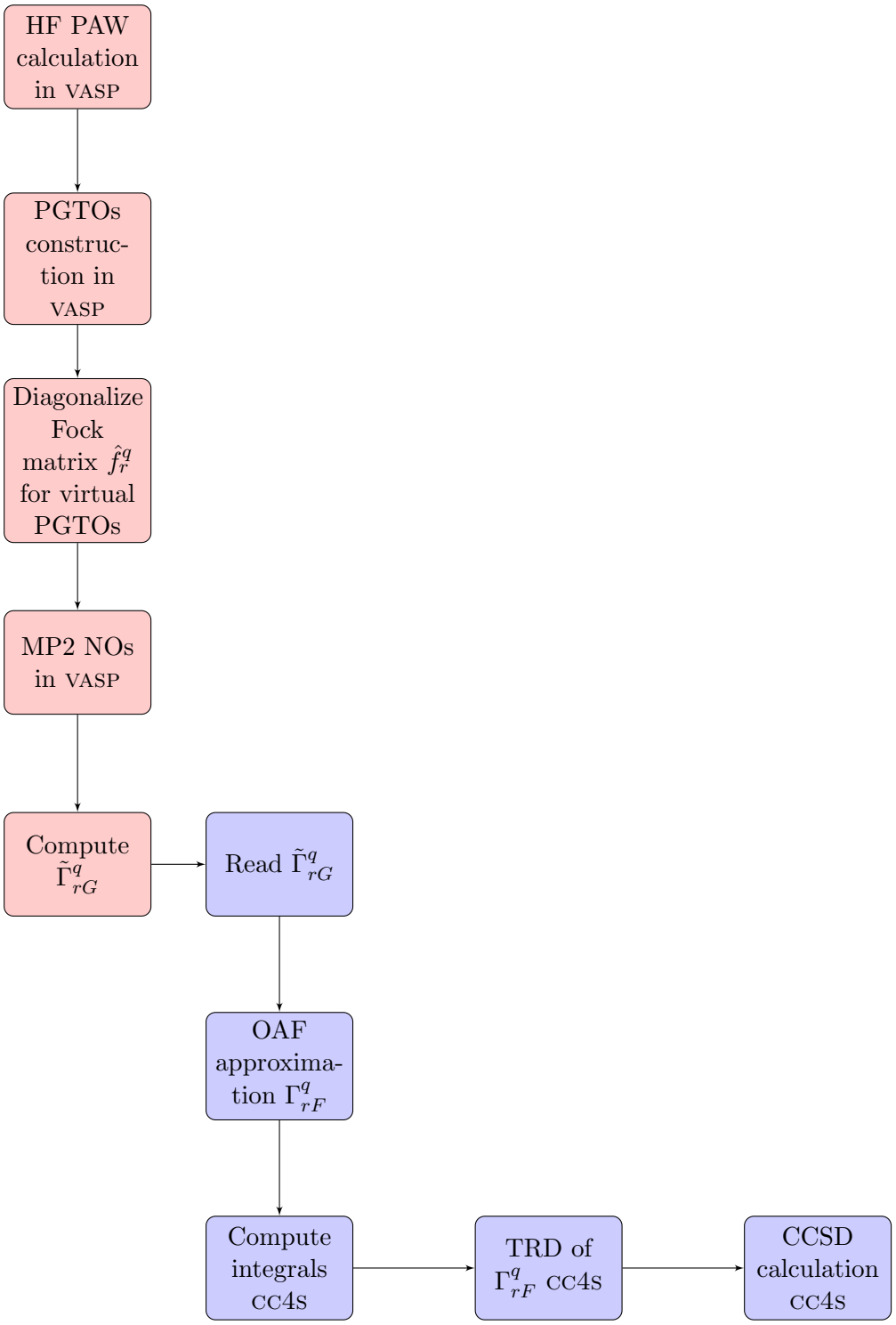

FIGURE 6.4: Schematic illustration of the workflow of a CCSD calculation with plane-wave expanded PGTOs representing the virtual one-electron states using the VASP (red squares) and CC4S (blue squares) codes.

The electronic correlation energy can be calculated in a plane-wave basis set using the expression from Eq. (3.61) and the two-electron integral approximation of Eq. (4.29) as

$$E_c = \langle 0|\big(\hat{\mathcal{H}} - E\big)|\Psi\rangle = \sum_{ij}\sum_{ab} T_{ij}^{ab}\big(2V_{ij}^{ab} - V_{ji}^{ab}\big) = \sum_{\mathbf{G}}{}' v(\mathbf{G})S(\mathbf{G}) \ . \tag{6.9}$$

Within the Γ-point approximation, $\mathbf{G}$ corresponds to a reciprocal lattice vector. Note that $v(\mathbf{G})$ is the Coulomb kernel in reciprocal space that diverges at $\mathbf{G} \to 0$, making it numerically necessary to disregard this contribution to the sum, as indicated by the apostrophe. Thus, $S(\mathbf{G})$ is the partial functional derivative of the correlation energy with respect to $v(\mathbf{G})$. In the thermodynamic limit, the $\sum_{\mathbf{G}}$ of Eq. (6.9) is replaced by $\int_{\mathbf{G}}$. Therefore, finite-size errors in the correlation energy of periodic systems originate from two sources [89]:

1. quadrature errors in the summation over $\mathbf{G}$.
2. the slow convergence of $S(\mathbf{G})$ with respect to the employed supercell size or k-point mesh.

Contributions to finite-size errors originating from the quadrature in the summation over $\mathbf{G}$ can be partitioned into the $\mathbf{G} = \mathbf{0}$ volume element contribution and the remaining terms. We note that as a result of the Coulomb divergence, the integrable contribution of $S(\mathbf{0})v(\mathbf{0})$ to the correlation energy is usually neglected in computer implementations of Eq. (6.9) [90, 91]. However, this is the dominant contribution to the finite size error of the correlation energy of insulators. A Taylor expansion of $S(\mathbf{G})$ around $\mathbf{G} = \mathbf{0}$ shows that $S(\mathbf{G})$ exhibits a quadratic behavior close to zero, explaining the $1/N$ decay of the finite size error for three dimensional insulators [90]. An estimate of $S(\mathbf{0})v(\mathbf{0})$ can be obtained by spherically averaging $S(\mathbf{G})$ and interpolating around $\mathbf{G} = \mathbf{0}$. Subsequently, the interpolated function is multiplied with the analytic Coulomb kernel and integrated over a sphere around $\mathbf{G} = \mathbf{0}$, yielding an estimate of $S(\mathbf{0})v(\mathbf{0})$ [90]. However, this approach is not well defined for anisotropic systems, such as surfaces, because it requires a spherical cutoff parameter. This drawback can be ameliorated by performing a tricubic interpolation of $S(\mathbf{G})$ without spherical averaging. Once obtained the interpolation of $S(\mathbf{G})$ and the analytic expression for the Coulomb kernel allows for integrating over $\mathbf{G}$ on a very fine grid, simulating the thermodynamic limit integration. This approach accounts for the $S(\mathbf{0})v(\mathbf{0})$ contribution to the correlation energy and reduces quadrature errors originating from too coarse a Brillouin zone sampling. Coupled cluster correlation energies obtained using this interpolation strategy will be referred to as CC-FS.

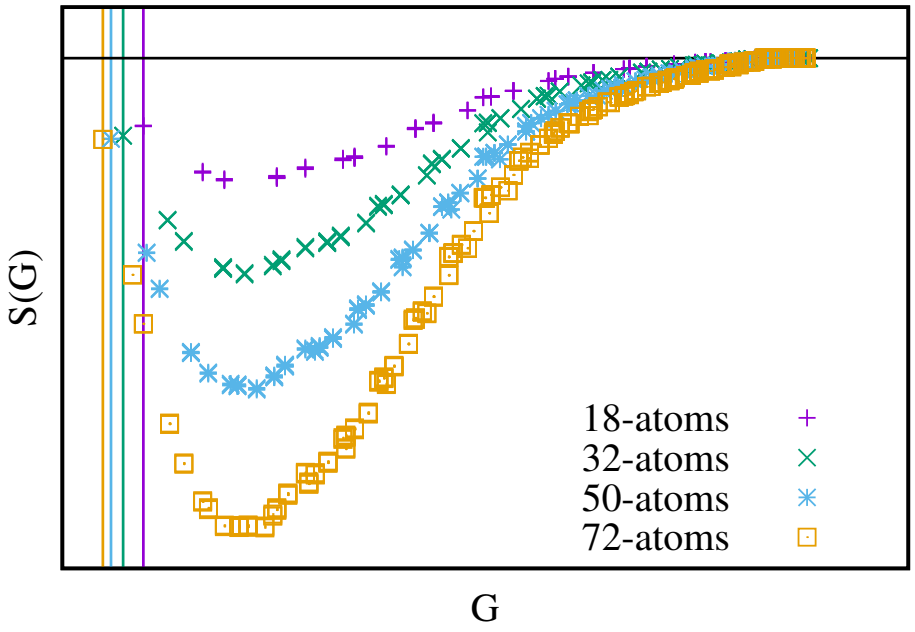

FIGURE 6.5: Partial derivative of the correlation energy with respect to the Coulomb kernel for water on h-BN, for different substrate sizes. On x-axis G denotes the absolute value of the reciprocal lattice vector $\mathbf{G}$.

The partial functional derivative of the correlation energy with respect to the Coulomb kernel $v(\mathbf{G}) = \frac{4\pi}{\mathbf{G}^2}$ can be expressed as

$$S(\mathbf{G}) = \sum_{ij} \sum_{ab} T_{ij}^{ab} \left[2C_i^a(\mathbf{G}) C_b^{j*}(\mathbf{G}) - C_i^b(\mathbf{G}) C_a^{j*}(\mathbf{G}) \right] , \tag{6.10}$$

where $C_i^a(\mathbf{G})$ is the Fourier transformed overlap density, defined in Eq. (4.26), and T_{ij}^{ab} are the amplitudes obtained either from CCSD or MP2 theory. A tricubic interpolation technique is employed to reduce quadrature errors in $\sum_{\mathbf{G}} v(\mathbf{G}) S(\mathbf{G})$. For the sake of computational efficiency of the tricubic interpolation a linear transformation $\mathcal{A} : \{\mathbf{G}_1, .., \mathbf{G}_n\} \mapsto \{\mathbf{C}_1, .., \mathbf{C}_n\}$ is defined, where $\{\mathbf{C}_1, .., \mathbf{C}_n\}$ are vectors of a simple cubic grid. $\mathcal{A}$ transforms the unit cell vectors of $\{\mathbf{G}_1, .., \mathbf{G}_n\}$ to the unit cell vectors of $\{\mathbf{C}_1, .., \mathbf{C}_n\}$. Furthermore it is noted that $S(\mathbf{G}_i) = S(\mathcal{A}^{-1}\mathbf{C}_i)$ and the auxiliary function $\mathscr{S}(\mathbf{C}_i) := S(\mathbf{G}_i)$ is defined. In order to obtain a more accurate estimate of the integral of $\sum_{\mathbf{G}} S(\mathbf{G}) v(\mathbf{G})$ the following procedure is pursued. Values of $\mathscr{S}$ are calculated using the tricubic interpolation at additional points on an arbitrarily dense simple cubic grid $\{\mathbf{D}_1, .., \mathbf{D}_n\}$, which is chosen to be $N_x \times N_y \times N_z$ times denser than the original one. Once obtained, the interpolated function and analytic expression of the Coulomb kernel can be employed to calculate the correlation energy using

$$E_c = \frac{1}{N_x N_y N_z} \sum_i v(\mathcal{A}^{-1}\mathbf{D}_i) \mathscr{S}(\mathbf{D}_i) . \tag{6.11}$$

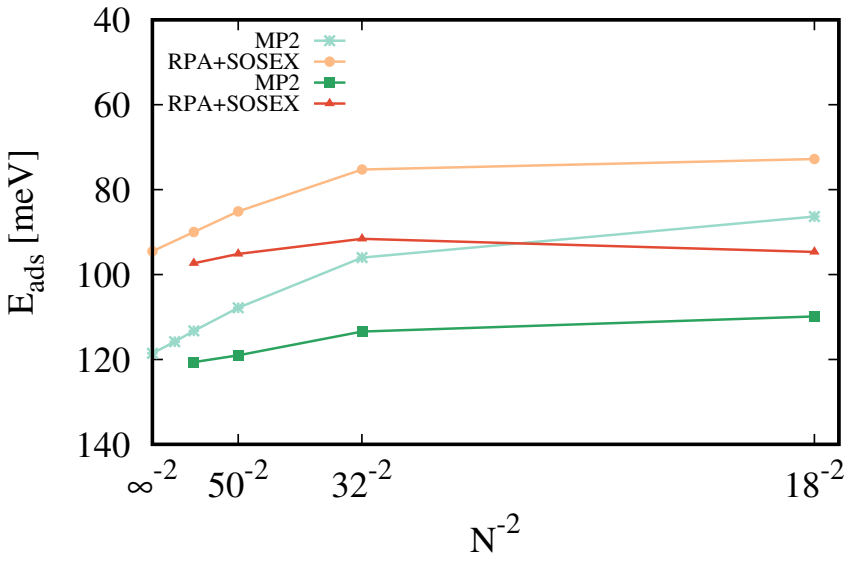

FIGURE 6.6: Adsorption energy of a single water molecule on a *h*-BN sheet. The MP2 and RPA+SOSEX energies are retrieved as a function of atoms in the sheet. FS3D indicates that finite-size corrections are included. Calculations employ a pseudized aug-cc-pVTZ basis set and include counterpoise corrections.

An $N_x = N_y = N_z = 50$ grid yields well converged correlation energies while the computational cost of the tricubic interpolation remains negligible.

As a demonstration of the applicability of the proposed method to reach the thermodynamic limit the adsorption energy of a single water molecule on an *h*-BN sheet is computed. The adsorption energy is defined as the difference in energy between the non-interacting fragments (water and the *h*-BN surface) and the interacting system (water molecule on *h*-BN),

$$E_{\text{ads}} = E_{\text{H}_2\text{O}} + E_{h\text{-BN}} - E_{\text{H}_2\text{O}+h\text{-BN}} \,. \tag{6.12}$$

To illustrate the importance of the interpolation method, the structure factor of the interacting system is considered. In Fig. 6.5 the structure factor as a function of the magnitude of the **G**-vectors along the x-direction is shown. The $\mathbf{G} = 0$ limit is approached only very slowly with increasing number of substrate atoms. Furthermore, the recent work of Al-Hamdani *et al.* [65] illustrates the importance of long-range correlation effects that account for approximately 25% of the reference adsorption energy computed in a (4×4) unit cell of *h*-BN. Figure 6.6 shows calculated adsorption energies at the level of RPA plus second-order screened exchange (RPA+SOSEX) [92] and MP2 theories

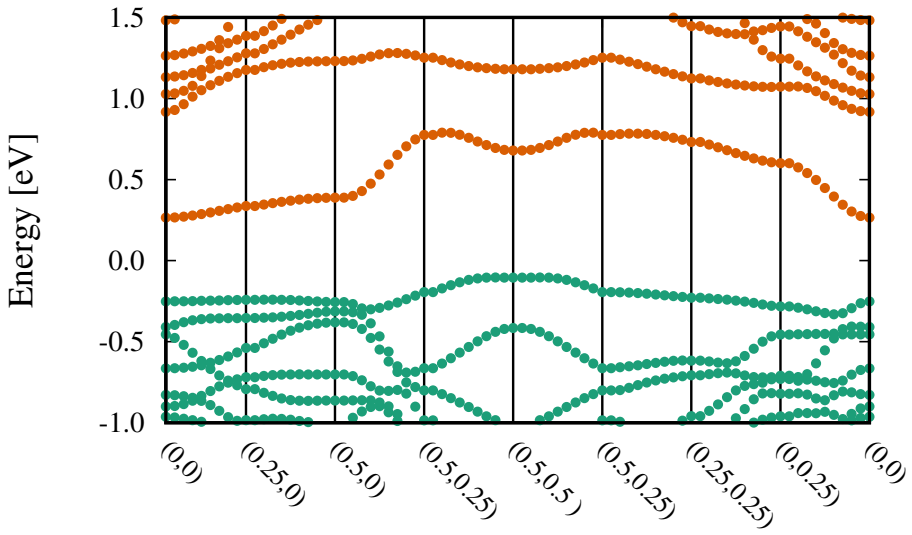

FIGURE 6.7: Hydrogen dissociation on Si(001) surface. Band structure at the level of PBE for the transition geometry. On x-axis are the k-points across a line over k-points of a Γ-centered $4 \times 4 \times 1$ k-mesh.

retrieved as a function of the number of atoms in the h-BN sheet. The same settings as in the study of the PGTOs are used, together with the aVTZ Gaussian basis set. Using MP2 theory it is possible to study very large systems [65] and it is found that the MP2 adsorption energy converges slowly to a thermodynamic limit value of 119 meV. It is noted that finite size errors for adsorption energies on two dimensional insulators are expected to decay as $1/N^2$, which is the predicted scaling from pairwise additive van der Waals interactions [65]. Applying the proposed finite size correction to MP2 theory for the (4×4) unit cell h-BN sheet with 32 atoms yields an adsorption energy of 113 meV in close agreement with the thermodynamic limit result. We observe a similar speed-up in convergence using RPA+SOSEX-FS theory, illustrating the transferability of the proposed method.

Let us now turn to the discussion of the slow convergence of $S(\mathbf{G})$ with respect to the employed supercell size or k-point mesh in small band-gap systems. Apart from long-range correlation effects small band-gap systems suffer from significant fluctuations in the one-particle band structure. This can be illustrated by the band structure in Fig. 6.7. Sampling the supercell of Fig. 8.1 using a $4 \times 4 \times 1$ k-mesh instead of the Γ-point results in different orbital eigenergies depending on the k-point. In the case of MP2 the amplitudes T_{ij}^{ab} in Eq. (6.10) are given by Eq. (3.47), i.e.,

$$T_{ij}^{ab} = \frac{V_{ij}^{ab}}{\varepsilon_i + \varepsilon_j - \varepsilon_a - \varepsilon_b} \,. \tag{6.13}$$

Due to the fluctuations in the band structure the denominator of Eq. (6.13) can vary significantly when increasing the k-point mesh. This is in contrast to high band-gap insulators where the corresponding band structure would be almost flat with respect to k-points, resulting in negligible difference in orbital eigenenergy differences for different k-points. At the level of correlated methods this problem can be ameliorated by the twist-averaging technique, i.e., calculating and averaging $S(\mathbf{G})$ for a set of shifted k-point meshes. It should be noted that the vectors $\mathbf{G}$ are not affected by shifting the employed k-mesh because $\mathbf{G}$ depends only on the difference between any two Bloch wave vectors. Thus the structure factor can be calculated on a Γ-centered grid for all different k-points. The twist-averaged structure factor for a set of N_t different k-point shifts is given by

$$\bar{S}(\mathbf{G}) = \frac{1}{N_t} \sum_{i=1}^{N_t} S_i(\mathbf{G}) \ . \tag{6.14}$$

The shifts are chosen such that they mimic a uniform Γ-centered k-mesh in the Brillouin zone. The correlation energy can then be calculated using this twist-averaged structure factor.

Chapter 7

Water physisorption on periodic surfaces

Molecular adsorption and diffusion on surfaces is central to countless industrial applications, including catalysis, gas storage, desalination, and more. Of all the many and varied molecular adsorption systems, few are of greater importance than those involving water. Water adsorption on the so-called vdW materials is particularly exciting as they exhibit peculiar long-range correlation interactions compared to bulk solids or molecules. Many of these exciting properties of water on vdW surfaces lack a full molecular level understanding of the processes and the mechanisms involved. In order to gain further insight, it is necessary to complement experimental investigations with theoretical approaches. One of the most fundamental properties of molecular adsorption on periodic surfaces is the strength and the physical nature of the interaction. Accurate electronic structure methods can therefore complement experimental data, by providing reference adsorption energies.

In this Chapter periodic MP2 and CC methods are applied to investigate water adsorption on the ionic crystal LiH, and the two-dimensional surfaces of *h*-BN and graphene. Wherever available, different methods are compared such as local quantum chemical techniques for periodic systems and Quantum Monte Carlo (QMC) calculations.

7.1 Water adsorption on the (001) LiH surface

As a first application, water adsorption on the surface of a LiH crystal is studied. Although dissolution is the fate of this ionic crystal upon solvation, it can serve as an important benchmark system for several wave function based methods. Furthermore,

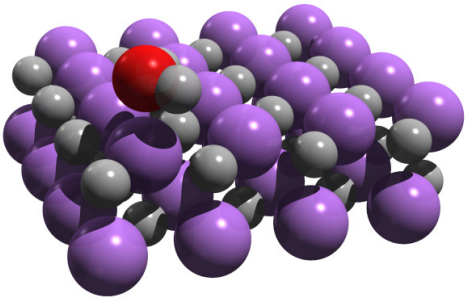

FIGURE 7.1: The adsorption geometry of water on a two-layer slab with 64 atoms per cell, representing the (001) LiH surface. The oxygen–surface distance is 2.15 Å, while the water molecule almost retains its equilibrium structure. The geometry was optimized using the PBE functional. The picture is taken from Ref. [97]

the relatively small number of electrons involved allows for an in-depth comparison of different post-mean-field methods. Periodic MP2 and CC theory are employed for the calculation of the adsorption energy of a single water molecule on the (001) LiH surface, keeping the atomic structure of the surface fixed. The adsorption energy is defined as the difference in energy between the non-interacting fragments (water and the LiH surface) and the interacting system (water molecule on LiH),

$$E_{\text{ads}} = E_{\text{H}_2\text{O}} + E_{\text{LiH}} - E_{\text{H}_2\text{O+LiH}} \ . \tag{7.1}$$

Since the primary interest is benchmarking different electronic-structure methods, zero-point energy contributions or finite temperature effects are neglected. The structure of the surface with the adsorbed molecule has been obtained in the following manner. The Li and H atoms have been kept fixed to their pristine lattice sites with a lattice constant of $a = 4.084$ Å, consistent with previous studies of the LiH crystal [93–95]. This has the advantage of keeping the geometry consistent when supercells or fragments of different sizes are used in quantum chemical and DFT calculations. The water molecule was relaxed on the LiH (001) surface using the Perdew–Burke–Ernzerhof (PBE) XC functional [7] and a two-layer slab with the 4×4 surface supercell. A vacuum gap of 20.5 Å has been employed to ensure that the surface slab does not interact with its periodic image. The relaxed geometry of the water molecule adsorbed on the LiH surface is shown in Fig. 7.1. The DMC adsorption energy curve obtained by varying the distance between the molecule and the surface, agrees well with the oxygen–surface distance of the PBE functional (2.15 Å) [96]. This geometry is used throughout this Section for all density-functional and correlated calculations.

7.1.1 Computational details

The calculations have been performed using the VASP code employing the PAW method alongside with the Γ-point approximation to sample the first Brillouin zone. The kinetic energy cutoff that determines the size of the plane-wave basis set expansion of the one-particle states was set to 500 eV. There are numerous density-functionals that could be considered, of which only a small selection have been chosen. The accuracy of one of the most widely-used functionals, the PBE functional, is assessed, as well as of several van der Waals functionals. Specifically, dispersion corrections were taken into account following the approach of Grimme *et al.* [98], the method of Tkatchenko and Scheffler [99], and the vdW-DF method proposed by Dion *et al.* [100–103], as implemented in VASP. In the former schemes a correction is added to the DFT total energy after the self-consistent-field (SCF) cycle is converged, whereas the latter scheme is a non-local correlation functional that approximately accounts for dispersion interactions. In all calculations all electronic states of the H and Li atoms were treated as valence states, whereas the $1s^2$ states of the O atom were kept frozen. Supercells of different sizes were used to model the LiH surface, containing 32, 64, and 128 atoms.

For wavefunction-based correlation techniques PGTOs are employed, as presented in Section 6.1, expanded in a plane-wave basis set to span the virtual orbital manifold necessary for the quantum chemical MP2 and CC methods. For the present calculations Dunning's contracted aug-cc-pVDZ (AVDZ), aug-cc-pVTZ (AVTZ), and aug-cc-pVQZ without g angular momentum functions (AVQZ–g) basis sets [66, 67] were pseudized and expanded in a plane-wave basis set. Augmented functions were not included for the Li atom because they possess a small exponent for the radial part that introduces linear dependencies in the virtual orbital space. The AVQZ–g basis set used here does not encompass g angular momentum functions since the corresponding pseudization procedure has not yet been implemented in VASP. Counterpoise corrections (CP) to the basis set superposition error (BSSE) [85] were included in all correlated quantum-chemical calculations with plane-waves that employ PGTOs for the virtual states.

Canonical periodic MP2 calculations using PGTOs were performed with the VASP code [38, 104]. The Coulomb vertex was expanded on a plane-wave grid, using a kinetic energy cutoff E_χ of 200 eV. All reported MP2 adsorption energies have been checked for convergence with respect to this cutoff. Table 7.1 shows the convergence of the MP2 adsorption energy with respect to the cutoff energy.

Periodic CCSD calculations were performed using the Coulomb vertex and the two-electron-four-index integrals calculated within the PAW method in VASP, as shown in Eqs. (4.27) and (4.29). It is stressed that the employed CCSD implementation does

TABLE 7.1: MP2 adsorption energy against the cutoff energy E_χ of the auxiliary basis set. One-particle states were expanded in a plane-wave basis set with a cutoff of 500 eV, while the virtual states were constructed using a pseudized AVTZ basis set.

E_χ [eV]	E_{ads} [meV]
50	242
100	214
150	211
200	211
250	211
300	211

not involve the low rank factorization of the two-electron integrals or the OAF approximation. In order to further reduce the computational cost pseudized Gaussian orbitals were considered only for the atoms of the top-most layer of the LiH slab. In a second step, the auxiliary plane-wave basis, required for the evaluation of the Coulomb vertex was truncated using a kinetic energy cutoff of 100 eV. MP2 calculations reveal that this approximation yields adsorption energies that deviate by 3 meV from those obtained using a cutoff of 200 eV as indicated in Table 7.1.

Finally, a δCCSD(T) correction was applied as the difference between canonical periodic CCSD(T) and MP2 calculations using the AVDZ PGTOs (placed in the top-most layer) and an H_2O+Li_8H_8 simulation cell.

7.1.2 Finite-size and basis set convergence

The finite-size and the basis set convergence studies summarized in this section employ a 2-layer LiH substrate as shown in Fig. 7.1. DFT-PBE and HF adsorption energies with respect to the system size using different implementations are summarized in Table 7.2. Converged results are in excellent agreement using plane-waves and Gaussian basis sets, with VASP and CRYSTAL respectively [97]. DFT-PBE results are converged already with a 32-atom LiH surface slab due to the inability of DFT-PBE to describe long-range dispersive interactions. HF results also exhibit a very fast rate of convergence albeit underestimating the adsorption energy compared to DFT-PBE significantly due to the neglect of any electronic correlation effects.

Canonical MP2 energies need to be converged with respect to both the basis set size and to the LiH surface size. Table 7.3 summarizes canonical MP2 adsorption energies obtained for varying basis set and supercell sizes. AV(D,T)Z and AV(T,Q–g)Z extrapolated adsorption energies agree to within $2-6$ meV for all studied system sizes. It is

TABLE 7.2: DFT-PBE and HF adsorption energies for water on 2-layer LiH substrates with different number of atoms in the supercell and different k-meshes. The reference 2-layer geometry with 64-atoms is shown in Fig. 7.1. The DFT-PBE and HF calculations have been performed with VASP and employ a 500 eV kinetic energy cutoff. HF CRYSTAL calculations with an AVTZ-quality basis set and a $3 \times 3 \times 1$ k-mesh yield a value of 14 meV [97].

	E_{ads} (meV)		
k-mesh	No. of atoms	PBE	HF
(Γ-point)	32	219	10
(Γ-point)	64	215	14
(Γ-point)	128	215	15
($3 \times 3 \times 1$)	64	214	15

TABLE 7.3: Canonical MP2 adsorption energies for water on 2-layer LiH substrates with different number of atoms in the computational supercell. The calculations were performed with VASP and employ PGTOs for the virtual orbitals alongside the Γ-point approximation. The thermodynamic limit is obtained from an $1/N^2$ extrapolation (N denotes the number of atoms in the LiH substrate).

	$E_{\text{ads}}^{\text{MP2}}$ (meV)				
Atoms	AVDZ	AVTZ	AVQZ–g	AV(D,T)Z	AV(T,Q–g)Z
32	162	193	198	207	201
64	181	211	218	224	222
72	185	213	220	226	224
128	188	218	228	231	235
∞	189	219	227	231	233

The LMP2-F12 and LMP2-pF12 adsorption energies are 238 and 235 meV respectively [97].

noted that the AV(T,Q–g)Z extrapolation is somewhat less reliable due to the absence of g angular momentum functions in the AVQZ values. The MP2 adsorption energies converge as $1/N^2$, where N denotes the number of atoms in the LiH substrate. This behavior is expected from the long-range decay of pairwise van der Waals contributions in two-dimensional systems. The convergence of the finite-size effects for the various basis set extrapolated MP2 results can be seen in Fig. 7.2. Using the $1/N^2$ behaviour MP2 adsorption energies can be extrapolated to the thermodynamic limit ($N \to \infty$), yielding 231 meV and 233 meV for AV(D,T)Z and AV(T,Q–g)Z, respectively. In Fig. 7.2 canonical plane-wave MP2 calculations are compared with periodic local MP2 (LMP2) ones [105, 106]. Despite a $5-7$ meV difference between the canonical MP2 and LMP2-F12, that is likely due to the remaining basis set incompleteness in the correlation energy of the former, the agreement of the two different schemes is impressive. The F12-based explicit correlation techniques combined with local approximation schemes accelerate

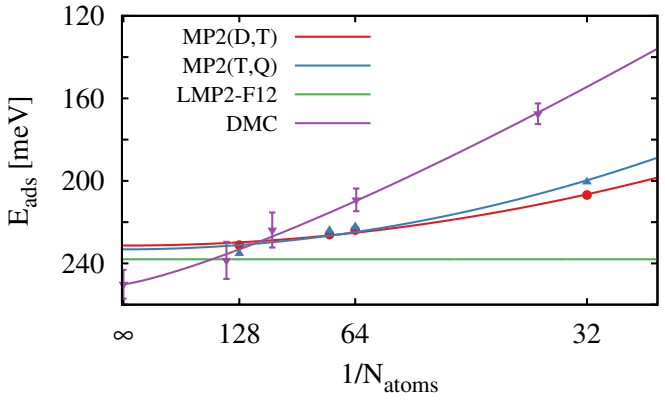

FIGURE 7.2: Dependence of the adsorption energy E_{ads} of H_2O on LiH on the number of atoms of the substrate at different levels of theory and basis set extrapolations. The fitted lines correspond to $1/N^2$ for the MP2 energies and $1/N^{5/4}$ for the DMC energies. MP2 results employ AV(D,T)Z and AV(T,Q)Z basis set extrapolations [108]. LMP2-F12 result corresponds to the thermodynamic limit. On the x-axis N_{atoms} is indicated instead of $1/\text{N}_{\text{atoms}}$.

the convergence of the MP2 correlation energy. Its close agreement with the periodic canonical results suggests that PGTOs provide an adequate virtual basis set for correlated calculations in plane-waves.

The DMC adsorption energy [96, 97] converges more slowly with respect to the supercell size than the MP2 energy as shown in Fig. 7.2, due to the long ranged nature of the real-space exchange-correlation hole and reduced screening in lower dimensional materials. Drummond *et al.* proposed a $1/N^{5/4}$ extrapolation for two-dimensional systems [107]. Despite its statistical uncertainty, the thermodynamic limit of the DMC adsorption energy suggests that the MP2 error for this system is small but not negligible and thus a higher-order quantum chemical treatment is desirable.

Periodic coupled-cluster calculations were performed with PGTOs building up the virtual orbitals. However, these Gaussian-type functions were placed only on the top-most layer of the LiH surface to reduce the computational cost. Additionally, only supercells with 32 and 64 atoms were used to model the LiH slab. AVDZ and AVTZ Gaussian basis sets were used for the construction of the PGTOs, and all results are extrapolated with respect to the basis set and the number of atoms in the supercell. MP2 results utilizing Gaussian orbitals for the full LiH surface and a thermodynamic-limit extrapolation using four points, verify that correlation effects are captured adequately via only top-most layer virtual states and a thermodynamic-limit extrapolation using two points. The error of this simplification is about 1 meV in the MP2 energy. Consequently, it is reasonable to assume that coupled-cluster results obtained using the same simplification provide a similarly converged estimate. MP2 and coupled-cluster results are summarized in Fig. 7.3. The CCSD adsorption energies are close to those of MP2, differing only by

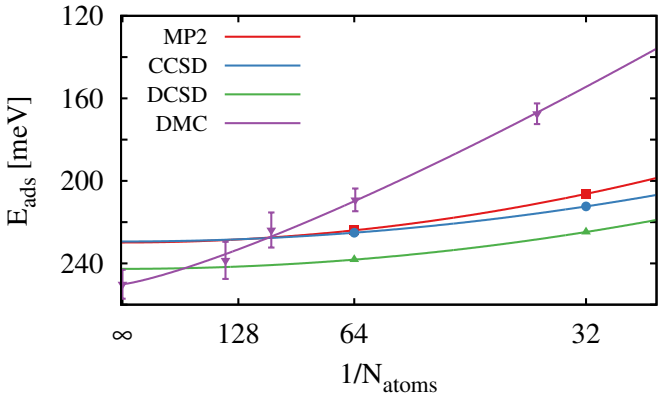

FIGURE 7.3: Adsorption energy E_{ads} of H_2O on LiH for different supercells sizes and levels of theory. Coupled-cluster and MP2 calculations were done using PGTOs only on the top-most layer of the LiH substrate. The fitted lines correspond to $1/N^2$ for the coupled-cluster and MP2 energies and $1/N^{5/4}$ for the DMC energies. The coupled-cluster and MP2 results employ AV(D,T)Z basis set extrapolation [108]. On the x-axis N_{atoms} is indicated instead of $1/\text{N}_{\text{atoms}}$.

1 meV. However, the extrapolated DCSD results deviate quite significantly from the CCSD and MP2 results, yielding an adsorption energy of 243 meV in better agreement with the DMC values.

Finally, a δCCSD(T) correction scheme was applied to the canonical and the MP2 results. The correction δCCSD(T) was defined as

$$E^{\delta\text{CCSD(T)}} = E^{\text{MP2}}_{\text{H}_2\text{O}+(\text{LiH})_\infty} + E^{\text{CCSD(T)}}_{\text{H}_2\text{O}+\text{Li}_8\text{H}_8} - E^{\text{MP2}}_{\text{H}_2\text{O}+\text{Li}_8\text{H}_8} \ , \tag{7.2}$$

where canonical CCSD(T) and MP2 calculations were performed using an H_2O+Li_8H_8 2-layer supercell (with an identical orientation of the water molecule as for the larger supercells) and an AVDZ basis set in a plane-wave representation. $E^{\text{MP2}}_{\text{H}_2\text{O}+(\text{LiH})_\infty}$ is the thermodynamic limit of the MP2 adsorption energy using AVD(T,Q–g)Z basis set extrapolation. This yields an adsorption energy of 254 meV. A similar δCCSD(T) correction to the LMP2-F12 results using finite clusters has been applied in Ref. [97], that yields an adsorption energy of 256 meV.

Finally, it is noted that calculations of the adsorption energy with respect to the number of layers [97] reveal that for the non-dispersive contributions, the two-layer slab is already an adequate model. Dispersion on the contrary, is not entirely converged with just two LiH-layers, however, at the scale of the whole adsorption energy, the lack of a few meV of dispersion in the two-layer model can be tolerated.

7.1.3 Comparison of adsorption energies

The converged adsorption energies are now summarized and compared to a small set of widely-used density-functionals. All reported results employ a 2-layer LiH substrate as in Fig. 7.1. The mutually agreeing DMC and δCCSD(T) results can be considered as the most reliable benchmark for the present system, yielding adsorption energies between 250 ($\pm$7) meV and 256 meV. For comparison, the adsorption energy of each method is depicted in Fig. 7.4. A sizable variation in the adsorption energies is evident between different van der Waals functionals (PBE-TS [99], optB86b-vdW [103], PBE-D3 [98], HSE06-D3 [109], RPBE-vdW-DF [100]), as well as PBE. The PBE functional underestimates the adsorption energy by roughly 45 meV, in a large part due to its lack of dispersive interactions. Grimme's D3 correction [98] accounts for such interactions, albeit overestimating the adsorption energy for the current system, predicting a PBE-D3 adsorption energy of 350 meV, consistent with similar findings for water adsorption on ionic surfaces [110]. We note that this overestimation is less pronounced when the HSE06 [111, 112] hybrid functional is used in conjunction with D3, yielding a value of 306 meV. This can partly be attributed to the fact that the HSE06 functional underestimates the adsorption energy compared to PBE by as much as 85 meV. The optB86b-vdW [103] results also overbind the water molecule by roughly 45 meV, while the RPBE-vdW-DF [100] adsorption energy exhibits a similar underbinding as for the case of PBE. The best van der Waals functional estimate is provided by the Tkatchenko and Scheffler functional (PBE-TS) with iterative Hirshfeld partitioning [113, 114]. The latter yields an adsorption energy of 268 meV in good agreement with δCCSD(T) results. These results illustrate the difficulties in van der Waals functionals. The PBE functional is known to provide a non-electrostatic binding between closed shell systems. This attraction is rather an artifact than a real dispersive interaction. At the same time, this artificial attraction provides a quantitatively reasonable effective substitute for dispersion. However, if the physically correct dispersion is added on top, it becomes difficult to avoid double counting, leading to a deterioration of the quantitative accuracy.

Figure 7.4 also shows the various wave function estimates of the adsorption energy. Canonical MP2 theory underestimates the adsorption energy by 17 meV compared to DMC, while LMP2-F12 provides a slightly better estimate, partly due to the explicit correlation, leading to an improved convergence with respect to the basis set size. The LMP2-F12 adsorption energy is 238 meV, only 11 meV below the DMC result. CCSD constitutes no improvement over MP2 theory for the present case, yielding a binding energy of 229 meV only. The DCSD approximation [61], consistent with findings in molecular systems [61–63], considerably improves the description of water adsorption on LiH, predicting an adsorption energy of 243 meV, which is within the stochastic error

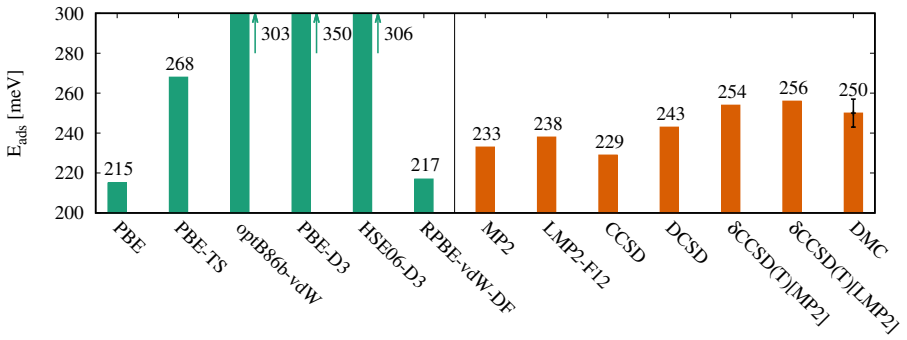

FIGURE 7.4: Converged adsorption energies of a water molecule on a LiH surface at different levels of theory. PBE and several van der Waals functionals shown on the left. Wave function based methods ranging from MP2 to δCCSD(T) and DMC shown on the right.

of DMC but still underbinding compared to the triples corrected δCCSD(T) results. In summary, high-level quantum chemistry and QMC techniques are excellent in agreement as well as different methods for computing MP2 adsorption energies between them. Furthermore the correlated wave function based methods yield estimates for the binding energy that lie in a relatively narrow energy window ranging from 229 meV to 256 meV.

7.1.4 Conclusions

A comprehensive comparison between different electronic structure methods including wavefunction-based theories and a small selection of density-functionals have been employed for the prediction of the adsorption energy of a single water molecule on the (001) LiH surface.

Quantum chemical methods are systematically improvable, hence yielding increasingly accurate adsorption energies as one moves up the hierarchy to higher orders of theory. Distinguishable cluster theory and inclusion of triple excitations to CCSD theory give the best agreement with DMC results. MP2 and CCSD reach a similar level of accuracy for this system, slightly underbinding the water molecule on the LiH surface by roughly 20 meV. A good agreement is found between periodic canonical and local implementations utilizing explicit correlation technique for improved basis set convergence. All this demonstrates that quantum chemical approaches are becoming a robust and reliable tool for condensed phase electronic structure calculations.

Van der Waals functionals on the other hand, yield a significantly larger spread of adsorption energy estimates compared to the employed many-electron theories. The under- and overestimations compared to DMC and δCCSD(T) are as large as 30 meV

(RPBE-vdW-DF) and 100 meV (PBE-D3), respectively. Although the PBE-TS functional achieves good agreement with the DMC and δCCSD(T) estimates for the present case, it remains difficult to achieve such a high level of accuracy for a wide class of materials using van der Waals functionals. This study contributes another benchmark system to the literature that can be used to further improve upon the currently available and computationally very efficient van der Waals functionals for cases where higher accuracy is needed.

7.2 Water adsorption on *h*-BN

Two-dimensional materials have attracted great interest since the discovery of graphene [115, 116], due to their unusual and promising properties for potential applications. Another material that belongs to this family is hexagonal BN, that crystalizes in a hexagonal honeycomb structure and has a lattice constant similar to graphene. It consists of B and N atoms that hybridize to sp^2 orbitals, forming a strong σ bond. Experimental results have revealed fascinating properties of water on *h*-BN [117, 118]. One of the most fundamental questions of any water–BN system is the water monomer adsorption energy on *h*-BN. While experimental results are difficult to obtain, accurate simulation data can have a key role in providing reference energies.

DFT calculations vary significantly, depending on the XC functional that is employed, or whether dispersion is included. DMC and RPA calculations [119, 120] have provided accurate benchmark energies for the adsorption. In this work the adsorption energy is revisited using periodic MP2, CCSD, and CCSD(T) theories, and compare them with DFT as well as with the accurate DMC and RPA results. Additionally, the adsorption energy of water on *h*-BN is compared with that of water on BN molecular complexes, such as borazine (the BN analogue of benzene), and boronene (BN analogue of coronene), illustrating the importance of accurately addressing long-range correlation effects.

7.2.1 Computational details

For the study of the adsorption energy of a single water molecule on BN the structures obtained by Al-Hamdani *et. al.* [119] have been used, whereby the molecule is oriented on top of an N site and the geometry has been optimized using the optB86b-vdW functional. The water–N distance was set to 3.25 Å, since the MP2 adsorption energy has the largest value at that distance [65]. A $4\times4\times1$ *h*-BN monolayer supercell was used at its pristine geometry, containing 32 B and N atoms, and the distance between two BN sheets was set to 16 Å. A 600 eV kinetic energy cutoff for the one particle orbitals was

employed along with Γ point sampling of the Brillouin zone. The B $2s^2 2p^1$, N $2s^2 2p^3$, O $2s^2 2p^4$, and H $1s^1$ states have been treated as valence states. The PAW method was employed for the interactions between valence electrons and ionic cores. Occupied HF states were converged within the full plane wave basis. PGTOs based on Dunning's aug-cc-pVTZ (AVTZ) [66, 67] basis set, mapped onto a plane-wave representation, form the virtual orbital manifold for the correlated calculations. Details of the underlying procedure are given in Section 6.1 and Refs. [68, 121]. The Fourier transformed overlap densities were expanded using an auxiliary plane-wave basis with a kinetic energy cutoff that was set to 300 eV [38, 104, 121, 122]. The adsorption energy is defined as the difference in energy between the non-interacting fragments and the interacting system

$$E_{\text{ads}} = E_{\text{H}_2\text{O}} + E_{\text{BN}} - E_{\text{H}_2\text{O+BN}}. \tag{7.3}$$

Counterpoise corrections to the basis set superposition error (BSSE) were included in all quantum chemical calculations employing the PGTOs. Convergence of the adsorption energy with respect to all involved parameters was checked thoroughly. The $N_G = 8270$ momentum grid points, employed to evaluate the Coulomb vertex $\tilde{\Gamma}^q_{rG}$, are approximated by $N_F = 1800$ field variables associated with the largest singular values of the Coulomb vertex. The Coulomb vertex is further decomposed into a contraction of three rank-two tensors with $N_R = 5400$ indices that allows for reduced scaling CCSD calculations, as explained in Sec. 5.2 and Ref. [121]. The finite size correction based on a tricubic interpolation of the correlation energy structure factor was also employed to ensure thermodynamic limit convergence. The δCCSD(T) correction was computed using an 18-atom h-BN substrate alongside an AVDZ PGTO basis set and was defined as the difference between the periodic canonical CCSD(T) and periodic canonical CCSD adsorption energy.

7.2.2 Results

It has already been demonstrated that long-range electronic correlation effects can be particularly important in low dimensional systems like water adsorption on h-BN. The weak physisorption energy calls for electronic structure methods with subchemical accuracy. Furthermore, the work of Al-Hamdani *et al.* [65] illustrates the importance of long-range correlation effects that account for approximately 25% of the reference adsorption energy computed in a 4×4 supercell of h-BN. Here periodic quantum chemical results are presented for the adsorption energy and compared with different electronic structure theory methods.

TABLE 7.4: Interaction energies in meV for water on h-BN at 3.25 Å with increasing number of atoms in the h-BN substrate. $\Delta E_{\text{int}}^{\text{fse}}$ is the difference in the interaction energy due to finite-size effects for water with 32 and 98 atoms in the h-BN unit cell.

No. of atoms	MP2	RPA	RPA+SE	PBE0+MBD
18 (3×3)	-70	-34	-58	-88
32 (4×4)	-93	-64	-84	-125
50 (5×5)	-106	-76	-95	-139
72 (6×6)	-113	-78	-97	-145
98 (7×7)	-116	-84	-103	-148
$\Delta E_{\text{int}}^{\text{fse}}$	-23	-20	-19	-23

Results are taken from Ref. [65].

Finite-size effects that arise from long-range Coulomb interactions are discussed first. In methods that account for charge fluctuations (and therefore vdW interactions) explicitly, whether it is via coupled harmonic oscillators in the Many-Body Dispersion (MBD) method [123] or via electronic excitations in the RPA, MP2, and CC theories, the fluctuations can give rise to spurious interactions with their periodic images. As such, correlated methods are affected by finite-size errors any time they are providing the energy of a macroscopic system by employing periodic boundary conditions. These errors are typically much larger than those observed in independent electron methods such as HF and DFT.

In Table 7.4 adsorption energies for increasing h-BN monolayer sizes, using the Γ-point approximation are shown. MP2 calculations employ the PGTOs to span the virtual orbital manifold, whereas RPA calculations have been performed using a cubic scaling implementation in the VASP code [65, 124–126]. Additionally, PBE+MBD calculations have been performed in Ref. [65] using the FHI-AIMS code [127–129]. For details about RPA and PBE+MBD calculations the reader is referred to Ref. [65]

The finite-size error to the interaction energy is defined as the difference in the interaction energy of water of 32- and 98-atom h-BN monolayer. It is stressed that all vdW inclusive methods, such as the aforementioned ones, all account for long-range dispersion interactions and predict a finite-size error of approximately 20 meV, exhibiting a similar convergence with respect to the number of monolayer atoms. It has already been demonstrated how the interpolation technique of the correlation energy structure factor can accelerate the convergence of the adsorption energy of the water monomer on h-BN,

yielding already thermodynamic limit results using a 32-atom monolayer. In what follows quantum chemical results, converged with respect to the basis set and finite-size effects, are present and compared them with DMC and various DFT calculations.

Adsorption energies from wavefunction-based methods are shown on the right panel of Fig. 7.5. δCCSD(T) and DMC results are in excellent agreement yielding an adsorption energy of 102 and 104 meV respectively. These results come at a higher computational cost than traditional DFT methodologies, however, they provide a reference adsorption energy that can be used to benchmark widely-used DFT methods. Quantum chemical methods, such as MP2, RPA+SOSEX, and DCSD, provide results within 10 meV of the reference number. Linearized DMC (LRDMC) calculations are also within 12 meV range from the DMC number. This example once again demonstrates the ability of quantum chemical methods to produce highly accurate interaction energies for periodic systems.

On the left side of the panel in Fig. 7.5 adsorption energies for water on *h*-BN obtained from various DFT methods are summarized. PBE underestimates the adsorption energy of water on *h*-BN by more than 50%. This comes with no surprise, given the fact that PBE does not include any non-local vdW interactions. Dispersion inclusive non-local functionals, such as vdW-DF2 [100] and optB86b-vdW [103] yield significantly larger adsorption energies than the PBE, given that vdW interactions are included. Nevertheless both functionals tend to overestimate the interaction strength by 40% and 70% respectively. Dispersion corrected functionals, such as Grimme's D3 [98] and the MBD method [130] account for vdW interaction as post-corrections to popular DFAs, such as PBE. Both schemes are very close to the vdW-DF2 result, overestimating the adsorption energy by 40%. It is noted that when using the PBE0 functional, PBE0+MBD yields an adsorption energy smaller by 9 meV, that is attributed solely to the use of the hybrid functional PBE0. Finally, the meta-GGA functional SCAN [131, 132] is examined. Despite the absence of vdW interactions, SCAN predicts an adsorption energy of 99 meV very close to the δCCSD(T) and DMC results, at a much lower cost.

The adsorption energy of water on *h*-BN has been calculated using periodic quantum chemical methods. Using the gold standard CCSD(T) method an adsorption energy of 102 meV is predicted. The agreement with DMC calculations, that yield an adsorption energy of 104 meV, is impressive. Furthermore, quantum chemical methods, such as MP2, RPA+SOSEX, and DCSD, all predict adsorption energies within 10 meV of the CCSD(T) reference. DFT-based methods, on the contrary, deviate by as much as 64 meV, although most vdW inclusive functionals overestimate the adsorption energy by roughly 40 meV.

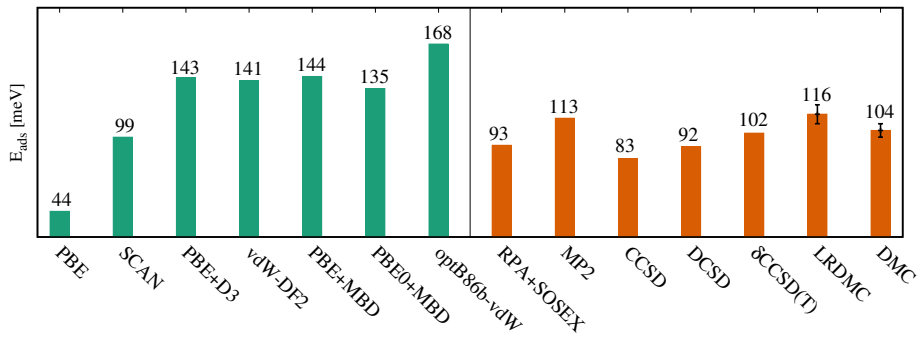

FIGURE 7.5: Converged adsorption energies of water monomer on *h*-BN monolayer at different levels of theory. PBE and several van der Waals functionals shown on the left. Wave function based methods ranging from MP2 to δCCSD(T) and DMC shown on the right.

7.3 Water adsorption on Graphene

Of all the many two-dimensional materials, few are of greater importance than graphene [115, 116]. In particular, there is a great interest in water–carbon interfaces, such as graphene and carbon nanotubes [133–135]. One of the most fundamental questions of water adsorption on graphene is the strength of the bond. DFT results vary strongly depending on the XC functional that is employed or whether dispersion forces are accounted for. Finite clusters, such as fused benzene rings, have been used with quantum chemical methods to estimate water adsorption on graphene [136–138]. Ma *et. al.* calculated water monomer adsorption on graphene using periodic DMC and RPA [139]. The authors reported small values of the interaction energy, suggesting that vdW inclusive functionals overestimate the bond strength. The prototypical water–graphene system is studied with periodic coupled cluster theory and the predicted adsorption energy is < 100 meV, in close agreement with recent periodic DMC and RPA calculations [140]. Interestingly, different adsorption energies of water on graphene and on molecular clusters, such as benzene, coronene, and circumcoronene are observed [140, 141].

7.3.1 Computational details

Water monomer adsorption on graphene is considered in three different motifs, dubbed 0-leg, 1-leg, and 2-leg as shown in Fig. 7.6. A $4 \times 4 \times 1$ graphene supercell, containing 32 carbon atoms is employed alongside a vacuum of 14.79 Å between two graphene sheets to ensure little interaction between periodic images. The binding distance d_{ads} of the oxygen atom to the graphene plane is 3.10, 3.46, and 3.37 Å for the 0-, 1-, and 2-leg respectively. Periodic MP2, CCSD, and CCSD(T) calculations have been carried out following the strategy outlined in the previous Section of water adsorption

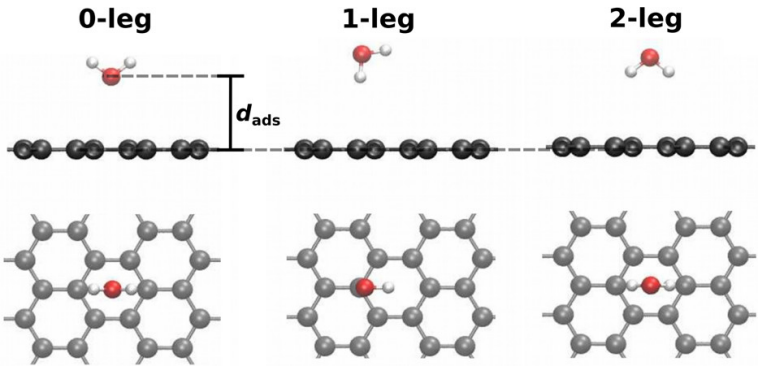

FIGURE 7.6: Water adsorption structures considered. We show the 0-leg, 1-leg, and 2-leg motif each from the side (top) and from above (bottom). The distance d_{ads} is defined as the distance of the oxygen atom from the graphene plane. All equilibrium geometries and the figure are taken from Ref. [140]

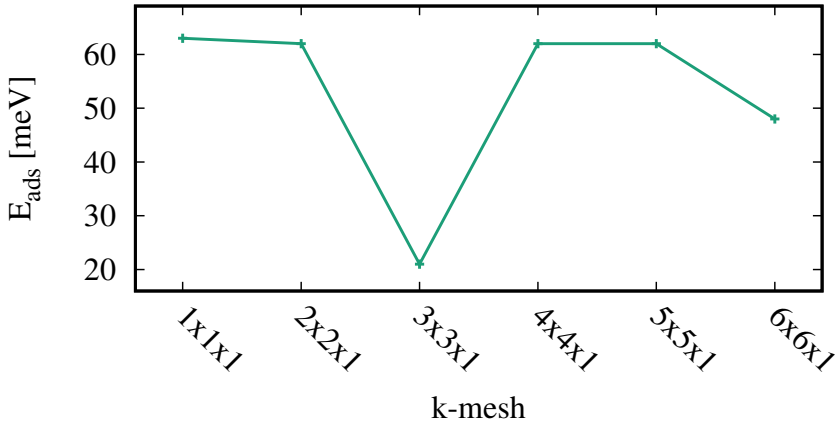

FIGURE 7.7: HF adsorption energy as function of the k-mesh. The k-meshes sample the Brillouin zone of the $4 \times 4 \times 1$ supercell.

on h-BN. Periodic HF orbitals have been computed within the PAW method with a kinetic energy cutoff for the plane-wave basis of 500 eV, whereas virtual orbitals in the CCSD calculations are projected to a pseudized aug-cc-pVTZ basis set, in a PAW representation [68]. Perturbative triples (T) are evaluated using the smaller cc-pVDZ basis set to represent the virtual orbitals. The CP corrected interaction energy is defined as

$$E_{\text{ads}} = E_{\text{H}_2\text{O+Graphene}} - E_{\text{H}_2\text{O}} - E_{\text{Graphene}} \,. \tag{7.4}$$

HF convergence with respect to the employed k-mesh is examined, before correlated methods are applied. Figure 7.7 demonstrates that the Γ-point approximation is sufficient to predict an adsorption energy to within meV accuracy at the level of HF. It should be noted, that HF does not bind the water monomer on the graphene surface. This is expected since the bond is mostly vdW driven, an interaction that is absent in HF theory. All subsequent correlated calculations employ the Γ-point approximation.

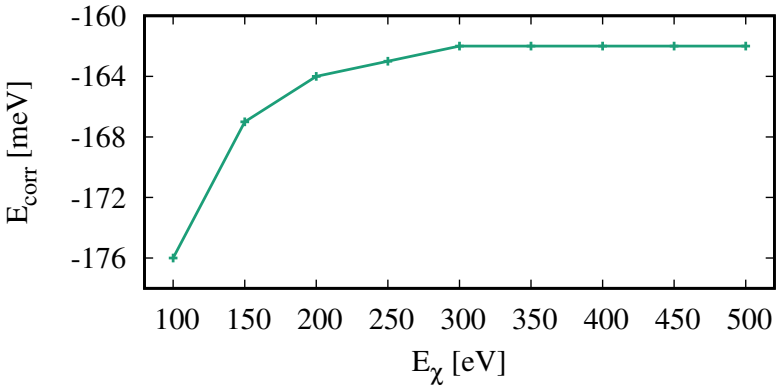

FIGURE 7.8: MP2 correlation contribution to the adsorption energy as function of the cutoff E_χ used to expand the Coulomb vertex. HF occupied orbitals are calculated within the Γ-point approximation using a 500 eV cutoff, whereas the virtual orbitals are a pseudized AVTZ basis set expanded in plane-waves.

Figure 7.8 shows the convergence of the MP2 correlation contribution to the adsorption energy as a function of the cutoff energy E_χ (see, e.g., Eq. 4.29). A rapid convergence (within meV) of the MP2 correlation energy for $E_\chi \geq 200$ eV is observed. $E_\chi = 300$ eV is therefore chosen as the cutoff for all subsequent MP2 and CC calculations. Next, the convergence of MP2 correlation energy with respect to the employed k-mesh is investigated using the twist-averaged procedure outlined in Sec. 6.3. Table 7.5 summarizes the results. The MP2 correlation energy is already converged using the Γ-point approximation. It should be stressed, however, that long range correlation effects, such as dispersion interactions, are not accounted for in the twist-averaged technique. The structure factor interpolation technique is later used to properly account for long range correlation effects. CCSD calculations employ the low-rank factorization technique for the two-electron integrals (see Sec. 5.2 and Ref. [121]). $N_R = 7488$ vertex indices are used to approximate the Coulomb vertex, as MP2 correlation energy is converged (Table 7.5). Finally, finite coverage effects are corrected for at the HF level only using a 5×5 graphene cell. Corrections to the vacuum size are computed using a supercell with a 30 Å vacuum distance at the MP2 level, and a basis set correction is also included and is defined as the difference between the full plane-wave basis set calculation and the aug-cc-pVTZ one at the MP2 level.

7.3.2 Results

Table 7.6 shows periodic quantum chemistry results for water adsorption on graphene. HF is purely repulsive for all three motifs due to the absence of any dispersion interactions. MP2 yields an interaction energy of −127 meV for the two-leg motif, that exhibits

TABLE 7.5: MP2 correlation energies as a function of the twisted k-mesh and the number of OAF variable N_f for water adsorption on a 4×4 graphene supercell. The pseudized AVTZ basis set is used for the virtual orbitals. The 1-leg O–graphene motif is employed with a distance of 3.34 and 3.46 Å , for the k-mesh and the OAF approximation respectively. All energies in eV.

k-mesh	$E^{\mathrm{corr}}_{\mathrm{MP2}}$	N_f	$E^{\mathrm{corr}}_{\mathrm{MP2}}$	$E^{\mathrm{corr}}_{\mathrm{CCSD}}$
$1 \times 1 \times 1$	-0.162	1842	-0.135	-0.097
$2 \times 2 \times 1$	-0.164	2333	-0.136	-0.095
$4 \times 4 \times 1$	-0.164	2824	-0.136	-0.094

TABLE 7.6: Water–graphene adsorption energies from quantum chemical methods. Corrections to finite-size effects, the basis set, vacuum size, and finite-coverage effects are also shown (Δ). O–graphene distance is 3.46 Å , that is the minimum of the DMC interaction energy [140]. All energies in meV.

	$E^{\text{one-leg}}_{\mathrm{ads}}$	$E^{\text{two-leg}}_{\mathrm{ads}}$	$E^{\text{zero-leg}}_{\mathrm{ads}}$
HF	42	47	34
MP2	-113	-127	-118
CCSD	-65	-75	-76
CCSD(T)	-76	-87	-84
$\Delta-$FS(MP2)	-21	-26	-25
$\Delta-$FS(CCSD)	-16	-19	-17
$\Delta-$CBS(MP2)	-5	-5	-4
$\Delta-$vacuum(HF)	1	2	2
$\Delta-$vacuum(MP2)	8	7	6
$\Delta-$coverage(HF)	1	-2	-2

the strongest binding. It is noted that the minimum of the MP2 interaction energy is at an O–graphene distance of 3.34 Å , whereas the minimum of the DMC interaction energy at a distance of 3.46 Å [140]. Subsequent calculations used the minimum distance of DMC. CCSD theory slightly underbinds the water monomer, yielding an interaction energy of -65, -75, and -76 meV for the one-, two-, and zero-leg motifs respectively. It is noted that the zero- and two-leg motifs are degenerate within CCSD theory. The gold standard method CCSD(T) yields an adsorption energy of -76, -87, and -84 for the one-, two-, and zero-leg motifs respectively. It is found that energetically the most favorable configuration is the two-leg motif.

Voloshina *et. al.* [142] reported periodic local MP2 and incremental CCSD(T) adsorption energies of water on graphene. The authors reported for the two-leg motif interaction energies of -116 and -135 meV at the level of MP2 and CCSD(T) respectively.

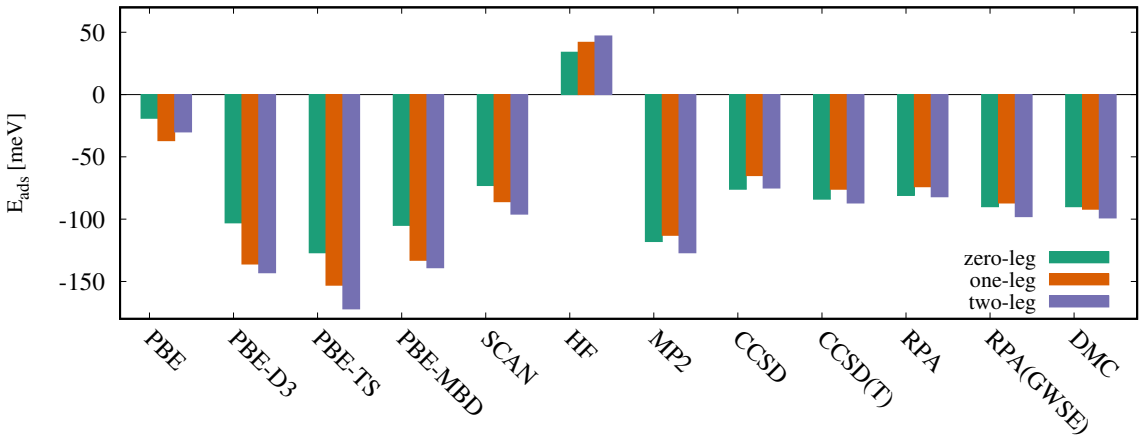

FIGURE 7.9: Water–graphene adsorption energies at different levels of theory. DMC and RPA results are taken from Ref. [140]. O–graphene distance is 3.46 Å , that is the minimum of the DMC interaction energy [140]. All energies in meV.

The MP2 interaction energy is in close agreement with the reported canonical periodic MP2 interaction energies, however, CCSD(T) calculations using the method of increments [143–146] yield a larger interaction energy compared to MP2. This is in contrast to this work's CCSD(T) calculations, that yield smaller interaction energies compared to MP2. Ma *et. al.* calculated water monomer adsorption on graphene using periodic DMC and RPA [139]. The authors reported a DMC interaction energy of −70 meV for the one- and two-leg motifs, and an RPA interaction energy of −98, and −82 meV respectively. These estimates for a benchmark binding energy range from 70 to 130 meV.

Recently, Brandenburg *et. al.* [140] revisited the adsorption problem using highly accurate electronic structure methods, that indeed agree within subchemical accuracy. The results are summarized in Figure 7.9. DMC calculations yield an interaction energy of −99 meV for the two-leg motif, whereas RPA+GWSE an interaction energy of −98 meV, both in close agreement with the periodic CCSD(T) results of −87 meV. These studies, based on state-of-the-art electronic structure theories demonstrate that different many-body electronic structure methods indeed agree within subchemical accuracy. Let us now turn to DFT-based methods. These yield interaction energies that range from −30 (PBE) to −172 meV (PBE-TS) for the two-leg motif. In the absence of dispersion interactions PBE largely underestimates the interaction energy. However, adding vdW interactions using Grimme's D3, Tkatchenko and Scheffler correction, and the many-body dispersion scheme, all overestimate the adsorption energy. SCAN predicts an interaction energy of −96 meV, very close to the DMC number.

Let us now compare the CCSD(T) results for the adsorption of water on the periodic graphene sheet to Domain local pair natural orbital (DLPNO)-CCSD(T) results of water interaction with polycyclic aromatic hydrocarbons (PAH), such as C_6H_6 (benzene),

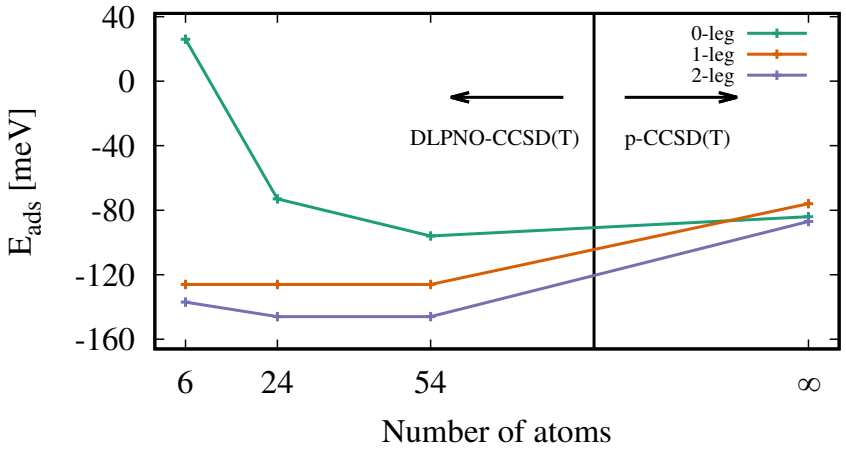

FIGURE 7.10: Water–PAH interaction energies against the number of carbon atoms in the PAH molecule. The molecular results are taken from Ref. [141], and have been computed using L-CCSD(T). O–PAH distance is fixed at 3.075, 3.289, and 3.155 Å. The ∞ symbol denotes the graphene substrate.

$C_{24}H_{12}$ (coronene), and $C_{54}H_{18}$ (circumcoronene). Figure 7.10 displays interaction energies of water monomer with PAH molecules of increasing size. Molecular results have been obtained using local-CCSD(T) theory [141], whereas the periodic results using canonical periodic CCSD(T).

For the 0-leg configuration L-CCSD(T) predicts a repulsive interaction energy with benzene (6 C atoms). With increasing number of C atoms, the water monomer bounds to the coronene and circumcoronene complexes. Furthermore, an increase in the interaction strength from −73 meV for coronene to −96 meV for circumcoronene is observed. Periodic CCSD(T) calculations yield an interaction energy for water on graphene of −84 meV. This energy is close to but smaller than the one for water on circumcoronene. The 1-leg configuration binds the water monomer to the PAH molecules, with constant strength of −126 meV. However, CCSD(T) for water on graphene yields a much smaller interaction energy of −76 meV. This is a large discrepancy between water on PAH calculated with L-CCSD(T) and water on graphene with canonical periodic CCSD(T), indicating that long-range correlation as well as screening effects of water on graphene cannot be fully mimicked using molecular PAH. For the 2-leg configuration a similar behavior is found. The interaction energy of water with benzene is −137 meV, while increasing to −146 meV for water with coronene and circumcoronene. Again when going to the periodic sheet of graphene one observes a reduction of the interaction energy to −87 meV.

It may be concluded that simulating water adsorption on graphene using a series of molecular hydrocarbon complexes may not lead to an accurate estimation of the true binding energy of water on graphene. Studies based on DFT-based symmetry-adapted

perturbation theory (SAPT) [147] revisiting the calculation of long-range electrostatics and using a series of molecular complexes, have provided interaction energies much closer to CCSD(T) and DMC estimates [148].

Chapter 8

Hydrogen dissociative adsorption on Si(100)

In this Chapter a prototypical molecule–surface reaction: the dissociative adsorption of molecular hydrogen on the Si(100) surface [149–160] is considered. In contrast to weakly physisorbed molecules this reaction is a more challenging system since the energetics of the combined molecule–surface system can vary significantly according to the rearranged chemical bonds featuring charge transfer, covalent bonding, and weak van der Waals interactions. Previous studies identify two reaction paths of dissociative H_2 adsorption, termed the intra- (H2*) and inter-dimer (H2) pathways, as shown in Fig. 8.1. Along both reaction paths, the stretch of H–H bond is accompanied by a significant modification of the characteristic buckled Si-dimer configuration in the vicinity of the molecule [160–163]. These structural modifications induce delicate changes to the electronic structure. DFT methods based on GGA capture the changes in the electronic exchange and correlation effects poorly along the reaction paths and result in too small adsorption barriers and reaction energies compared to experiments [150, 154, 155]. QMC and quantum chemistry methods using finite clusters predict adequate adsorption barriers for both pathways, however, reaction energies are overestimated [151, 157, 158]. In previous DFT and high level correlated calculations, H_2 adsorption is hindered by the smallest barrier through the H2 pathway, and the reaction occurs via a pairing mechanism [159, 160].

Here, a periodic quantum chemical description of the reaction using periodic CC theory is presented. It is shown that activation and reaction energies are calculated to within chemical accuracy compared to experimental values. Most interestingly, it becomes clear that the adsorption barriers for the H2* and H2 pathways are very similar, in contrast

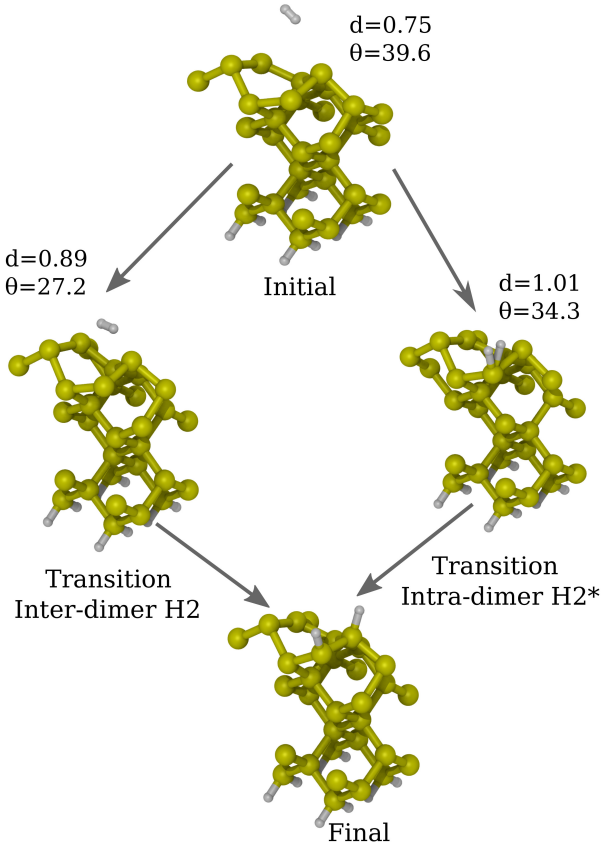

FIGURE 8.1: Intra- (H2*) and inter-dimer (H2) reaction pathways at low coverage (one H_2 molecule per two Si dimers). d denotes the bond length of the H_2 molecule in Å whereas θ the buckling angle of the Si dimers in degree.

to previous findings. It will be demonstrated that the main source of error of DFT-GGA is the self interaction error leading to an incorrect ground state density for the H2 path.

8.1 Computational details

Periodic slabs are employed for all density-functional and wavefunction based calculations. A Si(100)-2 × 2 surface with 8-layers is used, terminated with hydrogen atoms to passivate dangling bonds at the bottom layer. All calculations involve a plane-wave basis within the full potential PAW method as implemented in the VASP code [34, 36, 83, 164, 165]. In all calculations the 1s electronic states of the H atoms and the 3s and 3p states of the Si atoms were treated as valence states. The minimum energy paths of the H2* and H2 reactions are determined using the nudged elastic band (NEB) method within variational transition state theory with 8 images for the calculations [166]. For electronic structure calculations of the NEB method the PBE exchange correlation functional [7] is used. One-electron states were expanded using a plane-wave basis with a

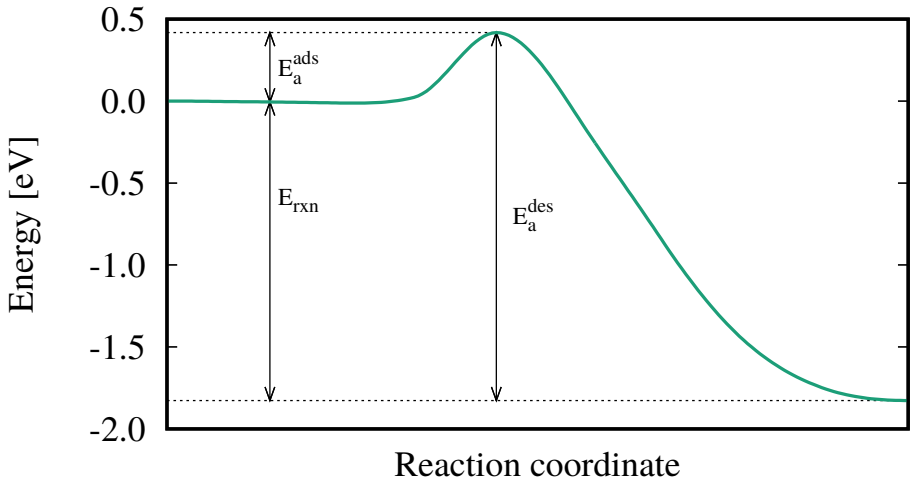

FIGURE 8.2: Hydrogen dissociation on Si(001) energetics along the intra-dimer (H2*) reaction path.

cutoff energy of 250 eV, alongside an $8 \times 8 \times 1$ k-mesh to sample the first Brillouin zone. The full reaction path energetics of the H2* pathway are shown in Fig. 8.2, with a schematic definition of the adsorption and desorption barriers, as well as the reaction energy. The exact energies of the transition states are determined by an interpolation or by using the the climbing NEB method [167]. The corresponding structures are shown in Fig. 8.1. The same geometries are used for the initial, transition, and final states to determine the reaction energy and the adsorption and desorption barriers for all methods. This allows for a direct comparison of the different levels of theory. Contributions of vibrational zero-point energies (ZPE) are included in all calculations and were taken from Ref. [157]. A $4 \times 4 \times 1$ k-mesh was employed for all subsequent DFT calculations, while the plane-wave energy cutoff was set to 500 eV. The accuracy of several density-functional approximations has been explored covering all five rungs of the Jacob's ladder of DFT. HF calculations were converged within the plane-wave basis. For MP2, CCSD and perturbative triples CCSD(T), as well as the RPA, we employ a set of atom-centered Gaussian-type functions based on Dunning's correlation consistent polarized Valence Quadruple Zeta basis set augmented with diffuse functions (aVQZ–g) [66, 67, 168], mapped onto a plane-wave representation [68], to construct the unoccupied one-electron states. The Fock matrix is always rediagonalized in order to perform a canonical correlated calculation. For the CCSD and (T) calculations the number of unoccupied states is further reduced using MP2 NOs, obtained from the virtual–virtual orbital block diagonalization of the one-electron reduced density matrix at the level of MP2 [70]. The remaining basis set incompleteness error is corrected for using an estimation based on a Γ-point full plane-wave direct MP2 calculation. A Γ-centered $4 \times 4 \times 1$ k-mesh was employed for the twist-averaging procedure (see Section 6.3) used in the MP2 and CCSD calculations, whereas the remaining finite size error of the correlation

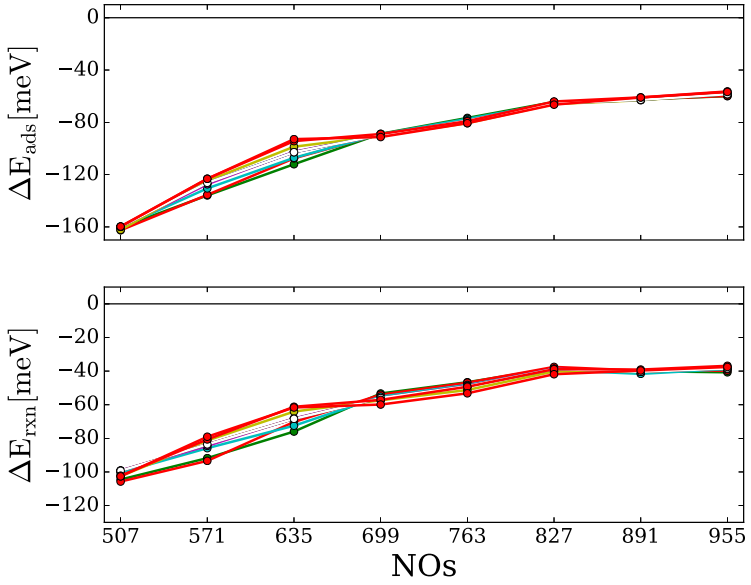

FIGURE 8.3: MP2 basis set convergence with respect to the number of NOs for the adsorption barrier (for the inter-dimer path) and the reaction energy. Each line corresponds to a different k-point in the Brillouin zone of the $4 \times 4 \times 1$ k-mesh. The energies ΔE are the difference from the MP2 value obtained using the full aVQZ–g PGTOs basis set. All energies in meV.

energy was corrected for using an interpolation technique of the structure factor on a plane-wave grid [169]. CCSD(T) results were obtained as correction to CCSD using the Γ-point approximation.

First the basis set convergence of the adsorption barriers (E_{ads}) and the reaction energy (E_{rxn}), defined as

$$E_{\text{rxn}} = E_{\text{initial}} - E_{\text{final}}, \tag{8.1}$$

and

$$E_{\text{ads}} = E_{\text{transition}} - E_{\text{initial}}, \tag{8.2}$$

respectively, is investigated. In Fig. 8.3 the convergence of the MP2 correlation energy of the different 10 k-points, shown in Table. 8.1, corresponding to the Γ-centered $4 \times 4 \times 1$ k-mesh, is shown with respect to the number of NOs. The NOs are obtained from the diagonalization of the virtual–virtual block of the one-electron MP2 reduced density matrix, using the aVQZ–g virtual states. The adsorption barriers and the reaction energy are plotted as the difference from the MP2 result, using the full aVQZ–g one-electron virtual states. A very similar behavior for all k-shifts of both the barriers and the reaction energy is observed. In particular, the basis set error for all k-shifts when we use 699 virtual NOs is the same within a few meV. It can thus be concluded that a large basis set calculation is only need for the Γ-point, since all other k-shifts exhibit the same basis set convergence. The aVQZ–g basis set limit result within a twist-averaged

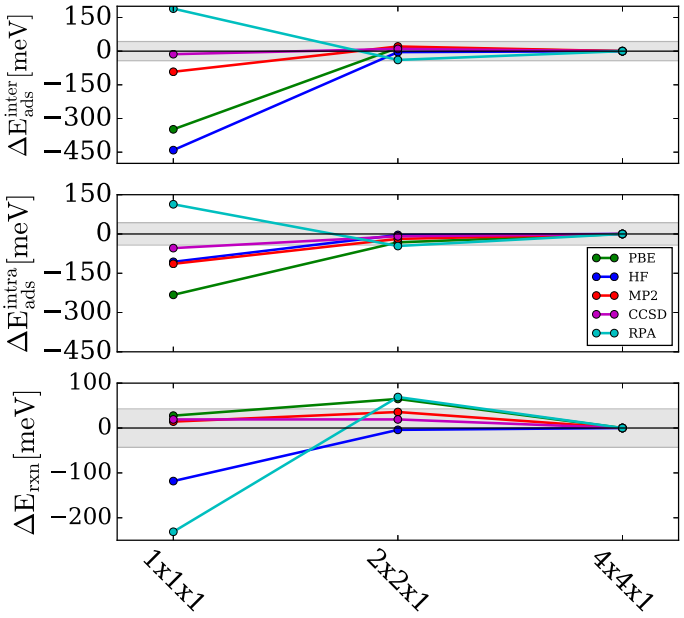

FIGURE 8.4: Dependence of the adsorption barriers for the two pathways and the reaction energy with respect to the k-mesh size. For MP2 and CCSD, we perform twist-averaged calculations for the $2 \times 2 \times 1$ and $4 \times 4 \times 1$ k-meshes. Only the convergence of the correlation part of the energy is shown for MP2 and CCSD, using 768 NOs. The energies are shown as the difference from the $4 \times 4 \times 1$ value for each method. The shaded region denotes the 1 kcal/mol area from the reference value. All energies in meV.

$4 \times 4 \times 1$ k-mesh at the MP2 level can thus be obtained as

$$E_{\text{MP2}} = E^{4\times4\times1}_{\text{MP2-699NOs}} + \Delta E^{1\times1\times1}_{\text{MP2-aVQZ–g}}. \tag{8.3}$$

It should be stressed that the aVQZ–g virtual orbital set still includes a basis set incompleteness and superposition error. A further correction $\Delta E^{1\times1\times1}_{\text{dMP2-PW}}$ is added, which is the difference of the direct MP2 (dMP2) Γ-point calculation using the full plane-wave virtual states (35076 states) and the dMP2 aVQZ–g calculation. Thus the converged MP2 results are obtained via the formula

$$E_{\text{MP2}} = E^{4\times4\times1}_{\text{MP2-699NOs}} + \Delta E^{1\times1\times1}_{\text{MP2-aVQZ–g}} + \Delta E^{1\times1\times1}_{\text{dMP2-PW}}. \tag{8.4}$$

Similarly, RPA calculations were performed with the VASP code, using PBE orbitals as a reference, a full $4 \times 4 \times 1$ k-mesh, and the aVQZ–g virtual orbital states with a Γ-point basis set correction using the full plane-wave virtual states. Consequently, the converged RPA correlation energy is computed as

$$E_{\text{RPA}} = E^{4\times4\times1}_{\text{RPA-aVQZ–g}} + \Delta E^{1\times1\times1}_{\text{RPA-PW}}. \tag{8.5}$$

TABLE 8.1: k-points in reciprocal coordinates with their respective weights corresponding to a $4 \times 4 \times 1$ k-mesh.

k_x	k_y	k_z	weight
0.00	0.00	0.00	1
0.25	0.00	0.00	2
0.50	0.00	0.00	1
0.00	0.25	0.00	2
0.25	0.25	0.00	2
0.50	0.25	0.00	2
−0.25	0.25	0.00	2
0.00	0.50	0.00	1
0.25	0.50	0.00	2
0.50	0.50	0.00	1

TABLE 8.2: Convergence of the CCSD(T) energy for the two adsorption barriers, the desorption energy, and the reaction energy with respect to the NOs used for the (T) correction ($\Delta E^{1\times1\times1}_{\text{CCSD(T)-NOs}}$). All contributions from Fig. 8.5 are included. All energies are in eV.

# of NOs	E_a^{ads}[H2]	E_a^{ads}[H2*]	E_a^{des}	E_{rxn}
123	0.75	0.80	2.73	1.98
187	0.74	0.79	2.66	1.92
251	0.70	0.75	2.62	1.91

Let us now turn to the discussion of the convergence of the MP2 and CCSD correlation energies with respect to the k-point sampling of the Brillouin zone via the twist-averaging technique. The CCSD correlation energy for the $4 \times 4 \times 1$ k-mesh is calculated as

$$E_{\text{CCSD}} = E^{4\times4\times1}_{\text{CCSD-699NOs}} + \Delta E^{1\times1\times1}_{\text{CCSD-1377NOs}} + \Delta E^{1\times1\times1}_{\text{dMP2-PW}}, \tag{8.6}$$

where $E^{4\times4\times1}_{\text{CCSD-699NOs}}$ is the twist-averaged finite-size corrected CCSD correlation energy using 699 virtual NOs, $\Delta E^{1\times1\times1}_{\text{CCSD-1275NOs}}$ is a basis set correction based on a Γ-point CCSD calculation using 1275 NOs, and $\Delta E^{1\times1\times1}_{\text{dMP2-PW}}$ is the CBS limit correction and is defined as

$$\Delta E^{1\times1\times1}_{\text{dMP2-PW}} = E^{1\times1\times1}_{\text{dMP2-PW}} - E^{1\times1\times1}_{\text{dMP2-1377NOs}}. \tag{8.7}$$

The convergence of PBE, HF, MP2, and CCSD with respect to the k-point sampling is shown in Fig. 8.4. It is safe to presume that the results are converged well within 1

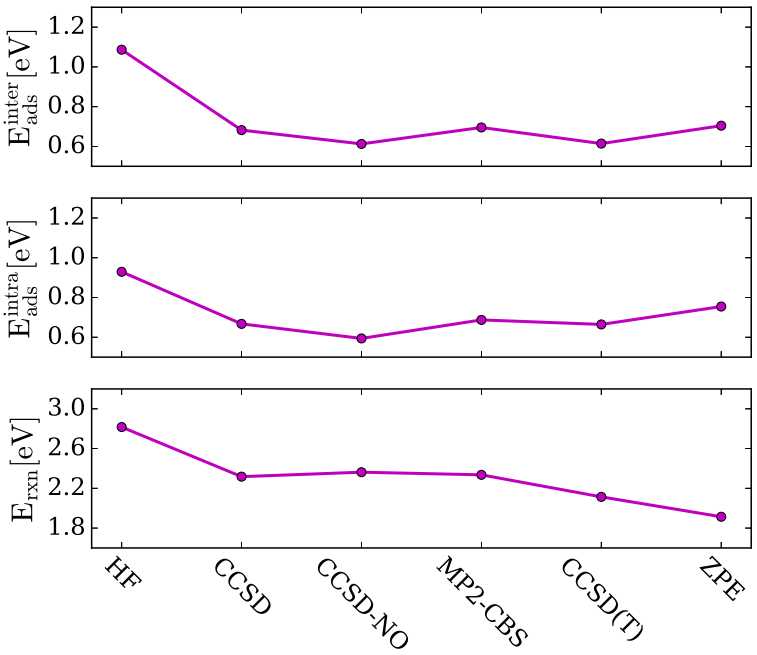

FIGURE 8.5: Different contributions to the CCSD(T) adsorption barriers and reaction energy. Starting from left to right we add the contributions to the adsorption barriers and the reaction energy. Thus, the ZPE contribution constitutes the final CCSD(T) number. Each contribution is defined in the text. We start from HF, add the CCSD correlation energy, two basis set corrections (one based on CCSD and one on the CBS MP2), the perturbative triples correction (T), and finally the ZPE. All energies given in eV.

kcal/mol (or 43 meV that is chemical accuracy) using a $4 \times 4 \times 1$ twist-averaged k-point sampling with MP2 and CCSD. PBE and HF energies can be obtained using a denser k-mesh, and we have checked convergence with respect to the $4 \times 4 \times 1$ mesh.

Finally the perturbative triples correction in CCSD is estimated by performing a Γ-point calculation with a few virtual NOs (251). The CCSD(T) barriers and reaction energy are obtained via the formula

$$E_{\text{CCSD(T)}} = E^{4\times4\times1}_{\text{CCSD-699NOs}} + \Delta E^{1\times1\times1}_{\text{CCSD-1377NOs}} + \Delta E^{1\times1\times1}_{\text{dMP2-PW}} + \Delta E^{1\times1\times1}_{\text{CCSD(T)-251NOs}}, \quad (8.8)$$

where $\Delta E^{1\times1\times1}_{\text{CCSD(T)-251NOs}}$ is defined as

$$\Delta E^{1\times1\times1}_{\text{CCSD(T)-251NOs}} = E^{1\times1\times1}_{\text{CCSD(T)-251NOs}} - E^{1\times1\times1}_{\text{CCSD-251NOs}}. \quad (8.9)$$

The different contributions to the CCSD(T) energies are shown in Fig. 8.5 for the two barriers and the reaction energy. These contributions are the HF energy and the CCSD(T) energy as defined in Eq. (8.8). The convergence of this final CCSD(T) energies with respect to the number of NOs used to evaluate $\Delta E^{1\times1\times1}_{\text{CCSD(T)-NOs}}$ is shown in Table 8.2.

8.2 Results and discussion

Figure 8.6 shows the calculated reaction energetics for H_2 on the (100) surface of Si at different levels of theory, together with the experimental estimates and the corresponding error depicted by the shaded area. The results are also summarized in Table. 8.3. First the reaction energy (E_{rxn}) is considered, shown in the top panel, and the discussion of the barrier heights will follow. The reaction energy is defined as $E_{rxn} = E_{initial} - E_{final}$, where the corresponding final and initial structures are shown in Fig. 8.1. The experimental estimate for the reaction energy is 1.9±0.3 eV [156]. The local-density approximation (LDA) constitutes the lowest rung of Perdew's Jacob's ladder of DFT methods. Reaction energies computed in the LDA are approximately 0.3 eV too small compared to the experimental estimate. The PBE functional is one of the most extensively used GGA functionals which represent the second rung of the Jacob's ladder and noticeably underestimates the reaction energy without any improvement compared to LDA. The meta-GGA functionals lie on the third rung and utilize the kinetic energy together with the electron density and its gradient. The strongly constrained and appropriately normed (SCAN) [131, 132] meta-GGA density functional significantly improves the reaction energy ($E_{rxn}^{SCAN} = 1.97$ eV), demonstrating its ability to describe diversely bonded molecules and materials such as the H–Si system accurately. Hybrid GGAs provide an improved description of covalent, hydrogen and ionic bonding by mixing non-local exact exchange with GGA exchange. B3LYP [10], PBE0 [170], and HSE06 [112] yield a reaction energy with a similar accuracy as SCAN. The good agreement between the hybrids and the SCAN functional confirms that meta-GGAs can yield reaction energies at the same level of accuracy yet at lower computational cost. As a method of the fifth rung of Perdew's Jacob's ladder the RPA is examined. The RPA correlation energy is fully non-local and seamlessly includes electronic screening as well as long-range dispersion interactions [171, 172]. The chemisorption energy in the RPA is, however, underestimated compared to hybrid-GGA and meta-GGA functionals, in agreement with a well known underestimation of binding energies [173]. Overall the predicted DFT results for the reaction energy are improving as one moves from lower to higher rungs with the exception of the RPA. The underestimated RPA reaction energy can be attributed to the neglect of post-RPA corrections and a lack of self-consistency.

Let us now switch from DFT to the wavefunction based hierarchy for treating electronic correlation. HF theory, approximating the many-electron wavefunction by a single Slater determinant, overestimates the reaction energy by as much as 0.7 eV compared to experiment. It should be noted that this is in contrast to atomization energies of molecules and cohesive energies of solids, which are usually underestimated by HF [104, 174].

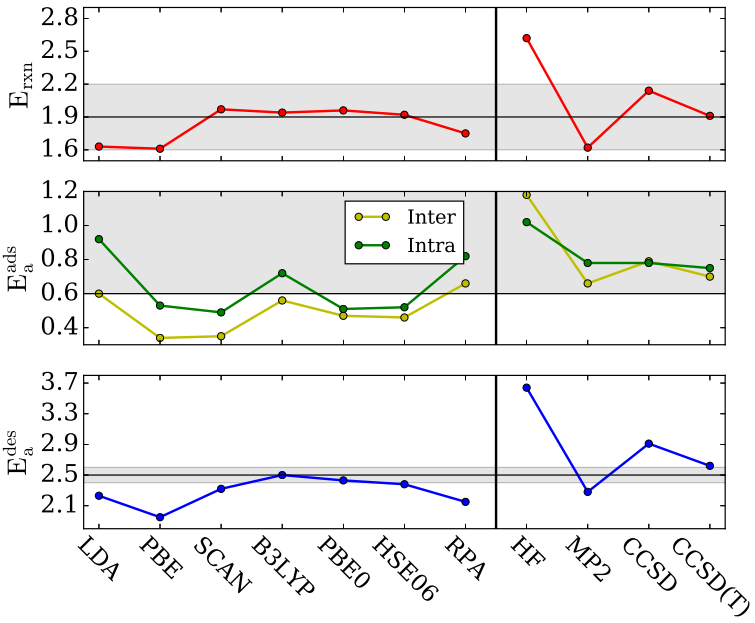

FIGURE 8.6: Reaction energetics for H_2 dissociation on the Si(001) surface calculated at different levels of theory. The calculated reaction energies (E_{rxn}) adsorption (E_a^{ads}) and desorption (E_a^{des}) barriers for H_2 dissociative adsorption on Si(100) surface. The black lines represent the experimental estimate while the shaded region the error. All energies given in eV.

Adding correlation effects at the level of MP2 theory over-corrects HF and yields a reaction energy of 1.62 eV, almost 0.3 eV smaller than the experimental estimate. this overcorrection of MP2 can be assigned to the small band gap of the Si surface. The more sophisticated CCSD theory overestimates the experimental reaction energy by 0.25 eV. Adding the perturbative triples correction (T) to CCSD yields a reaction energy that is very close to hybrid DFT results and the experimental estimate. This demonstrates the ability of the wavefunction based hierarchy to yield systematically improvable and chemically accurate chemisorption energies for molecules on periodic surfaces. However, at lower levels of theory, the DFT based methods exhibit a significantly better trade-off between accuracy and computational cost.

Given that experimental measurements for the chemisorption energy can be confirmed using accurate electronic structure theories, let us now discuss the activation barrier height for the dissociation, that is defined as $E_a^{ads} = E_{transition} - E_{initial}$. Establishing accurate estimates of barrier heights is more difficult compared to reaction energies for theory as well as experiment. Transition states often exhibit strong electronic correlation effects that can only be treated accurately using higher levels of theory. Furthermore experimental measurements of adsorption barriers are usually lower bounds and do not allow to determine directly whether the reaction proceeds via the H2 or H2* mechanism.

Adsorption barriers for both pathways are depicted in the middle panel of Fig. 8.6, alongside the experimental lower bound of 0.6 eV [155]. LDA yields a barrier of 0.6 eV and 0.92 eV for the H2 and H2* pathway, respectively. The difference in the barriers between the two pathways is considerable. Noteworthy, LDA does not vastly underestimate the activation energies, but yields rather adequately high barriers for both mechanisms. PBE underestimates the reaction barriers and yields in agreement with LDA a larger barrier for the H2* pathway. We observe the same trend for the SCAN functional. Although the description of the reaction energy is much improved, SCAN fails to ameliorate the errors in the reaction barriers predicted by GGA, yielding a too low barrier for the H2 path and the same difference between the barriers of the two pathways. Interestingly, LDA predicts much larger activation energies than GGA, challenging the trend LDA<GGA observed for adsorption barriers of molecular reactions [175]. Similar results, however, have been reported for activation energies of gas-phase reactions [176]. Hybrid functionals mix exact exchange with commonly-used density functionals and partly cancel the spurious self-interaction error. In the case of H_2 on Si(100) hybrid functionals do improve the description of the reaction barrier. B3LYP yields a barrier height of 0.56 eV for the H2 path, whereas PBE0 and HSE06 yield barriers of 0.47 eV and 0.46 eV respectively. For the H2* mechanism B3LYP predicts a barrier 0.16 eV higher than the H2 one, whereas PBE0 and HSE06 yield barriers only 0.04 and 0.06 eV higher than the H2 pathway, respectively. The RPA yields significantly higher barriers compared to PBE when combined with exact exchange computed with PBE orbitals. It is noted, however, that the H2 path is still favored by RPA with a barrier of 0.66 eV compared to 0.82 eV of the H2* path. The results discussed above illustrate convincingly a lack of systematic improvability in the obtained estimates of barrier heights as one moves from lower to higher levels of approximate DFT based methods. Furthermore, errors in activation energies may vary significantly with the employed density functional. Therefore reliable predictions for the barrier height and the relative stability of the considered transition states are not possible. Nevertheless, the considered system provides a realistic and insightful scenario to further develop and improve upon the computationally efficient DFT based methods.

Let us now turn to the discussion of wavefunction based *ab-initio* calculations for the barrier. HF theory yields barriers larger than 1 eV for both pathways. In contrast to DFT based findings, HF favors the H2* path over the H2 one by 0.16 eV. In order to better understand the difference between HF and DFT, we consider the different paths as a competition between stretching the H_2 molecule and flattening the Si dimers of the surface. In Fig. 8.1 the hydrogen bond in the H2 transition state is 0.89 Å, compared to 1.01 Å of the H2* one, whereas the dimers buckling angle is 27.2° for the former and 34.3° for the latter transition state. In order to see why HF favors the H2* path we

need to consider the energy cost between the buckled and symmetric configurations of the Si dimer reconstruction. This energy difference per dimer is 250–260 meV for LDA and GGA, in contrast to 544 meV for HF. The energy penalty for flattening the dimers can be identified as the main difference between HF and DFT methods, owing to a large extent on the metallic nature of the symmetric Si dimer configuration. MP2 theory reverses the preference of the two pathways. Furthermore, the MP2 adsorption barrier for the H2 transition state is 0.66 eV while for the H2* is 0.78 eV. Due to the smaller band gap of the H2 transition state MP2 overcorrects HF, hence it favors the lower band gap H2 reaction pathway. CCSD theory yields barriers for the two reaction mechanisms that are practically degenerate. Specifically, the H2 transition state barrier is 0.79 eV and the H2* 0.78 eV. In agreement with experiment the inclusion of perturbative triples, CCSD(T), yields activation barriers of 0.70 eV for the H2 transition and 0.75 eV for the H2* one, retaining the picture of two approximately degenerate barriers of CCSD to within chemical accuracy.

The picture emerging from the results discussed above is qualitatively different within the different methods that are examined. The two barriers are approximately degenerate using the more sophisticated CCSD and CCSD(T) theories, in contrast to LDA, PBE and SCAN functionals, where the H2 path is favored. Hybrid functionals remedy partly the self-interaction error and thus yield barriers that differ less than the GGA and LDA ones. An exception is B3LYP, where although the barriers are higher in energy, the H2 path is favored by 0.16 eV. The reason is that part of the exchange-correlation functional is based on a mixture of LDA and GGA rather than solely on GGA as in PBE0 and HSE06. Thus B3LYP contains part of the LDA errors and deficiencies, hence the higher barriers and the larger difference between the two pathways. Barriers for the two mechanisms based on the RPA also differ significantly. The discrepancy between the CCSD(T) barriers and the RPA ones can be associated with the use of PBE orbitals for the RPA calculations as opposed to the HF ones for CCSD(T). It is likely that a sizable fraction of the error exists already in the original DFT functional, leading to an overestimation of the H2 barrier. In order to get more insight into the disagreement of CC methods and DFT based methods, non-self-consistent calculations have been performed for the activation barriers of the two mechanisms at the level of DFT-PBE using HF orbitals. The results are shown in Table. 8.3. One can observe that when HF orbitals are employed for DFT-PBE calculations the H2 barrier is appreciably higher, whereas the H2* one remains almost the same. The difference between the two barriers is 0.04 eV in close agreement with the accurate CCSD(T) and hybrid DFT results. This is partly due to the cancellation of the density driven one-electron self-interaction error [177], and similar results have been obtained for simple molecular reaction barriers and adsorption energies [178, 179].

TABLE 8.3: Adsorption barriers for the two pathways, alongside desorption and reaction energies. Desorption energies correspond to the energetically lowest path, whereas reaction energies to the intra-dimer (H2*) geometry, since it is energetically the lowest configuration. ZPE corrections assumed for all calculations(identical for both pathways). All energies are reported in eV.

	E_a^{ads}[H2]	E_a^{ads}[H2*]	E_a^{des}	E_{rxn}
LDA	0.60	0.92	2.23	1.62
PBE	0.34	0.53	1.95	1.61
PBE@HF	0.46	0.50	2.13	1.76
SCAN	0.35	0.49	2.32	1.97
B3LYP	0.56	0.72	2.50	1.94
PBE0	0.47	0.51	2.43	1.96
HSE06	0.46	0.52	2.38	1.92
RPA	0.66	0.82	2.16	1.75
HF	1.18	1.02	3.79	2.62
MP2	0.66	0.78	2.28	1.62
CCSD	0.79	0.78	2.92	2.18
CCSD(T)	0.70	0.75	2.62	1.91
QMC [158]	(0.09)0.63	(0.05)0.75	(0.09)2.91	(0.05)2.20
Expt. [149, 155, 156]	> 0.6	> 0.6	(0.10)2.50	(0.30)1.90
ZPE [157]	+0.09	+0.09	−0.11	−0.20

Finally, the desorption mechanisms for the reaction is examined. The desorption barrier is defined as $E_a^{des} = E_{transition} - E_{final}$. QMC corrections using finite clusters [158] predict that none of the H2 or H2* mechanisms are compatible with temperature programmed desorption experiments [149], since they yield too high desorption barriers for both mechanisms. Using periodic CCSD(T), however, it is found that desorption barriers for the two mechanisms are very close and agree rather well with the experimental estimate of 2.5 ± 0.1 eV. Furthermore, CCSD(T) desorption energies are 2.62 and 2.67 eV for the H2 and H2* mechanisms. DFT-PBE predicts desorption energies of 1.95 and 2.14 eV, respectively, vastly misjudging the absolute magnitude, as well as the relative difference of the desorption barrier for the two mechanisms. The SCAN functional improves the PBE desorption barriers, however, only by ameliorating the description of the chemisorption energy and not of the adsorption barrier. Hybrid functional results are in satisfactory agreement with CSSD(T). Moreover, PBE0 and HSE06 estimated desorption energies are 2.43 and 2.38 eV for the H2 mechanism and 2.47 and 2.44 eV for the H2* one. It is stressed that the two desorption energies are not only significantly higher than the DFT-PBE ones but also not far from each other. B3LYP yields desorption energies of

2.50 and 2.66 eV for the H2 and H2* mechanisms respectively. Although the energies are close to the experimental estimate the overall picture for the reaction mechanism is significantly different than the CCSD(T) one. The H2 pathway is much preferred over the H2* one due to the mistreatment of the relative difference of the two adsorption barriers, stemming from the LDA part of the exchange-correlation functional. Finally the RPA desorption energies, although they represent a significant improvement over DFT-PBE, they still inherit shortcomings of the parent PBE density functional, by favoring the H2 adsorption channel.

8.3 Conclusion and Summary

A range of DFT and quantum chemical wavefunction based calculations were performed for the H2 and H2* adsorption/desorption mechanisms of H_2 on the Si(100) surface at low coverage. It is shown that periodic CCSD(T) calculations yield excellent agreement with experimental results for the adsorption barriers and the reaction energy. In contrast to previous calculations, we find similar activation energies for the H2 and H2* adsorption mechanisms. DFT-GGA and DFT-meta-GGA functionals over-stabilize the H2 adsorption mechanism due to incorrect ground state densities caused by self-interaction errors. It is argued that both a correct description of the H_2 molecule dissociation, as well as of the surface dimer reconstruction is essential for a precise interpretation of the reaction mechanisms. Hybrid functionals, like PBE0 and HSE06 slightly underestimate the adsorption barriers, however, they yield adequate results for the energetics of the reaction. It has been demonstrated that high level periodic wavefunction based methods have the potential to serve as accurate benchmark theories for predicting reaction energetics on periodic surfaces, which will ultimately help to further improve upon computationally more efficient yet less accurate methods.

Chapter 9

Summary and Conclusions

Surfaces and their interaction with molecules is a very broad field of research on its own. In order to achieve an accurate electronic structure description in these systems it is often necessary to go beyond DFT with local or semi-local approximations. The main goal of this thesis is to implement and apply many-body correlation techniques in surface science problems. Popular methods, such as MP2 and CC theory posses a high-order polynomial scaling of their computational cost with respect to the system size in their canonical implementations. In this work a canonical CC theory is developed in a plane-wave basis within the PAW framework.

In the first part of the thesis an introduction is presented. The electronic Hamiltonian within the BO approximation is introduced in Chapters 1 and 2. Methods for obtaining approximate solutions are presented in Chapter 3. DFT is discussed before presenting wavefunction-based methods. The fundamentals of HF theory as well as of correlation techniques, such as CI, MP2, and CC are then presented. In Chapter 4 the PAW method is discussed. An expression for the DFT and HF energies, as well as for the two-electron repulsion integrals is given.

The second part of the thesis presents a robust and computationally feasible periodic CC scheme. In Chapter 5 a Γ-point periodic canonical implementation of the CCSD and (T) equations is given. First, a low-rank representation of the Coulomb integrals via the Coulomb vertex is discussed. An approximation to the Coulomb vertex via a singular value decomposition is then used to approximate the Coulomb integrals. A low-rank factorization of the Coulomb vertex is presented, allowing for a reduction of the computational cost of the most expensive terms in the CCSD equations. The CCSD and (T) equations are implemented using the Cyclops Tensor Framework, a massively parallel tensor contraction library. In Chapter 6 an efficient truncation of the vast number of plane-wave virtual orbitals is considered. A compact representation

of the virtual orbitals is found by mapping a set of pseudized atom-centered Gaussian functions onto a plane-wave representation. The Fock matrix is then rediagonalized by this set of orbitals, resulting in a canonical set of one-particle states, with much fewer number of orbitals. Last, a finite-size correction scheme is presented, that accelerates the thermodynamic limit convergence, without the need to increase the supercell size. Water adsorption on *h*-BN serves as a benchmark system for testing the approximations.

The third and last part of the thesis presents applications of the CC scheme, studying surface interactions with molecules. In Chapter 7 physisorption of water on two-dimensional and quasi two-dimensional surfaces is studied with CC theory. First, a comprehensive comparison between different electronic structure methods including wavefunction-based theories and a small selection of density-functionals is presented for the prediction of the adsorption energy of a single water molecule on the (001) LiH surface. Quantum chemical methods are systematically improvable, hence yielding increasingly accurate adsorption energies as one moves up the hierarchy to higher orders of theory. Inclusion of triple excitations to CCSD theory give the best agreement with the DMC results. A good agreement between periodic canonical and local implementations utilizing explicit correlation techniques for improved basis set convergence is also found. All these demonstrate that quantum chemical approaches are becoming a robust and reliable tool for molecule–surface electronic structure calculations. Water physisorption on hexagonal BN and graphene is studied next. The adsorption energy of water on BN is obtained using periodic CCSD(T) theory. CCSD(T), DMC, and RPA with single excitations agree well on the interaction strength of water monomer on BN. Comparison with vdW corrected density-functionals shows a slight underestimation of the adsorption energy by the former. Graphene interaction with water is studied next. Results based on CCSD(T) theory indicate that the strength of the interaction is weaker than previously reported in other studies. Results are again in good agreement with DMC studies.

In Chapter 8 a CC study of the reaction energetics of hydrogen dissociation on Si is presented. A range of DFT and quantum chemical wavefunction-based calculations are employed for two different adsorption/desorption mechanisms of H2 on the Si(100) surface at low coverage. It is shown that periodic CCSD(T) calculations yield excellent agreement with experimental results for the adsorption barriers and the reaction energy. In contrast to previous calculations, similar activation energies for the two adsorption mechanisms are found.

This thesis has demonstrated that high-level periodic wavefunction-based methods have the potential to serve as accurate benchmark theories for predicting reaction energetics on periodic surfaces, which will ultimately help to further improve upon computationally more efficient yet less accurate methods.

Appendix A

Slater–Condon Rules

In order to proceed with wavefunction-based theories, one needs the matrix elements of the Hamiltonian

$$\mathcal{H}_{IJ} = \langle \Phi_I | \hat{\mathcal{H}} | \Phi_J \rangle \ . \tag{A.1}$$

The Slater-Condon rules allow one to calculate these matrix elements for any pair of orthonormal Slater determinants Φ_I and Φ_J. Assuming a reference determinant Φ (usually the HF one), we can describe all other determinants by specifying the difference in spin-orbitals between the two determinants. We can define excited Slater determinants as follows. Singly excited determinants Φ_i^a, where spin-orbital ψ_i is replaced by ψ_a, double excited determinants Φ_{ij}^{ab}, where spin-orbitals ψ_i and ψ_j is replaced by ψ_a and ψ_b, and so forth.

We can split the Hamiltonian into one-body and two-body parts

$$\begin{aligned} \hat{\mathcal{H}} =& \hat{H}_1 + \hat{H}_2 \ , \\ \hat{H}_1 =& \sum_i \hat{h}(i) \ , \\ \hat{H}_2 =& \sum_{i>j} \frac{1}{r_{ij}} \ . \end{aligned} \tag{A.2}$$

The Slater–Condon rules for the one-body part $\hat{H}_1$ read

$$\begin{aligned} \langle \Phi | \hat{H}_1 | \Phi \rangle =& \sum_i \langle \psi_i | \hat{h} | \psi_i \rangle \ , \\ \langle \Phi_i^a | \hat{H}_1 | \Phi \rangle =& \langle \psi_a | \hat{h} | \psi_i \rangle \ , \\ \langle \Phi_{ij}^{ab} | \hat{H}_1 | \Phi \rangle =& 0 \ . \end{aligned} \tag{A.3}$$

We note that matrix elements between the reference and higher excited determinants vanish as well.

The matrix elements of $\hat{H}_2$ read

$$\begin{aligned}
\langle\Phi|\hat{H}_2|\Phi\rangle =& \frac{1}{2}\sum_{ij}\left[\langle\psi_i\psi_j|\frac{1}{r_{12}}|\psi_i\psi_j\rangle - \langle\psi_i\psi_j|\frac{1}{r_{12}}|\psi_j\psi_i\rangle\right] , \\
\langle\Phi_i^a|\hat{H}_2|\Phi\rangle =& \sum_{j}\left[\langle\psi_a\psi_j|\frac{1}{r_{12}}|\psi_i\psi_j\rangle - \langle\psi_a\psi_j|\frac{1}{r_{12}}|\psi_j\psi_i\rangle\right] , \\
\langle\Phi_{ij}^{ab}|\hat{H}_2|\Phi\rangle =& \langle\psi_a\psi_b|\frac{1}{r_{12}}|\psi_i\psi_j\rangle - \langle\psi_a\psi_b|\frac{1}{r_{12}}|\psi_j\psi_i\rangle , \\
\langle\Phi_{ijk}^{abc}|\hat{H}_2|\Phi\rangle =& 0 .
\end{aligned} \tag{A.4}$$

Again matrix elements between Φ and higher excited Slater determinants vanish as well. Finally, we stress that summations over i and j run over all occupied spin-orbitals in Φ.

Appendix B

Rayleigh–Schrödinger perturbation theory

In Rayleigh–Schrödinger perturbation theory we are looking solutions to the time-independent Schrödinger equation

$$\hat{\mathcal{H}}\Psi_n = E_n\Psi_n \ , \tag{B.1}$$

where $\hat{\mathcal{H}}$ is the Hamiltonian and Ψ_n and E_n represent the exact eigenfunctions and eigenvalues of the Hamiltonian. The idea is to split the Hamiltonian into two parts

$$\hat{\mathcal{H}} = \hat{\mathcal{H}}_0 + \lambda\hat{\mathcal{V}} \ , \tag{B.2}$$

where $\hat{\mathcal{H}}_0$ is the uperturbed Hamiltonian and $\hat{\mathcal{V}}$ is the perturbation. λ is a formal parameter that later will be set to one. The ground-state wavefunction Ψ and energy E can be expanded as Taylor series of the parameter λ

$$\begin{aligned} \Psi(\lambda) =& \Psi^{(0)} + \lambda\Psi^{(1)} + \lambda^2\Psi^{(2)} + \dots \ , \\ E(\lambda) =& E^{(0)} + \lambda E^{(1)} + \lambda^2 E^{(2)} + \dots \ , \end{aligned} \tag{B.3}$$

where

$$\begin{aligned} \Psi^{(k)} =& \frac{1}{k!}\left(\frac{\partial^k\Psi}{\partial\lambda^k}\right)_{\lambda=0} \ , \\ E^{(k)} =& \frac{1}{k!}\left(\frac{\partial^k E}{\partial\lambda^k}\right)_{\lambda=0} \ . \end{aligned} \tag{B.4}$$

Assuming that $\langle\Psi^{(0)}|\Psi^{(k)}\rangle = \delta_{k0}$ and if $\Psi^{(0)}$ is normalized, then we have intermediate normalization, i.e.,

$$\langle\Psi^{(0)}|\Psi\rangle = 1 \ . \tag{B.5}$$

Note that Ψ is not normalized. If we introduce the ansatz of Eq. (B.3) into the Schrödinger equation using the Hamiltonian of Eq. (B.2) and equate the coefficients of same powers of λ we arrive at a hierarchy of equations

$$\begin{aligned}
&\left[\hat{\mathcal{H}}_0 - E^{(0)}\right]|\Psi^{(0)}\rangle = 0 && \text{(B.6)}\\
&\left[\hat{\mathcal{H}}_0 - E^{(0)}\right]|\Psi^{(1)}\rangle + \left[\hat{\mathcal{V}} - E^{(1)}\right]|\Psi^{(0)}\rangle = 0 && \text{(B.7)}\\
&\left[\hat{\mathcal{H}}_0 - E^{(0)}\right]|\Psi^{(2)}\rangle + \left[\hat{\mathcal{V}} - E^{(1)}\right]|\Psi^{(1)}\rangle - E^{(2)}|\Psi^{(0)}\rangle = 0 && \text{(B.8)}\\
&\vdots
\end{aligned}$$

Multiplying each equation from the left with $\langle\Psi^{(0)}|$ and using the orthogonality conditions yields a series of equations for the energies

$$\begin{aligned}
E^{(0)} =& \langle\Psi^{(0)}|\hat{\mathcal{H}}|\Psi^{(0)}\rangle && \text{(B.9)}\\
E^{(1)} =& \langle\Psi^{(0)}|\hat{\mathcal{V}}|\Psi^{(0)}\rangle && \text{(B.10)}\\
E^{(2)} =& \langle\Psi^{(0)}|\hat{\mathcal{V}}|\Psi^{(1)}\rangle && \text{(B.11)}\\
&\vdots
\end{aligned}$$

In order on to determine the second order correction to the energy $E^{(2)}$, one has to determine the first order correction to the wavefunction $\Psi^{(1)}$. Assuming we have an orthonormal set of solutions $\left\{\Psi_n^{(0)}\right\}$ for the zeroth order Hamiltonian $\hat{\mathcal{H}}_0$, one can expand the first order wavefunction as

$$\Psi^{(1)} = \sum_m C_m^{(1)}\Psi_m^{(0)} \ , \tag{B.12}$$

excluding the ground state $\Psi^{(0)}$. The coefficients $C_l^{(1)}$ can be obtained by inserting the ansatz of Eq.(B.12) into Eq. (B.7) and left multiplying with $\langle\Psi_l^{(0)}|$, which yields

$$\sum_m C_m^{(1)}\langle\Psi_l^{(0)}|\hat{\mathcal{H}}_0 - E^{(0)}|\Psi_m^{(0)}\rangle + \sum_m C_m^{(1)}\langle\Psi_l^{(0)}|\hat{\mathcal{V}} - E^{(1)}|\Psi^{(0)}\rangle = 0 \ , \tag{B.13}$$

and therefore

$$C_l^{(1)} = \frac{\langle\Psi_l^{(0)}|\hat{\mathcal{V}}|\Psi^{(0)}\rangle}{E^{(0)} - E_l^{(0)}} \ . \tag{B.14}$$

Appendix C

Closed-shell CCSD equations

Part of the C++ code implementing the closed CCSD equations (3.66), (3.67) and (3.68) using the CTF.

`T["tuvw"]` : Generic fourth rank tensor T^{tu}_{vw}

`R["tuxy"] = T["tuvw"] * S["vwxy"]` : Tensor contraction $R^{tu}_{xy} = \sum_{vw} T^{tu}_{vw} S^{vw}_{xy}$

`a b c d` : Virtual orbital indices

`i j k l` : occupied orbital indices

`GammaGia["Gia"]` : Coulomb vertex Γ^{aG}_{i}

`Tabij["abij"]` : Doubles amplitudes T^{ab}_{ij}

`Vabij["abij"]` : Two electron integrals V^{ab}_{ij}

`Rabij["abij"]` : Doubles amplitudes residua R^{ab}_{ij}

```
//*********************************************************
//************  T2 amplitude equations  *****************
//*********************************************************

// Build Xabij
```

```
Xabij["abij"]  = Tabij["abij"];
Xabij["abij"] += Tai["ai"] * Tai["bj"];

// Build Kac
Kac["ac"]  = (-2.0) * Vijab["klcd"] * Xabij["adkl"];
Kac["ac"] += ( 1.0) * Vijab["kldc"] * Xabij["adkl"];

// Build Lac
Lac["ac"]  = Kac["ac"];
Lac["ac"] += ( 2.0) * conjTransposeGammaGab["Gac"] * GammaGia["Gkd"]
             * Tai["dk"];
Lac["ac"] += (-1.0) * conjTransposeGammaGab["Gad"] * GammaGia["Gkc"]
             * Tai["dk"];

// Build Kki
Kki["ki"]  = ( 2.0) * Vijab["klcd"] * Xabij["cdil"];
Kki["ki"] += (-1.0) * Vijab["kldc"] * Xabij["cdil"];

// Build Lki
Lki["ki"]  = ( 1.0) * Kki   ["ki"];
Lki["ki"] += ( 2.0) * Vijka["klic"] * Tai["cl"];
Lki["ki"] += (-1.0) * Vijka["lkic"] * Tai["cl"];

// Build Xakic
Xakic["akic"]  = ( 1.0) * conjTransposeGammaGai["Gai"] * GammaGia["Gkc"];
Xakic["akic"] += (-1.0) * conjTransposeGammaGij["Gli"] * Tai["al"]
                 * GammaGia["Gkc"];
Xakic["akic"] += ( 1.0) * conjTransposeGammaGab["Gad"] * Tai["di"]
                 * GammaGia["Gkc"];
Xakic["akic"] += (-0.5) * conjTransposeGammaGia["Gld"] * Tabij["dail"]
                 * GammaGia["Gkc"];
Xakic["akic"] += (-1.0) * conjTransposeGammaGia["Gld"] * Tai["di"]
                 * Tai["al"] * GammaGia["Gkc"];
Xakic["akic"] += ( 1.0) * Vijab["lkdc"] * Tabij["adil"];
Xakic["akic"] += (-0.5) * Vijab["lkcd"] * Tabij["adil"];

// Build Xakci
Xakci["akci"]  = ( 1.0) * conjTransposeGammaGab["Gac"] * GammaGij["Gki"];
Xakci["akci"] += (-1.0) * conjTransposeGammaGia["Glc"] * Tai["al"]
```

```
                * GammaGij["Gki"];
Xakci["akci"] += ( 1.0) * conjTransposeGammaGab["Gac"] * GammaGia["Gkd"]
                * Tai["di"];
Xakci["akci"] += (-1.0) * conjTransposeGammaGia["Glc"] * Tai["al"]
                * GammaGia["Gkd"] * Tai["di"];
Xakci["akci"] += (-0.5) * Vijab["lkcd"] * Tabij["dail"];

// Build Xklij intermediate
Xklij["klij"]  = Vijkl["klij"];
Xklij["klij"] += Vijka["klic"] * Tai["cj"];
Xklij["klij"] += Vijka["lkjc"] * Tai["ci"];
Xklij["klij"]  = Vijab["klcd"] * Xabij["cdij"];

//////////////////////////////////////

// Contract Lac with T2 Amplitudes
Rabij["abij"] += ( 1.0) * Lac["ac"] * Tabij["cbij"];

// Contract Lki with T2 Amplitudes
Rabij["abij"] += (-1.0) * Lki["ki"] * Tabij["abkj"];

// Contract Coulomb integrals with T2 amplitudes
Rabij["abij"] += ( 1.0) * conjTransposeGammaGai["Gai"] * GammaGab["Gbc"]
                * Tai["cj"];
Rabij["abij"] += (-1.0) * conjTransposeGammaGij["Gki"] * Tai["ak"]
                * GammaGab["Gbc"] * Tai["cj"];

Rabij["abij"] += (-1.0) * Vaijk["akij"] * Tai["bk"];
Rabij["abij"] += (-1.0) * Tai["bk"] * Vaijb["akic"] * Tai["cj"];

// Contract and Xakic intermediates with T2 amplitudes Tabij
Rabij["abij"] += ( 2.0) * Xakic["akic"] * Tabij["cbkj"];
Rabij["abij"] += (-1.0) * Xakic["akic"] * Tabij["bckj"];

// Contract and Xakci intermediates with T2 amplitudes Tabij
Rabij["abij"] += (-1.0) * Xakci["akci"] * Tabij["cbkj"];
Rabij["abij"] += (-1.0) * Xakci["bkci"] * Tabij["ackj"];

// Symmetrize Rabij by applying permutation operator
```

```
Rabij["abij"] += Rabij["baji"];

// Add Vabij to Rabij (MP2 term)
Rabij["abij"] += Vabij["abij"];

// Contract Xklij with T2+T1*T1 Amplitudes via Xabij
Rabij["abij"] +=  Xklij["klij"] * Xabij["abkl"];
// Last term contracted only with the doubles
// The singles term is computed in the slicing
Rabij["abij"] +=  Xklij["klij"] * Tabij["abkl"];

// Tcdij * (Vabcd - Vakcd * Tbk - Vkbcd * Tak + Vklcd * Tal * Tbk)
Rabij["abij"]  = ( 1.0) * Xabij["cdij"] * PiaR["cR"]
                        * PiaR["dS"] * conjLambdaGR["GR"] * LambdaGR["GS"]
                        * PiaR["bS"] * PiaR["aR"];
Rabij["abij"]  = (-1.0) * Xabij["cdij"] * PiaR["cR"]
                        * PiaR["dS"] * conjLambdaGR["GR"] * LambdaGR["GS"]
                        * PijR["kS"] * Tai["bk"] * PiaR["aR"];
Rabij["abij"]  = (-1.0) * Xabij["cdij"] * PiaR["cR"]
                        * PiaR["dS"] * conjLambdaGR["GR"] * LambdaGR["GS"]
                        * PiaR["bS"] * PijR["kR"] * Tai["ak"];
Rabij["abij"]  = ( 1.0) * Xabij["cdij"] * PiaR["cR"]
                        * PiaR["dS"] * conjLambdaGR["GR"] * LambdaGR["GS"]
                        * PijR["kS"] * Tai["bk"] * PijR["kR"] * Tai["ak"];

// Tcdij * (Vabcd - Vakcd * Tbk - Vkbcd * Tak + Vklcd * Tal * Tbk)
Vabcd["abcd"]  = ( 1.0) * GammaGab["Gac"] * conjTransposeGammaGbd["Gbd"];
Vabcd["abcd"] += (-1.0) * GammaGia["Gkc"] * Tai["ak"]
                        * conjTransposeGammaGbd["Gbd"];
Vabcd["abcd"] += (-1.0) * GammaGab["Gac"] * conjTransposeGammaGia["Gkd"]
                        * (*Tai)["bk"];
Vabcd["abcd"] += ( 1.0) * GammaGia["Gkc"] * Tai["ak"]
                        * conjTransposeGammaGia["Gkd"] * (*Tai)["bk"];
Rabij["abij"] += ( 1.0) * Vabcd["abcd"] * Xabij["cdij"];

// Tcdij * (Vabcd - Vakcd * Tbk - Vkbcd * Tak + Vklcd * Tal * Tbk)
Rabij["abij"] += ( 1.0) * Xabij["cdij"] * PiaR["cR"]
                        * PiaR["dS"] * conjLambdaGR["GR"] * LambdaGR["GS"]
                        * PiaR["bS"] * PiaR["aR"];
```

```
Rabij["abij"] += (-1.0) * Xabij["cdij"] * PiaR["cR"]
                        * PiaR["dS"] * conjLambdaGR["GR"] * LambdaGR["GS"]
                        * PijR["kS"] * Tai["bk"] * PiaR["aR"];
Rabij["abij"] += (-1.0) * Xabij["cdij"] * PiaR["cR"]
                        * PiaR["dS"] * conjLambdaGR["GR"] * LambdaGR["GS"]
                        * PiaR["bS"] * PijR["kR"] * Tai["ak"];
Rabij["abij"] += ( 1.0) * Xabij["cdij"] * PiaR["cR"]
                        * PiaR["dS"] * conjLambdaGR["GR"] * LambdaGR["GS"]
                        * PijR["kS"] * Tai["bk"] * PijR["kR"] * Tai["ak"];


//*********************************************************
//************  T1 amplitude equations  *****************
//*********************************************************

// Build Kck
Kck["ck"]  = ( 2.0) * Vijab["klcd"] * Tai["dl"];
Kck["ck"] += (-1.0) * Vijab["kldc"] * Tai["dl"];

// Contract all the terms to get T1 amplitudes
Rai["ai"] += ( 1.0) * Kac["ac"] * Tai["ci"];
Rai["ai"] += (-1.0) * Kki["ki"] * Tai["ak"];
Rai["ai"] += ( 2.0) * Kck["ck"] * Tabij["caki"];
Rai["ai"] += (-1.0) * Kck["ck"] * Tabij["caik"];
Rai["ai"] += ( 1.0) * Tai["ak"] * Kck["ck"] * Tai["ci"];
Rai["ai"] += ( 2.0) * Vaijb["akic"] * Tai["ck"];
Rai["ai"] += (-1.0) * Vaibj["akci"] * Tai["ck"];
Rai["ai"] += ( 2.0) * conjTransposeGammaGab["Gac"] * GammaGia["Gkd"]
             * Xabij["cdik"];
Rai["ai"] += (-1.0) * conjTransposeGammaGab["Gad"] * GammaGia["Gkc"]
             * Xabij["cdik"];
Rai["ai"] += (-2.0) * Vijka["klic"] * Xabij["ackl"];
Rai["ai"] += ( 1.0) * Vijka["lkic"] * Xabij["ackl"];
```

Bibliography

[1] M. Born and R. Oppenheimer, Annalen der Physik **389**, 457.

[2] W. Kohn, Rev. Mod. Phys. **71**, 1253 (1999).

[3] P. Hohenberg and W. Kohn, Phys. Rev. **136**, B864 (1964).

[4] W. Kohn and L. J. Sham, Phys. Rev. **140**, A1133 (1965).

[5] D. Ceperley, Phys. Rev. B **18**, 3126 (1978).

[6] D. M. Ceperley and B. J. Alder, Phys. Rev. Lett. **45**, 566 (1980).

[7] J. P. Perdew, K. Burke, and M. Ernzerhof, Phys. Rev. Lett. **77**, 3865 (1996).

[8] J. P. Perdew and K. Schmidt, AIP Conference Proceedings **577**, 1 (2001).

[9] T. Van Voorhis and G. E. Scuseria, The Journal of Chemical Physics **109**, 400 (1998).

[10] A. D. Becke, The Journal of Chemical Physics **98**, 5648 (1993).

[11] U. von Barth and L. Hedin, Journal of Physics C: Solid State Physics **5**, 1629 (1972).

[12] O. Gunnarsson and B. I. Lundqvist, Phys. Rev. B **13**, 4274 (1976).

[13] M. Stöhr, T. Van Voorhis, and A. Tkatchenko, Chem. Soc. Rev. **48**, 4118 (2019).

[14] D. R. Hartree, Mathematical Proceedings of the Cambridge Philosophical Society **24**, 89110 (1928).

[15] V. Fock, Zeitschrift für Physik **61**, 126 (1930).

[16] J. C. Slater, Phys. Rev. **35**, 210 (1930).

[17] A. Szabó and N. Ostlund, *Modern Quantum Chemistry: Introduction to Advanced Electronic Structure Theory* (Dover Publications, New York, 1996).

[18] T. Helgaker, P. Jørgensen, and J. Olsen, *Molecular Electronic-Structure Theory* (Wiley, 2000).

[19] T. Kato, Communications on Pure and Applied Mathematics **10**, 151.

[20] C. Hättig, W. Klopper, A. Köhn, and D. P. Tew, Chemical Reviews **112**, 4 (2012).

[21] D. P. Tew, W. Klopper, and T. Helgaker, Journal of Computational Chemistry **28**, 1307 (2007).

[22] E. Schrödinger, Annalen der Physik **385**, 437 (1926).

[23] C. Møller and M. S. Plesset, Phys. Rev. **46**, 618 (1934).

[24] M. Head-Gordon, J. A. Pople, and M. J. Frisch, Chemical Physics Letters **153**, 503 (1988).

[25] J. Čížek, The Journal of Chemical Physics **45**, 4256 (1966).

[26] J. Paldus, J. Čížek, and I. Shavitt, Phys. Rev. A **5**, 50 (1972).

[27] R. J. Bartlett and M. Musiał, Rev. Mod. Phys. **79**, 291 (2007).

[28] P. Pulay, Chemical Physics Letters **73**, 393 (1980).

[29] S. Hirata, I. Grabowski, M. Tobita, and R. J. Bartlett, Chemical Physics Letters **345**, 475 (2001).

[30] K. Raghavachari, G. W. Trucks, J. A. Pople, and M. Head-Gordon, Chemical Physics Letters **157**, 479 (1989).

[31] P. Piecuch, S. A. Kucharski, K. Kowalski, and M. Musia, Computer Physics Communications **149**, 71 (2002).

[32] V. Heine (Academic Press, 1970) pp. 1 – 36.

[33] P. Schwerdtfeger, ChemPhysChem **12**, 3143 (2011).

[34] P. E. Blöchl, Phys. Rev. B **50**, 17953 (1994).

[35] D. Vanderbilt, Phys. Rev. B **41**, 7892 (1990).

[36] G. Kresse and D. Joubert, Phys. Rev. B **59**, 1758 (1999).

[37] J. Paier, R. Hirschl, M. Marsman, and G. Kresse, The Journal of Chemical Physics **122**, 234102 (2005).

[38] M. Marsman, A. Grüneis, J. Paier, and G. Kresse, The Journal of Chemical Physics **130**, 184103 (2009).

[39] J. Harl, *The linear response function in density functional theory*, Ph.D. thesis, University of Vienna (2008).

[40] N. H. F. Beebe and J. Linderberg, International Journal of Quantum Chemistry **12**, 683 (1977).

[41] I. Røeggen and E. Wislff-Nilssen, Chemical Physics Letters **132**, 154 (1986).

[42] H. Koch, A. Sànchez de Merás, and T. B. Pedersen, The Journal of Chemical Physics **118**, 9481 (2003).

[43] B. I. Dunlap, J. W. D. Connolly, and J. R. Sabin, The Journal of Chemical Physics **71**, 4993 (1979).

[44] M. Feyereisen, G. Fitzgerald, and A. Komornicki, Chemical Physics Letters **208**, 359 (1993).

[45] O. Vahtras, J. Almlöf, and M. Feyereisen, Chemical Physics Letters **213**, 514 (1993).

[46] R. Sundararaman and T. A. Arias, Phys. Rev. B **87**, 165122 (2013).

[47] F. L. Hitchcock, Journal of Mathematics and Physics **6**, 164 (1927).

[48] T. Kolda and B. Bader, SIAM Review **51**, 455 (2009).

[49] L. Karlsson, D. Kressner, and A. Uschmajew, Parallel Computing **57**, 222 (2016).

[50] E. H. Moore, Bull. Amer. Math. Soc. **26**, 385 (1920).

[51] R. Penrose and J. A. Todd, Mathematical Proceedings of the Cambridge Philosophical Society **51**, 406 (1955).

[52] E. G. Hohenstein, R. M. Parrish, and T. J. Martìnez, The Journal of Chemical Physics **137**, 044103 (2012).

[53] R. M. Parrish, E. G. Hohenstein, T. J. Martìnez, and C. D. Sherrill, The Journal of Chemical Physics **137**, 224106 (2012).

[54] E. G. Hohenstein, R. M. Parrish, C. D. Sherrill, and T. J. Martìnez, The Journal of Chemical Physics **137**, 221101 (2012).

[55] R. M. Parrish, E. G. Hohenstein, T. J. Martìnez, and C. D. Sherrill, The Journal of Chemical Physics **138**, 194107 (2013).

[56] S. Kindermann and C. Navasca, arXiv preprint arXiv:1109.3832 (2011).

[57] A. Cichocki and R. Zdunek, in *Advances in Neural NetworksISNN 2007* (Springer, 2007) pp. 793–802.

[58] N. Li, S. Kindermann, and C. Navasca, arXiv:1109.3831 [math] (2011), arXiv: 1109.3831.

[59] R. M. Parrish, C. D. Sherrill, E. G. Hohenstein, S. I. L. Kokkila, and T. J. Martínez, The Journal of Chemical Physics **140**, 181102 (2014).

[60] E. Solomonik, D. Matthews, J. R. Hammond, J. F. Stanton, and J. Demmel, Journal of Parallel and Distributed Computing **74**, 3176 (2014).

[61] D. Kats and F. R. Manby, The Journal of Chemical Physics **139**, 021102 (2013).

[62] D. Kats, The Journal of Chemical Physics **141**, 061101 (2014).

[63] D. Kats, D. Kreplin, H.-J. Werner, and F. R. Manby, The Journal of Chemical Physics **142**, 064111 (2015).

[64] D. Kats, The Journal of Chemical Physics **144**, 044102 (2016).

[65] Y. S. Al-Hamdani, M. Rossi, D. Alfè, T. Tsatsoulis, B. Ramberger, J. G. Brandenburg, A. Zen, G. Kresse, A. Grüneis, A. Tkatchenko, and A. Michaelides, J. Chem. Phys. **147**, 044710 (2017).

[66] T. H. Dunning, The Journal of Chemical Physics **90**, 1007 (1989).

[67] D. Feller, Journal of Computational Chemistry **17**, 1571 (1996).

[68] G. H. Booth, T. Tsatsoulis, G. K.-L. Chan, and A. Grüneis, The Journal of Chemical Physics **145**, 084111 (2016).

[69] J. Harl and G. Kresse, Phys. Rev. B **77**, 045136 (2008).

[70] A. Grüneis, G. H. Booth, M. Marsman, J. Spencer, A. Alavi, and G. Kresse, Journal of Chemical Theory and Computation **7**, 2780 (2011).

[71] A. Grüneis, J. J. Shepherd, A. Alavi, D. P. Tew, and G. H. Booth, The Journal of Chemical Physics **139**, 084112 (2013).

[72] N. B. Balabanov and K. A. Peterson, The Journal of Chemical Physics **123**, 064107 (2005).

[73] R. Dovesi, R. Orlando, A. Erba, C. M. Zicovich-Wilson, B. Civalleri, S. Casassa, L. Maschio, M. Ferrabone, M. De La Pierre, P. D'Arco, Y. Noël, M. Causà, M. Rérat, and B. Kirtman, International Journal of Quantum Chemistry **114**, 1287 (2014).

[74] C. Pisani, M. Schütz, S. Casassa, D. Usvyat, L. Maschio, M. Lorenz, and A. Erba, Phys. Chem. Chem. Phys. **14**, 7615 (2012).

[75] L. Maschio, D. Usvyat, M. Schütz, and B. Civalleri, The Journal of Chemical Physics **132**, 134706 (2010).

[76] M. Von Arnim and R. Ahlrichs, Journal of Computational Chemistry **19**, 1746 (1998).

[77] G. Lippert, J. Hutter, and M. Parrinello, Theoretical Chemistry Accounts **103**, 124 (1999).

[78] M. Krack and M. Parrinello, Phys. Chem. Chem. Phys. **2**, 2105 (2000).

[79] K. N. Kudin and G. E. Scuseria, Phys. Rev. B **61**, 16440 (2000).

[80] L. Füsti-Molnár and P. Pulay, The Journal of Chemical Physics **117**, 7827 (2002).

[81] J. VandeVondele and J. Hutter, The Journal of Chemical Physics **118**, 4365 (2003).

[82] M. Del Ben, J. Hutter, and J. VandeVondele, Journal of Chemical Theory and Computation **8**, 4177 (2012).

[83] G. Kresse and J. Hafner, Journal of Physics: Condensed Matter **6**, 8245 (1994).

[84] R. M. Parrish, L. A. Burns, D. G. A. Smith, A. C. Simmonett, A. E. DePrince, E. G. Hohenstein, U. Bozkaya, A. Y. Sokolov, R. Di Remigio, R. M. Richard, J. F. Gonthier, A. M. James, H. R. McAlexander, A. Kumar, M. Saitow, X. Wang, B. P. Pritchard, P. Verma, H. F. Schaefer, K. Patkowski, R. A. King, E. F. Valeev, F. A. Evangelista, J. M. Turney, T. D. Crawford, and C. D. Sherrill, Journal of Chemical Theory and Computation **13**, 3185 (2017).

[85] S. F. Boys and F. Bernardi, Molecular Physics **19**, 553 (1970).

[86] P.-O. Löwdin, Phys. Rev. **97**, 1474 (1955).

[87] E. R. Davidson, Rev. Mod. Phys. **44**, 451 (1972).

[88] F. Aquilante, T. K. Todorova, L. Gagliardi, T. B. Pedersen, and B. O. Roos, The Journal of Chemical Physics **131**, 034113 (2009).

[89] M. Holzmann, R. C. Clay, M. A. Morales, N. M. Tubman, D. M. Ceperley, and C. Pierleoni, Phys. Rev. B **94**, 035126 (2016).

[90] K. Liao and A. Grüneis, J. Chem. Phys. **145**, 141102 (2016).

[91] J. McClain, Q. Sun, G. K.-L. Chan, and T. C. Berkelbach, J. Chem. Theory Comput. **13**, 1209 (2017), arXiv:1701.04832 .

[92] A. Grüneis, M. Marsman, J. Harl, L. Schimka, and G. Kresse, The Journal of Chemical Physics **131**, 154115 (2009).

[93] S. J. Nolan, M. J. Gillan, D. Alfè, N. L. Allan, and F. R. Manby, Phys. Rev. B **80**, 165109 (2009).

[94] J. Paier, C. V. Diaconu, G. E. Scuseria, M. Guidon, J. VandeVondele, and J. Hutter, Phys. Rev. B **80**, 174114 (2009).

[95] S. J. Binnie, S. J. Nolan, N. D. Drummond, D. Alfè, N. L. Allan, F. R. Manby, and M. J. Gillan, Phys. Rev. B **82**, 165431 (2010).

[96] S. J. Binnie, *Ab initio surface energetics: beyond chemical accuracy*, Ph.D. thesis, UCL (University College London) (2011).

[97] T. Tsatsoulis, F. Hummel, D. Usvyat, M. Schütz, G. H. Booth, S. S. Binnie, M. J. Gillan, D. Alfè, A. Michaelides, and A. Grüneis, The Journal of Chemical Physics **146**, 204108 (2017).

[98] S. Grimme, J. Antony, S. Ehrlich, and H. Krieg, The Journal of Chemical Physics **132**, 154104 (2010).

[99] A. Tkatchenko and M. Scheffler, Phys. Rev. Lett. **102**, 073005 (2009).

[100] M. Dion, H. Rydberg, E. Schröder, D. C. Langreth, and B. I. Lundqvist, Phys. Rev. Lett. **92**, 246401 (2004).

[101] G. Román-Pérez and J. M. Soler, Phys. Rev. Lett. **103**, 096102 (2009).

[102] J. Klimeš, D. R. Bowler, and A. Michaelides, Journal of Physics: Condensed Matter **22**, 022201 (2010).

[103] J. Klimeš, D. R. Bowler, and A. Michaelides, Phys. Rev. B **83**, 195131 (2011).

[104] A. Grüneis, M. Marsman, and G. Kresse, The Journal of Chemical Physics **133**, 074107 (2010).

[105] H.-J. Werner, T. B. Adler, and F. R. Manby, The Journal of Chemical Physics **126**, 164102 (2007).

[106] D. Usvyat, The Journal of Chemical Physics **139**, 194101 (2013).

[107] N. D. Drummond, R. J. Needs, A. Sorouri, and W. M. C. Foulkes, Phys. Rev. B **78**, 125106 (2008).

[108] A. Halkier, T. Helgaker, P. Jørgensen, W. Klopper, H. Koch, J. Olsen, and A. K. Wilson, Chemical Physics Letters **286**, 243 (1998).

[109] J. Moellmann and S. Grimme, The Journal of Physical Chemistry C **118**, 7615 (2014).

[110] E. Kanaki, G. Sansone, L. Maschio, and B. Paulus, Phys. Chem. Chem. Phys. **17**, 18722 (2015).

[111] J. Heyd, G. E. Scuseria, and M. Ernzerhof, The Journal of Chemical Physics **118**, 8207 (2003).

[112] A. V. Krukau, O. A. Vydrov, A. F. Izmaylov, and G. E. Scuseria, The Journal of Chemical Physics **125**, 224106 (2006).

[113] T. Bučko, S. Lebègue, J. Hafner, and J. G. Àngyàn, Journal of Chemical Theory and Computation **9**, 4293 (2013).

[114] T. Bučko, S. Lebègue, J. G. Àngyàn, and J. Hafner, The Journal of Chemical Physics **141**, 034114 (2014).

[115] K. S. Novoselov, A. K. Geim, S. V. Morozov, D. Jiang, Y. Zhang, S. V. Dubonos, I. V. Grigorieva, and A. A. Firsov, Science **306**, 666 (2004).

[116] K. S. Novoselov, A. K. Geim, S. V. Morozov, D. Jiang, M. I. Katsnelson, I. V. Grigorieva, S. V. Dubonos, and A. A. Firsov, Nature **438**, 197 (2005).

[117] A. Pakdel, C. Zhi, Y. Bando, T. Nakayama, and D. Golberg, ACS Nano **5**, 6507 (2011).

[118] W. Lei, D. Portehault, D. Liu, S. Qin, and Y. Chen, Nature Communications **4**, 1777 (2013).

[119] Y. S. Al-Hamdani, M. Ma, D. Alfè, O. A. von Lilienfeld, and A. Michaelides, The Journal of Chemical Physics **142**, 181101 (2015).

[120] Y. Wu, L. K. Wagner, and N. R. Aluru, The Journal of Chemical Physics **144**, 164118 (2016).

[121] F. Hummel, T. Tsatsoulis, and A. Grüneis, J. Chem. Phys. **146**, 124105 (2017).

[122] A. Grüneis, Phys. Rev. Lett. **115**, 066402 (2015).

[123] A. Ambrosetti, N. Ferri, R. A. DiStasio, and A. Tkatchenko, Science **351**, 1171 (2016).

[124] M. Kaltak, J. c. v. Klimeš, and G. Kresse, Phys. Rev. B **90**, 054115 (2014).

[125] M. Kaltak, J. Klimes, and G. Kresse, Journal of Chemical Theory and Computation **10**, 2498 (2014).

[126] J. Klimes, M. Kaltak, E. Maggio, and G. Kresse, The Journal of Chemical Physics **143**, 102816 (2015).

[127] V. Blum, R. Gehrke, F. Hanke, P. Havu, V. Havu, X. Ren, K. Reuter, and M. Scheffler, Computer Physics Communications **180**, 2175 (2009).

[128] A. Tkatchenko, A. Ambrosetti, and R. A. DiStasio, The Journal of Chemical Physics **138**, 074106 (2013).

[129] A. Ambrosetti, A. M. Reilly, R. A. DiStasio, and A. Tkatchenko, The Journal of Chemical Physics **140**, 18A508 (2014).

[130] A. Tkatchenko, R. A. DiStasio, R. Car, and M. Scheffler, Phys. Rev. Lett. **108**, 236402 (2012).

[131] J. Sun, A. Ruzsinszky, and J. P. Perdew, Phys. Rev. Lett. **115**, 036402 (2015).

[132] J. Sun, R. C. Remsing, Y. Zhang, Z. Sun, A. Ruzsinszky, H. Peng, Z. Yang, A. Paul, U. Waghmare, X. Wu, M. L. Klein, and J. P. Perdew, Nature Chemistry **8**, 831 (2016).

[133] L. Fumagalli, A. Esfandiar, R. Fabregas, S. Hu, P. Ares, A. Janardanan, Q. Yang, B. Radha, T. Taniguchi, and K. Watanabe, Science (Washington, DC, U. S.) **360**, 1339 (2018).

[134] J. Abraham, K. S. Vasu, C. D. Williams, K. Gopinadhan, Y. Su, C. T. Cherian, J. Dix, E. Prestat, S. J. Haigh, and I. V. Grigorieva, Nat. Nanotechnol. **12**, 546 (2017).

[135] R. K. Joshi, P. Carbone, F. C. Wang, V. G. Kravets, Y. Su, I. V. Grigorieva, H. A. Wu, A. K. Geim, and R. R. Nair, Science **343**, 752 (2014).

[136] D. Feller and K. D. Jordan, The Journal of Physical Chemistry A **104**, 9971 (2000).

[137] I. W. Sudiarta and D. J. W. Geldart, The Journal of Physical Chemistry A **110**, 10501 (2006).

[138] S. Xu, S. Irle, D. G. Musaev, and M. C. Lin, The Journal of Physical Chemistry A **109**, 9563 (2005).

[139] J. Ma, A. Michaelides, D. Alfè, L. Schimka, G. Kresse, and E. Wang, Phys. Rev. B **84**, 033402 (2011).

[140] J. G. Brandenburg, A. Zen, M. Fitzner, B. Ramberger, G. Kresse, T. Tsatsoulis, A. Grüneis, A. Michaelides, and D. Alf, The Journal of Physical Chemistry Letters **10**, 358 (2019).

[141] A. O. Ajala, V. Voora, N. Mardirossian, F. Furche, and F. Paesani, Journal of Chemical Theory and Computation **15**, 2359 (2019).

[142] E. Voloshina, D. Usvyat, M. Schütz, Y. Dedkov, and B. Paulus, Phys. Chem. Chem. Phys. **13**, 12041 (2011).

[143] H. Stoll, Phys. Rev. B **46**, 6700 (1992).

[144] H. Stoll, Chemical Physics Letters **191**, 548 (1992).

[145] H. Stoll, The Journal of Chemical Physics **97**, 8449 (1992).

[146] B. Paulus, Physics Reports **428**, 1 (2006).

[147] H. L. Williams and C. F. Chabalowski, The Journal of Physical Chemistry A **105**, 646 (2001).

[148] A. Heßelmann, Journal of Chemical Theory and Computation **9**, 273 (2013).

[149] U. Höfer, L. Li, and T. F. Heinz, Phys. Rev. B **45**, 9485 (1992).

[150] E. Pehlke and M. Scheffler, Phys. Rev. Lett. **74**, 952 (1995).

[151] M. R. Radeke and E. A. Carter, Phys. Rev. B **54**, 11803 (1996).

[152] A. Gross, M. Bockstedte, and M. Scheffler, Phys. Rev. Lett. **79**, 701 (1997).

[153] A. Biedermann, E. Knoesel, Z. Hu, and T. F. Heinz, Phys. Rev. Lett. **83**, 1810 (1999).

[154] E. Penev, P. Kratzer, and M. Scheffler, The Journal of Chemical Physics **110**, 3986 (1999).

[155] M. Dürr, M. B. Raschke, E. Pehlke, and U. Höfer, Phys. Rev. Lett. **86**, 123 (2001).

[156] M. B. Raschke and U. Höfer, Phys. Rev. B **63**, 201303 (2001).

[157] J. A. Steckel, T. Phung, K. D. Jordan, and P. Nachtigall, The Journal of Physical Chemistry B **105**, 4031 (2001).

[158] C. Filippi, S. B. Healy, P. Kratzer, E. Pehlke, and M. Scheffler, Phys. Rev. Lett. **89**, 166102 (2002).

[159] M. Dürr and U. Höfer, Surface Science Reports **61**, 465 (2006).

[160] W. Brenig and E. Pehlke, Progress in Surface Science **83**, 263 (2008).

[161] R. A. Wolkow, Phys. Rev. Lett. **68**, 2636 (1992).

[162] A. Ramstad, G. Brocks, and P. J. Kelly, Phys. Rev. B **51**, 14504 (1995).

[163] S. B. Healy, C. Filippi, P. Kratzer, E. Penev, and M. Scheffler, Phys. Rev. Lett. **87**, 016105 (2001).

[164] G. Kresse and J. Furthmüller, Computational Materials Science **6**, 15 (1996).

[165] G. Kresse and J. Furthmüller, Phys. Rev. B **54**, 11169 (1996).

[166] G. Henkelman and H. Jónsson, The Journal of Chemical Physics **113**, 9978 (2000).

[167] G. Henkelman, B. P. Uberuaga, and H. Jnsson, The Journal of Chemical Physics **113**, 9901 (2000).

[168] K. L. Schuchardt, B. T. Didier, T. Elsethagen, L. Sun, V. Gurumoorthi, J. Chase, J. Li, and T. L. Windus, Journal of Chemical Information and Modeling **47**, 1045 (2007).

[169] T. Gruber, K. Liao, T. Tsatsoulis, F. Hummel, and A. Grüneis, Phys. Rev. X **8**, 021043 (2018).

[170] C. Adamo and V. Barone, The Journal of Chemical Physics **110**, 6158 (1999).

[171] J. Harl, L. Schimka, and G. Kresse, Phys. Rev. B **81**, 115126 (2010).

[172] X. Ren, P. Rinke, C. Joas, and M. Scheffler, Journal of Materials Science **47**, 7447 (2012).

[173] F. Furche, Phys. Rev. B **64**, 195120 (2001).

[174] T. Helgaker, T. A. Ruden, P. Jrgensen, J. Olsen, and W. Klopper, Journal of Physical Organic Chemistry **17**, 913 (2004).

[175] D. Porezag and M. R. Pederson, The Journal of Chemical Physics **102**, 9345 (1995).

[176] A. Mahler, B. G. Janesko, S. Moncho, and E. N. Brothers, The Journal of Chemical Physics **146**, 234103 (2017).

[177] M.-C. Kim, E. Sim, and K. Burke, Phys. Rev. Lett. **111**, 073003 (2013).

[178] B. G. Janesko and G. E. Scuseria, The Journal of Chemical Physics **128**, 244112 (2008).

[179] A. Patra, H. Peng, J. Sun, and J. P. Perdew, Phys. Rev. B **100**, 035442 (2019).

Publications

- George H Booth, Theodoros Tsatsoulis, Garnet Kin-Lic Chan, and Andreas Grüneis

  "From plane waves to local Gaussians for the simulation of correlated periodic systems"

  The Journal of chemical physics, **145**, 084111 (2016).

- Y. S. Al-Hamdani, M. Rossi, D. Alf, T. Tsatsoulis, B. Ramberger, J. G. Brandenburg, A. Zen, G. Kresse, A. Grneis, A. Tkatchenko, and A. Michaelides,

  "Properties of the water to boron nitride interaction: From zero to two dimensions with benchmark accuracy"

  J. Chem. Phys. **147**, 044710 (2017).

- T. Tsatsoulis, F. Hummel, D. Usvyat, M. Schütz, G. H. Booth, S. S. Binnie, M. J. Gillan, D. Alfe, A. Michaelides, and A. Grüneis,

  "A comparison between quantum chemistry and quantum Monte Carlo techniques for the adsorption of water on the (001) LiH surface"

  The Journal of Chemical Physics **146**, 204108 (2017).

- Felix Hummel, Theodoros Tsatsoulis, and Andreas Grüneis,

  "Low rank factorization of the Coulomb integrals for periodic coupled cluster theory"

  The Journal of Chemical Physics **146**, 124105 (2017).

- J. G. Brandenburg, A. Zen, M. Fitzner, B. Ramberger, G. Kresse, T. Tsatsoulis, A. Grüneis, A. Michaelides, and D. Alfe,

  "Physisorption of water on graphene: Subchemical accuracy from many-body electronic structure methods"

  The Journal of Physical Chemistry Letters **10**, 358 (2019).

- T. Gruber, K. Liao, T. Tsatsoulis, F. Hummel, and A. Grüneis,

"Applying the coupled-cluster ansatz to solids and surfaces in the thermodynamic limit"

Phys. Rev. X **8**, 021043 (2018).

- Theodoros Tsatsoulis, Sung Sakong, Axel Groß, and Andreas Grüneis,

  "Reaction energetics of hydrogen on Si (100) surface: A periodic many-electron theory study"

  The Journal of chemical physics, **149** 244105 (2018).

Talks, Posters, Schools and Awards

Talks

1. DPG meeting *6–11 March 2016 Regensburg, Germany*
2. APS meeting 2017 *13–17 March New Orleans, USA*
3. Invited Talk - Axel Gross Group *14 December 2017 University of Ulm, Germany*

Posters

1. DPG meeting

   6–11 March 2016 Regensburg, Germany

2. Future of Chemical Physics, JCP

   31 August–2 September 2016 Oxford, U.K.

3. APS March meeting 2017

   13–17 March New Orleans, USA

4. 17th European Seminar on Computational Methods in Quantum Chemistry

   11–14 July 2017 Harper-Adams University, Shropshire, U.K.

5. WATOC 2017

   27 August–1 September 2017 Munich, Germany

6. CECAM Workshop

8–10 November 2017 Laussane, Switzerland

7. 16-ICQC

18–23 June 2018 Menton, France

8. CECAM 50 Years conference

9–12 September 2019 Laussane, Switzerland

Schools

1. MWM Summer School 2016: Modern Wavefunction Methods in Electronic Structure Theory

3–8 Oct 2016 Gelsenkirchen, Germany

Awards and Scholarships

1. International Max Planck Research School Scholarship 2013-2015
2. Poster prize: 17th European Seminar on Computational Methods in Quantum Chemistry *11–14 July 2017 Harper-Adams University, Shropshire, U.K.*
3. Poster prize: 16-ICQC *18–23 June 2018 Menton, France*